APPLICATIONS OF SHORT AND ULTRASHORT LASER INTERACTION WITH MATTER: FOR ABLATION AND NANOLITHOGRAPHY

by

Ahmed M. Elsied

A Dissertation

Submitted to the Faculty of Purdue University

In Partial Fulfillment of the Requirements for the degree of

Doctor of Philosophy

School of Nuclear Engineering

West Lafayette, Indiana

December 2020

THE PURDUE UNIVERSITY GRADUATE SCHOOL

STATEMENT OF COMMITTEE APPROVAL

Dr. Shripad T. Revankar, Chair

School of Nuclear Engineering

Dr. Lefteri H. Tsoukalas

School of Nuclear Engineering

Dr. Mamoru Ishii

School of Nuclear Engineering

Dr. David Koltick

Department of Physics and Astronomy

Approved by:

Dr. Seungjin Kim

To my father Mohamed Abu Elela and the soul of my mother Soheir Abu Elela, there are no words in my dictionary that can express what you deserve. All of what I have achieved and what I am going to achieve are all gifted to you. Thank you for your love, care, and inspiration. This work and any success I ever accomplished were never going to be achieved without the grace and mercy of the almighty God. All the praise to him alone.

ACKNOWLEDGMENTS

First of all, I offer my sincere appreciation to Prof. Ahmed Hasanein for research support, guidance, laboratory access and funding support. Also, I like to express my deepest gratefulness to Prof. Shripad T. Revankar for helping me in my thesis and improving my research. My sincere thanks to my thesis committee Prof. Mamoru Ishii, Prof. Lefteri H. Tsoukalas, and Prof. David S. Koltick for their support and their priceless advises. This work would have not been done without the help from my team: Dr. Prasoon K. Diwakar, Nicholar C. Termini, Payson C. Dieffenbach. Finally, I would like to acknowledge that this work was supported by the National Science Foundation PIRE project.

TABLE OF CONTENTS

LIST OF FIGURES

ABSTRACT

The laser is being applied to various industrial applications as well as many research areas since the first laser built in the 1960s until it became a promising candidate for the technology development in the modern life. Hence, laser-material interaction continued to draw global attention. Understanding the mechanism of laser-material interaction at the femto- and nanosecond scales is crucial for basic research as well as energy, industrial, and defense applications. This thesis provides a study of the physics involved in laser-target interaction processes. This study starts with laser energy couples to target materials, then followed by studying of the ejected target particles, and the evolution of the evolving plasma. Although there are thorough works both theoretical and experimental which have been conducted over the years, there are still open questions to be answered. This includes the coupling of laser energy to the target material mainly in the high laser energy regions, the role of laser pulse duration on the dependence of the energy-target coupling, the charged particles ejection mechanisms, and how the pulse duration and target material properties affect target evolution.

Understanding of the physics and mechanisms of laser energy coupling to the target material was then used for developing and optimizing multi-disciplinary applications. In this thesis, the ultrafast laser was investigated as a promising candidate for nanoparticles generation and thin film fabrication. Furthermore, laser energy was used to study the erosion of metals under different ambient conditions of gas and pressure, these conditions provide a simultaneous thermal, charged particles, and photons irradiation. These conditions are similar to the conditions at which material is exposed to in real applications such as energy applications using fusion reactors. Coupling both ultrafast and fast laser pulses was used for extreme ultraviolet (EUV) light generation for advanced nanolithography for the next-generation computer chips. This laser-produced plasma could provide a solution to one of a problem existing in the current lithography industry which is ion debris and EUV photon collection system lifetime degradation.

NOMENCLATURE

E:	Electric filed intensity
B:	Magnetic field intensity
ε_o:	Vacuum permittivity
ε_f:	Fermi temperature
μ_0:	Vacuum permeability
e:	Electron charge
v:	Velocity
n_0:	Ion number density
n_e:	Electron number density
n_{cr}:	Critical plasma density
ω:	Laser angular frequency
$\omega_{1/2}$:	Half-width at half maximum of measured at 10^{16} cm^{-3}
$\omega_{pe:}$	Plasma frequency
v_{ei}:	Electron-ion collision frequency
T_e:	Electron temperature
T_h:	Electron temperature of hot species
T_i:	Ion temperature
T_D:	Debye temperature
T_m:	Melting temperature
θ:	laser incidence angle measured from normal to the target surface
Φ:	Phase factor
k:	Wave number
k_e:	Electron thermal conductivity
l_s:	Optical skin depth
c:	Speed of light
C_e:	Electron heat capacity
C_i:	Ion heat capacity

C_s:	Ablated plume speed
γ:	electron-ion coupling factor
η:	Photon absorption coefficient
I_0:	Amplitude of laser intensity
τ_e:	Electron cooling time
τ_i:	Ion cooling time
τ_L:	Laser pulse duration
λ:	Laser wavelength
S:	Laser spot size on the target surface
r:	Distance from the target surface to the detector
Q:	Charge of ions
β:	Forward peaking factor the ratio between the longitudinal and transverse axis of the plume
ρ:	Target mass density
ρ_P:	Plume mass density
ρ_{amb}:	ambient gas mass density
P_s:	Pressure on the target surface
$P_{plume,bottom}$:	Pressure of the bottom of the plume
M:	Ion's mass.
A:	Atomic weight
Z^*:	Charge of ejected ion
Z_{avg}:	Average ion's charge state
k_B:	Boltzmann constant
E_{max}:	Theoretical maximum kinetic energy

ABBREVIATIONS

WLP:	White Light Profilometer
AFM:	Atomic Force Microscope
EUV:	Extreme Ultraviolet Emission
DPP:	Discharge Produced Plasma
LPP:	Laser Produced Plasma
FC:	Faraday Cup
IC:	Ion Collector
CE:	Conversion Efficiency

CHAPTER 1. INTRODUCTION

1.1 Problem statement and significance of the problem

Despite much theoretical and experimental research reported in the field of laser-material interaction existing in literature, the laser energy coupling to the target material is still far from being fully understood. Laser-material interaction is a complicated problem to deal with because it depends on multiple parameters, including laser properties, namely energy, pulse duration, wavelength, spot size, and angle of incidence; and thermal and physical material properties, such as mass, mass density, thermal conductivity, melting temperature, the heat of vaporization, and ambient irradiation conditions such as background gas and pressure. In most cases it is not possible to study the effect of one single parameter in the absence of others. Making the understanding of laser-material interaction even more complex. The absence of experimental and theoretical models of laser-material interaction, especially at elevated laser power, such as the terawatt regime, the physics of this regime remains largely unexplored. Exploring the physics and building models for laser energy coupling in such a regime help overcome one of the problems associated with laser ablation such as Heat Affected Zone (HAZ), which causes permanent thermal damage to the target material. Laser-induced ions are main consequence of laser-material interaction; however, the ion ejection mechanism, namely ions with high energy, remains a debatable topic in the literature were multiple theories interpreted it differently. A comprehensive understanding of the dynamics of laser-induced ions, such as flux and energy spatial evolution and temporal evolution, is of high interest for some applications in the semiconductor industry, which suffers from lifetime degradation to its production systems due to erosion by laser-induced ions and low efficiency due to limited laser energy coupling to the target material.

1.2 Literature review

The concept on which laser technology depends was first proposed by Albert Einstein in 1916 when he first proposed that photon can stimulate the emission of an identical photon from an excited atom. This concept inspired a lot of physicists to explore the physics of photon stimulation [1]. Since then, development in laser science has continued unabated until the present. In the 1960s, laser science became an applicable science when the American engineer and physicist

Theodore H. Maiman built the first laser generator source [2]. Ever since, new applications numerous research areas began to rely on laser technology finally laser technology itself became the main focus of development. A wide spectrum of applications that have advanced from laser science in multiple areas such as medical, industrial, and energy and forensic science. A few of these applications include Laser-Induced Breakdown Spectroscopy (LIBS) [3], nanoparticle generation [4], tabletop shorter wavelength light source for next generation nanolithography [5], pulsed laser deposition (PLD) [6], and ion implantation [7]. Developing these applications promoted the importance of understanding the physics of laser energy coupling to materials (Laser-Material Interaction).

In principle, laser-material interaction is a photothermal process through which laser energy interacts with the target material by either absorption and/or reflection of the incident photons. The material is affected by the amount of photon energy that can be absorbed within its volume. When dealing with solid targets, particularly metals and dielectrics, there are multiple absorption mechanisms, such as interband absorption due to free charge carriers, interband transitions and molecular excitation, absorption by collective excitations (excitons, photons), and absorption by impurities and defects [8]. Consequently, this absorbed energy heats the target to elevated temperatures. This is followed by material removal from the target due to vaporization, melt, phase explosion, and/or normal boiling [9]. The removed/ablated mass forms a plasma plume that propagates in the medium in front of the target. This plume forms at an early time during the laser pulse and contains different kind of particles: charged particles consist of free electrons and ions and neutral particles consist of neutral atoms, and clusters of particles which varies in size and shape, such as fragments. Laser energy gets absorbed within a limited volume of the target material limited by the target material's optical properties, incident laser properties, and plasma properties that form within the target [10]. However, the creation of free charged particles and thermal waves is a result of laser-material interaction which carry the incident laser energy further through the target and lead to further material ablation. As a result of laser ablation, a crater profile forms within the target volume; this crater profile represents the amount of mass removed from the target [11]. The properties of the ablated plume and the crater profile are dependent on the laser parameters, such as laser energy, pulse duration, spot size, and laser wavelength [12,13]; ambient conditions, such as background gas and pressure; and the material properties, such as thermal and physical properties [14,15].

In literature, there are significant efforts were exerted to help investigating experimentally the effect of incident laser on the ablation process [16–19] in power regime varies from mega to giga watt. Along with experimental work, theories and models in literature were developed to help to understand the physics of laser ablation. One-dimensional hydrodynamic simulations and two-temperature models of metal ablation by ultrashort laser [20] attributed laser ablation at moderate laser fluence less than few J/cm^2 to the shock wave creation induced by laser energy deposition that drives the target surface to expand at a high speed and nonuniform strain rate. Simultaneously, rapid heating to the material causes the material to melt, forming a liquid phase. This liquid phase gets fragmented by the nonuniform high strain rate, turning it into an ensemble of droplets so the ablation occurs; this process is called homogeneous nucleation [20]. However, insight into the formation and ejection mechanism of these droplets was not viable due to the lack of knowledge about the microscopic properties of the interfacial solid-liquid phase. Consequently, the gap between experimental and theoretical results is pronounced. Laser-material interaction in an elevated laser power such as the terawatt regime is of interest for laser particle acceleration [21]; to the best of our knowledge, this regime has not been explored experimentally, and no data in the literature is provided about this regime, so this lack of information makes this field interesting from both the fundamental physics and application understanding. Permanent thermal damage to the target material has been a research topic for the laser machining industry [22] that downgraded the laser's capability to compete with conventional etching mechanisms such as wet etch and dry etch [23]. Permanent thermal damage presented in the HAZ was associated with the laser with long pulse duration (> few picoseconds) compared to a typical time of electron-phonon collisions in the solid matter, which is in the order of few picoseconds, and it was absent in the case of lasers with shorter pulse duration, such as the femtosecond laser [17]. However, ultrashort laser ablation mechanism was still lacking a sufficient understanding especially the mechanism behind widening the crater/ablation profile. Furthermore, the effect of ambient conditions on the HAZ and the possibilities to mitigate such impact was also an inquiry. The theoretical and experimental aspects of laser-induced plasma were investigated in the literature to understand the plasma plume dynamics: formation, time and space evolution, and relative population of its constituents [24–26]. However, ion ejection mechanism during laser-material interaction has been a debatable research topic mainly due to the multiple theories in the literature about the driving force that is responsible for ejecting ions from the target material, specifically ions with higher energies. In literature, ions

with higher energies were attributed to the laser-plasma interaction followed by laser ablation [27], other theories attributed it to the space charge mechanism [28]. Furthermore, some other theories attributed it to the hydrocarbon contamination exists on the target surface [29,30]. The existence of variant theories trying to explain the ejection mechanism of higher ion energy acquires extra research to be done to answer that question. As semiconductor technology continues to develop, microchips are getting denser, as stated by Moore's law [31]. To manufacture these denser microchips, the features on these chips need to be smaller and have a higher aspect ratio. The latest technology relies on Laser- Produced Plasma (LPP) to generate a photon source to manufacture such features on semiconducting material; the smaller the features required to be manufactured, the shorter the wavelength of the light source has to be. Laser-produced tin plasma was found to be a promising candidate to meet semiconductor industry needs by generating light source with a short wavelength in the region of Extreme Ultraviolet light (EUVL), 13.5 nm. However, three main problems were found by using laser-produced tin plasma that are currently facing the semiconductor industry, namely conversion efficiency (CE): the efficiency at which EUVL can be generated from a laser source, the frequency at which the EUVL can be generated, lastly the ion debris mitigation problem [32]. Consequently, research has been going on to close these gaps. It was found that EUVL CE is highly dependent on the laser spot size as well as laser wavelength. Laser spot size affects the plasma plume expansion and consequently the absorption of the laser within the plume; a shorter wavelength enables higher absorption of laser energy within the target as well as within the laser plume [33]. Spatial uniformity and absolute yield of EUV light were found to be a function of laser pulse duration as it was reported that a 30% enhancement in EUV emission and uniformity when using picosecond pulse laser over femtosecond pulse laser [34,35]. A small incident laser angle was found to increase the EUVL emission due to changing the opacity of the plasma, so the EUVL absorption within the plume decreased [36]. Despite a large number of theoretical and experimental investigations on the role of laser parameters on EUV CE, the influence of laser pulse duration on EUV CE, spectral features, and ion debris are far from being fully understood.

1.3 Hypothesis

There have been a lot of studies on laser ablation that state the effect of laser fluence on the ablation profile [16–18,37]. They theorized that laser ablation depth follows Beer's low that states that

ablation depth is a logarithmic function of laser fluence. So, by using elevated laser fluence, features with deeper depth can be formed. Consequently, HAR feature can be achieved which are essential for semiconductor as well as micromachining industry.

Studies [37,38] state that fast ions are formed as a result of further plume heating by the incident laser, other studies attribute it to the existence of hydrocarbon contaminants on the target surface. Theoretical studies state that the energy relaxation time between laser-induced electrons and lattice atom is in the order of few picoseconds. Accordingly, irradiating the target material with laser pulse that has duration less than picoseconds eliminates the possibility of heating the plume by the incident laser. Furthermore, applying cleaning laser shots to the target material rule ensures that contaminants were cleaned off before acquiring the ion's signal.

When pulse duration is longer than the electron-ion energy relaxation time [39], laser-plume interaction will occur consequently the dynamics of the plume will have a significant effect on laser ablation. So, ambient conditions were exploited to investigate the role of plume dynamics on laser ablation.

Studies [40–42] show that molten material fragmentation by internal shockwave is the driving mechanism for nanoparticles formation in case of ultrashort laser material interaction. This can alter the size of the ejected nanoparticles at elevated laser fluence.

If a dense cloud of particles can be generated prior to the generation of EUV photons, it will attenuate the ion debris accompanying EUV photons. Consequently, it can provide a solution to the lifetime degradation occurs in EUVL optical system used to collect EUV photons.

1.4 Thesis Objectives

The overall objective of this work is to provide a better understanding of laser-material interaction in regimes that are not investigated in the literature, and to provide solutions to some of the gaps in industry namely, ion debris in nanolithography and HAR features in semiconductor fabrication, this can be summarized in four objectives as follow:

1. Study laser ablation at terawatt regime, different ambient conditions and different material properties.

2. Study the dynamics of laser-produced ions and electrons.
3. Study the properties of laser-produced nanoparticles.
4. Proposing an irradiation scheme for EUVL generation that can mitigate the ion debris.

To accomplish these objectives, series of experiments were designed and conducted to provide parametric study on the effect of some of the parameters that influence the laser-material interaction as follow:

1. The effect of laser fluence on the ablation profile at elevated laser fluence.
2. The effect of material properties on the ablation profile and the thermal damage.
3. The effect of ambient gas type and pressure on ablation profile and the thermal damage.
4. The effect of laser fluence on laser-produced ion's dynamics and nanoparticles.

Modeling and theories were provided to explain some of the phenomena that are associated with laser-material interaction that were observed through this work. The unique points of this research are presented in the study of laser-material interaction in the terawatt regime at which Beer's law breaks, investigating the laser-induced ions ejection mechanisms during laser-material interaction. Investigating the thermal damage and the Heat Affected Zone (HAZ) caused by laser irradiation showing the effect of ambient conditions on the permanent damage that can be caused to the material as a result of laser-material interaction, explaining the ablation profile widening resulting from the laser ablation process, explaining the dependence of nanoparticle size and shape on the laser properties. Eventually, propose a new EUV generation scheme for nanolithography application that can mitigate the ion debris deposition of on the EUV photon collection system which results in a decrease in the reflectivity and impact the lifetime of such a system.

1.5 Methodology

Two different laser systems were exploited in this work to investigate the characteristics of laser-material interaction, namely Ti:Sapphire, which laser that generates 800 nm laser wavelength, 40 fs FWHM pulse duration, P-polarized, laser energy up to 110 mJ, 1×10^{-8} picosecond contrast ratio, and 1×10^{-7} nanosecond contrast ratio; and Nd:YAG laser, which generates 1064 nm laser wavelength, 6 ns FWHM pulse duration, P-polarized and laser energy up to 300 mJ. Different targets used throughout this work vary in their properties, but all are solid targets. The interaction

was conducted in an ablation chamber in which the background pressure and gas can be controlled through a feedthrough connected to the chamber. Different background pressures were used in this work: 10-6 Torr, 10 Torr, and 760 Torr; similarly, two different background gases were used in this work: Ar and air. Ion Time-of-Flight (TOF) measurement method used for ion flux and ion velocity measurement using Faraday Cup ion collector (IC). IC was also mounted on an angle manipulator to investigate the ion flux and ion kinetic energy angular distribution. Time-gated LIBS technique was used for measuring the plasma properties such as electron plasma density and temperature based on the spectral line emission's profile and Boltzmann plot method, respectively. A time-gated fast imaging technique was used to measure the plasma plume expansion and propagation rate using an ICCD camera. The laser ablation profile was measured based on light interference using White Light Profilometer (WLP). Nanoparticle properties were first deposited on a Si plate and then measured using Atomic Force Microscopy (AFM) technique.

1.6 Laser-Material Interaction: Theoretical and Analytical background

In this work, the laser energy is exploited to study the physics of laser-material interaction and their application. To understand how the electromagnetic (EM) wave interacts with a solid target, it is better to start from a simple analytical background that explains how the laser energy couples with the target material. Equation 1.1 show Maxwell equations [43] that provide a general description of how this process occurs:

$$\nabla \cdot \vec{E} = \frac{1}{\varepsilon_o} e(n_o - n_e) \quad (1.1.\ a)$$

$$\nabla \times \vec{E} = -\frac{\partial \vec{B}}{\partial t} \quad (1.1.b)$$

$$\nabla \times \vec{B} = -\mu_o e n_o \vec{v} + \varepsilon_o \mu_o \frac{\partial \vec{E}}{\partial t} \quad (1.1.c)$$

$$\nabla \cdot \vec{B} = 0 \quad (1.1.d)$$

Where $\boldsymbol{E}$ and $\boldsymbol{B}$ are the electric and magnetic field intensities, n_o, n_e are the ion and electron number densities, e, $\boldsymbol{v}$ are the electron charge and velocity, ε_o and μ_o are the vacuum permittivity and

permeability. Solving for ***E*** by taking the curl of Eq. (1.1.b) and substituting from Eq. (1.1.c) results in the wave equation, Eq. (1.2):

$$\nabla^2\vec{E} - \varepsilon_o\mu_o\frac{\partial^2\vec{E}}{\partial t^2} = -\mu_o e\frac{\partial(n_o\vec{v})}{\partial t} + \nabla(\nabla\cdot\vec{E}) \tag{1.2}$$

The right-hand side of the wave equation represents the laser source term of the EM field. Linearizing Eq. 1.2 by assuming that all fields and fluid quantities have a harmonic time dependence *exp(-iωt)*, where ω is laser frequency, and using Lorentz force equation (Eq. 1.4) to solve for *v*:

$$\frac{\partial}{\partial t} \rightarrow -i\omega \tag{1.3.a}$$

$$n_e \rightarrow n_o + n_1 \tag{1.3.b}$$

$$\vec{E} + \vec{v}\times\vec{B} \rightarrow \vec{E}_1 \tag{1.3.c}$$

$$m\frac{d\vec{v}}{dt} = -e(\vec{E} + \vec{v}\times\vec{B}) - mv_{ei}\vec{v} \tag{1.4}$$

$$\nabla^2\vec{E}_1 + \frac{\omega^2}{c^2}\left(1 - \frac{\omega_{pe}^2}{\omega(\omega - iv_{ei})}\right)\vec{E}_1 = \nabla(\nabla\cdot\vec{E}_1) \tag{1.5}$$

$$\varepsilon = 1 - \frac{\omega_{pe}^2}{\omega(\omega - iv_{ei})} \tag{1.6}$$

Equation 1.6 is the relative permittivity that describes how the material properties change as a result of laser irradiation through its dependence on plasma frequency, ω_{pe}, and electron-ion collision frequency, v_{ei}. These two parameters (ω_{pe} and v_{ei}) are functions of plasma temperature which is a function of the incident laser energy as will be discussed later. In the limit of cold plasma, the electron temperature is less than Fermi temperature ($T_e < \varepsilon_f$) the collision frequency is governed by the scattering of electrons by phonons or lattice vibration, Equation (1.7.a). In contrast, hot plasma is dependent on electron-ion collisions, as shown in Equation (1.7.b).

$$v_{el-phonon} \simeq 2k_s\frac{e^2k_BT_i}{\hbar v_f} \qquad \text{at } T_D < T_e < T_m, v_f << c, \text{ and } \hbar\omega_{pi} << k_BT_i \tag{1.7.a}$$

$$v_{ei} = 3 \times 10^{-6}\, ln(\Lambda) \frac{n_e Z}{T_e^{1.5}(eV)} \text{at } T_e > \varepsilon_f \quad (1.7.b)$$

Where ln(Λ) is Coulomb logarithm, v_f is Fermi velocity, k_B, ħ, are Boltzmann and Plank's constant. Z is the atomic number, and T_D, T_m, T_i represent the Debye, melting, and ion temperatures, respectively. There is no exact expression for the collision frequency in the range between fermi temperature and melting temperature. The collision frequency determines how fast can the energy transfer either from laser to electrons, electrons to electrons, or electrons to lattice. The maximum value for the electron-ion collision was found to be in the order of the electron plasma frequency, $v_{ei} \sim \omega_{pe}$ [44].

To determine the amount of the laser energy that can be absorbed by the target and the target volume that will be affected by the laser energy, considering the case of incident plane wave at angle θ and solving Equation. 1.5. for ***E.*** The Solution is given by Equations. 1.8 and 1.9 in a vacuum and inside the target, respectively:

$$\vec{E}_1(x) = 2\vec{E}_o\, sin(\, kx\, cos(\, \theta) + \phi) \quad \text{at x<0 (vacuum)} \quad (1.8)$$

$$\vec{E}_1(x) = \vec{E}(0) e^{-(\frac{x}{l_s})} \quad \text{at x>0 (inside target)} \quad (1.9)$$

where φ is a phase factor will be determined later and k is the wavenumber. Accordingly, the electric field decays exponentially inside the target material [45] (Eq. 1.9) leading to deposition of laser energy in a certain depth of the material known as optical skin depth or penetration depth, l_s, (Eq. 1.10), that is expressed as:

$$l_s = \frac{c}{\omega\, Im[\sqrt{\varepsilon}]} \quad (1.10)$$

Along with the laser spot size, the optical skin depth determines the volume of the material that absorbs the incident laser energy, hence the particle flux that can be generated from the target. Eq. 1.10 shows the dependence of l_s on laser properties through ω and material properties through the imaginary part of the dielectric constant $Im[\sqrt{\varepsilon}]$. For high-conducting metals this can be approximated as $\left(l_s \approx (\frac{c}{\omega_{pe)}} \sqrt{2\nu_{eff}/\omega}\right)$ [10]. Using the boundary conditions at x=0 leads to an expression of the incident electric field inside the material (Equations. 1.11 & 1.12).

$$\vec{E}_1(x) = 2\vec{E}_o \, sin(\phi) e^{-(\frac{x}{l_s})} \quad (1.11)$$

$$tan(\phi) = -\frac{\omega}{c} l_s \, cos(\theta) \quad (1.12)$$

Besides the EM theory, several analytical models were used to determine the amount of incident laser energy that can be deposited in the target material. The two-temperature model was found to be relatively simple and quite efficient in describing the energy transfer from the laser to the target's electrons hence from electrons to lattice [46,47]:

$$C_e(T_e) n_e \frac{\partial T_e}{\partial t} = -\frac{\partial \chi(x)}{\partial x} - \gamma(T_e - T_i) - \frac{\partial S}{\partial x} \quad (1.13.a)$$

$$C_i(T_e) n_e \frac{\partial T_i}{\partial t} = \gamma(T_e - T_i) \quad (1.13.b)$$

$$\chi(x) = -k_e \frac{\partial T_e}{\partial x} \quad (1.13.c)$$

$$\frac{\partial S}{\partial x} = -\frac{2\eta}{l_s} I_o e^{-(\frac{2x}{l_s})} \quad (1.13.d)$$

$$I_o = \frac{\varepsilon_o c}{2} (2E_o \, sin(\phi))^2 \quad (1.13.e)$$

where C_e and C_i are electrons and ions heat capacity, k_e and γ are the electron's thermal conductivity and electron-ion coupling parameter, η and I_o are the absorption coefficient and amplitude of laser intensity, relatively. At temperatures >1eV the electron heat capacity is considered to be constant ~1.5 [48]. It can be concluded from Eq. 1.13 that, the laser-matter interaction is controlled by three different time scales: electron cooling time ($\tau_e = \frac{C_e}{\gamma}$), ion heating time ($\tau_i = \frac{C_i}{\gamma} \sim ps$), and laser pulse duration (τ_L). In the case of the ultrashort laser pulse $\tau_L << \tau_e$, lattice electrons coupling as well as thermal conductivity can be neglected [49]. Consequently, Equation 1.13.a can be easily solved for T_e resulting in an analytical expression to the dependence of electron temperature on the incident laser intensity, Equation 1.1:

$$T_e(t) = \frac{4}{3} \frac{\eta I_o t}{l_s n_e} e^{-(\frac{2x}{l_s})} \quad (1.1)$$

For most of the metals, the ratio between the absorption coefficient and the optical skin depth is almost constant and can be expressed as $\frac{\eta}{l_s} \approx (2\omega/c)\left(1 - \sqrt{\frac{\omega}{2\omega_{pe}}}\right)$ [10]. Thus, it can be inferred from Equation 1.14 that elements with higher electron number density have lower electron temperature compared to elements with low electron number density. The electron's energy transferred to ions as shown by Equation 1.13.b will result in ion ejection and plasma plume formation. Furthermore, the incident laser energy is carried deeper inside the target either by a thermal wave, as in the case of longer laser pulse duration, or by the free electrons and ions, as in the case of the ultrashort laser pulse. These energy carriers transfer their energies to the target material resulting in the melting of the target followed by target vaporization. These two phases: liquid (melted target's material) and gas (vaporized target's material) determine the amount of material that can be ejected/ablated from the target; this is called laser ablation. Eventually, this leads to a plume formation which consists of charged particles, neutral atoms, nanoparticles, and clusters. Diagnostic techniques such as fast imaging were used to analyze the ejected plume showed that charged components of the plume propagate ahead of the neutral components [50–52] with velocities one order of magnitude higher than the neutral particles.

In this thesis, a study of laser-material interaction is provided with study of the laser-energy coupling to the target's material and the consequent ablation occurs within the target material volume as well as the effect of laser ablation profile characteristics on the incident laser fluence. Material removed from the target material (ablated material) consists of different species of particles charged, neutral, and fragments. The properties of ultrashort laser-produced ions specifically, the effect of laser flux and velocity on incident laser fluence and irradiated material, the effect of target material on both temporal and angular distribution of these ions furthermore, ion ejection mechanisms existing during laser-material interaction were studied in chapter 3. Chapter 4 studies the characteristics of laser-produced ions using short laser pulse instead to highlight the effect of plasma shielding in laser ablation, thermal impact in irradiated material as a consequence of laser irradiation as well as the effect of material properties on laser ablation. Along with the ions, there are electrons that are ejected in the ablated plume, the evolution of these electrons in space and time in terms of their density and temperature were studied in chapter 5. The effect of ambient conditions specifically the effect of the type of ambient gas and the ambient pressure on laser ablation is studied in chapter 6. Chapter 7 focuses on the properties of the neutral

particles ejected along with the charged particles as a result of laser ablation to provide a comprehensive picture of laser-material interaction starting with laser energy coupling to the target material and ending with properties of the ablated material. Chapter 8 sheds light on the application of laser-material interaction in the nanolithography industry, as it proposes a new irradiation system for EUVL generation, the objective of this system is to mitigate the ion debris that has a significant lifetime impact on the EUVL collection system.

In this work ultrafast, ultrashort, and femtosecond laser are used interchangeably; similarly, fast and nanosecond laser are used interchangeably as well.

CHAPTER 2. LASER ABLATION OF MATERIALS

Chemical etching is being a traditional way for material processing and machining. As various applications develop, they tend to reduce the size of their components, such as microchip fabrication for semiconductors. This in turn challenges the potentials and the efficiency of chemical etching as a common method for material processing. Furthermore, chemical etching has environmental and health concerns. The recent development in laser technology has enabled scientists to use the laser-ablation mechanism, as a competitive candidate for material processing, to replace chemicals. Consequently, the nanosecond laser was exploited for laser micromachining. Unfortunately, the pulse duration of such laser is long enough to cause a large heat-affected zone (HAZ) and significant thermal damage to the material being processed. Consequently, this causes a serious challenge when using nanosecond laser for micromachining. This chapter discusses the basics of laser ablation with comprehensive experiments showing that the thermal effect/damage induced by long pulse duration such as nanosecond laser can be significantly reduced when using an ultrashort laser pulse as an alternative laser for micromachining [53,54].

2.1 Ultrashort Laser Ablation

2.1.1 Experimental Setup

The experimental system comprises a chirped pulse amplifier (CPA) laser system that consists of Synergy^{TM} Mirror-dispersion-controlled Ti:Sapphire oscillator produces 75 MHz, 40 fs at full width at half maximum (FWHM) pulse duration, 800 nm wavelength, and 10 nJ laser beam. The beam passes through a stretcher to increase the pulse duration hence decreasing the laser intensity, regen-amplifier for power amplification, and then is compressed back to the 40 fs pulse duration. The final output is a P-polarized laser pulse of 10 Hz, 40 fs, 800 nm, with 110 mJ maximum energy. Such a system provides a tunable laser power ranges from tens of gigawatts up to several terawatts. When using such a high laser power, the laser pre-pulse/contrast ratio must be considered. For this purpose, the noise around the main pulse was measured in the delay range of about -500 ps to 180 ps and the picosecond contrast ratio was found to be $1x10^{-8}$. The parasitic pulses arriving at greater than 1 ns delay around the main pulse were also measured and the nanosecond contrast ratio was

found to be $1x10^{-7}$. Consequently, the effects of both post- and prepulses, either pico- or nanosecond, can be ignored, and the output laser can be assumed to be pure femtosecond laser. A set of half waveplate and thin film polarizer positioned before the compressor enabled tuning the output laser energy. Outside the compressor, the laser beam goes through a 14 mm aperture shutter. The shutter was controlled by a delay time generator to allow a single pulse ablation mode. A 99.99%, 1 mm thick Sn was used as a target for this study. Sn metal is one of the most challenging elements when used for microfabrication by laser due to its low melting temperature (505 K), which makes the probability of causing permeant thermal damage and HAZ high. Target was placed on an XY translation stage inside a vacuum chamber (10^{-6} Torr) as shown in Figure 2.1. The laser entered the chamber through a quartz window then focused on the sample using a 10 cm plano-convex lens. The laser spot size on the target surface was measured to be 100 μm in diameter and kept constant throughout the entire experiment. The crater profile was measured using a White Light Profilometer (WLP) with a 1μm lateral resolution and 1 nm axial resolution.

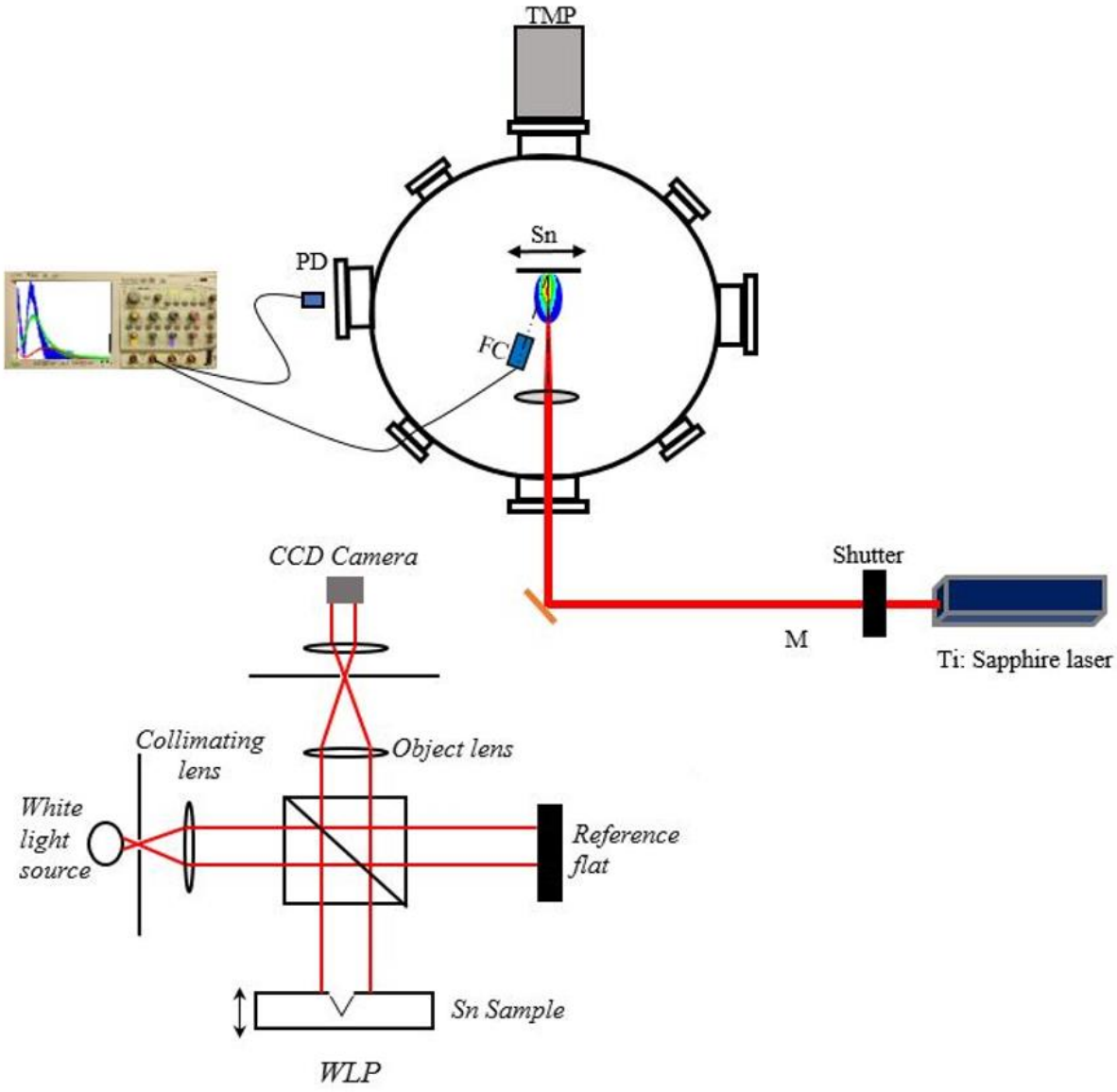

Figure 2.1 Schematic of the experimental setup

2.1.2 Effect of Ultrashort Laser Fluence on Laser Ablation

In principle, Laser as a dense energy source when it hits a target material it leads to ablation/material removal from that target, leaving an empty portion within that target called the crater profile. In this study, the ablation of the target materials was found to produce a crater profile that resembles the shape of the incident laser pulse, which is Gaussian in this study, as should be

intuitively anticipated. Not only the depth of this profile is dependent on the incident laser fluence but also the profile width was found to depends on the incident laser fluence. Figure 2.2, shows that by varying the incident laser fluence the profile characteristic dimensions (width and depth) vary accordingly. The larger the laser fluence the larger the crater width and depth. When using a laser for micromachine the thermal damage to the mater becomes a concern as it may cause permanent damage that results from material melting. In some applications such as solar cell fabrication, this molten material around the crater profile can act as a conducting bridge between films that usually stacked on top of each other leading eventually to misfunctioning the cell. The crater profiles shown in Figure 2.2 presents an absence of any ridges or up normal structures around the ablated spot even when creating a profile with several micrometers in depth using high laser fluence >100 mJ/cm^2. The later observation presents an important property of ultrafast laser that makes it a promising candidate for laser micromachining applications.

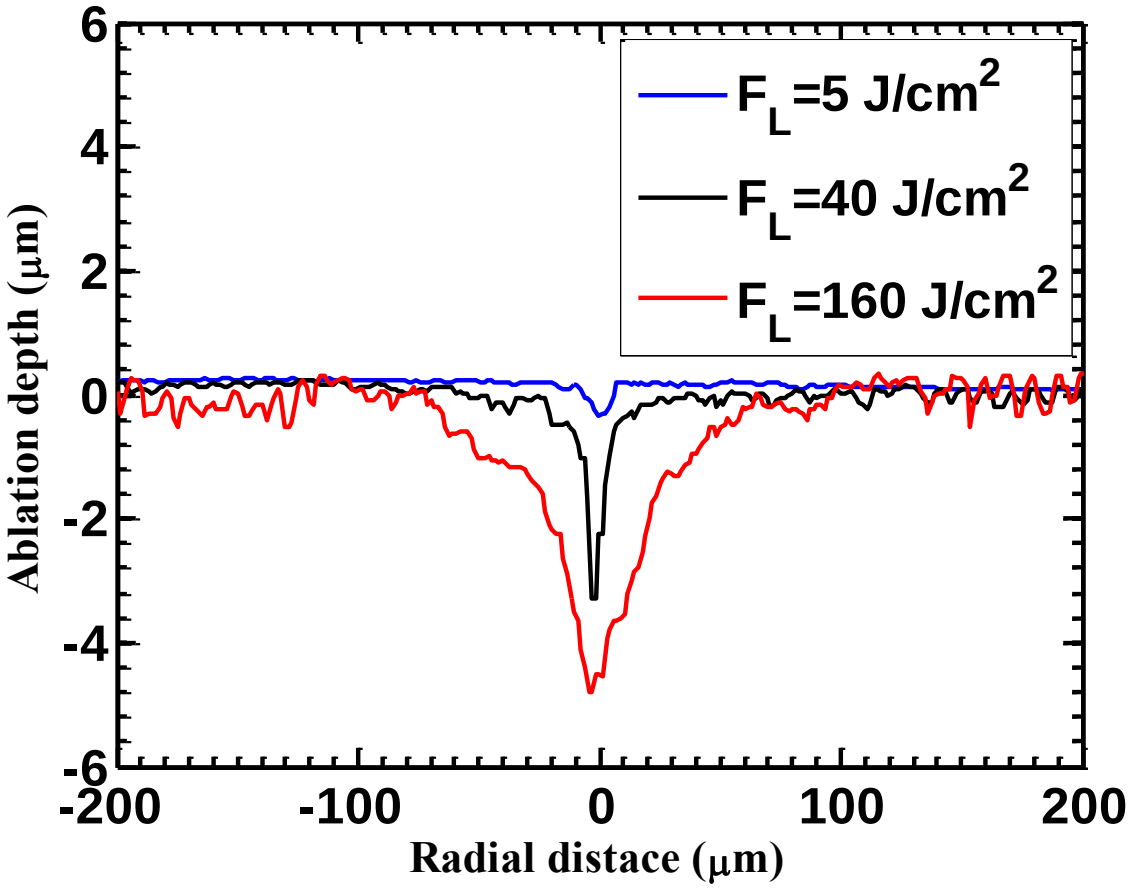

Figure 2.2 Laser ablation profile at different laser fluences

Laser ablation is a process that has a threshold value below which the material cannot be ejected from the target [39]. Once the laser fluence exceeds the threshold value for the irradiated target the material can be ejected so the ablation occurs. Accordingly, the increase in the crater width shown in Figure 2.2 is attributed to the increase in the energy of the wings of the incident laser pulse. This increases gradually when increasing the incident laser fluence, and when it exceeds the ablation threshold value for the Sn target, it causes material removal at the sides of the crater profile resulting in crater width increase. This will be referred to as the laser-wing effect [54]. This increase in the crater diameter was found to be a logarithmic function of the incident laser fluence, as indicated in Figure 2.3. This trend is in good agreement with previous work done on Indium-Tin oxide using 60 fs laser pulse and laser fluence from the ablation threshold value up to 2.72 J/cm^2 [55].

Along the propagating direction of the incident laser beam, the ablation depth was found to be affected differently by the incident laser beam. As shown in Figure 2.4, the increase in the ablation depth happens within a certain region. This region has a relatively low laser fluence (<250 J/cm^2) with respect to the entire laser fluence being used in this study. Using higher laser fluence showed no effect of the crater profile depth. This observation is interesting for high volume manufacturing (HVM) when the throughput becomes an important factor in recommending certain processes over others. Results in Figure 2.4 shows that increasing input laser energy doesn't translate into increasing the crater depth as it levels off at high laser fluence so for HVM and high throughput investing in laser energy could add additional cost with no manufacturing benefits while investing in increasing the laser frequency/repetition rate could aim to high throughput. After discussing the dependence of the crater profile shape, depth, and width on the incident laser fluence, it is important to consider the amount of mass removal dependence on the incident laser fluence. This can be accomplished by combining results from Figure 2.3 and Figure 2.2 and assuming that the crater profile has a Gaussian shape, which is a valid assumption. Based on results from Figure 2.2, the total ablated mass can be determined; results were calculated and plotted in Figure 2.5. At low laser fluence, the ablated mass was found to have a strong dependence on the incident laser fluence; this can be inferred from the sharp increase in the ablated mass that was observed at laser fluence less than ~100mJ/cm^2. While a slight increase was observed at higher laser fluence. This slight increase was observed in contrary to the ablation depth that was noticed to saturate at high laser fluence, this contradiction can be easily resolved by recalling results from Figure 2.3 that shows

the dependence of the crater profile on the incident laser fluence. Accordingly, this slight increase in the ablated mass is mainly due to the ablation that occurs in crater sides which is induced by the laser pulse wing-effect discussed earlier.

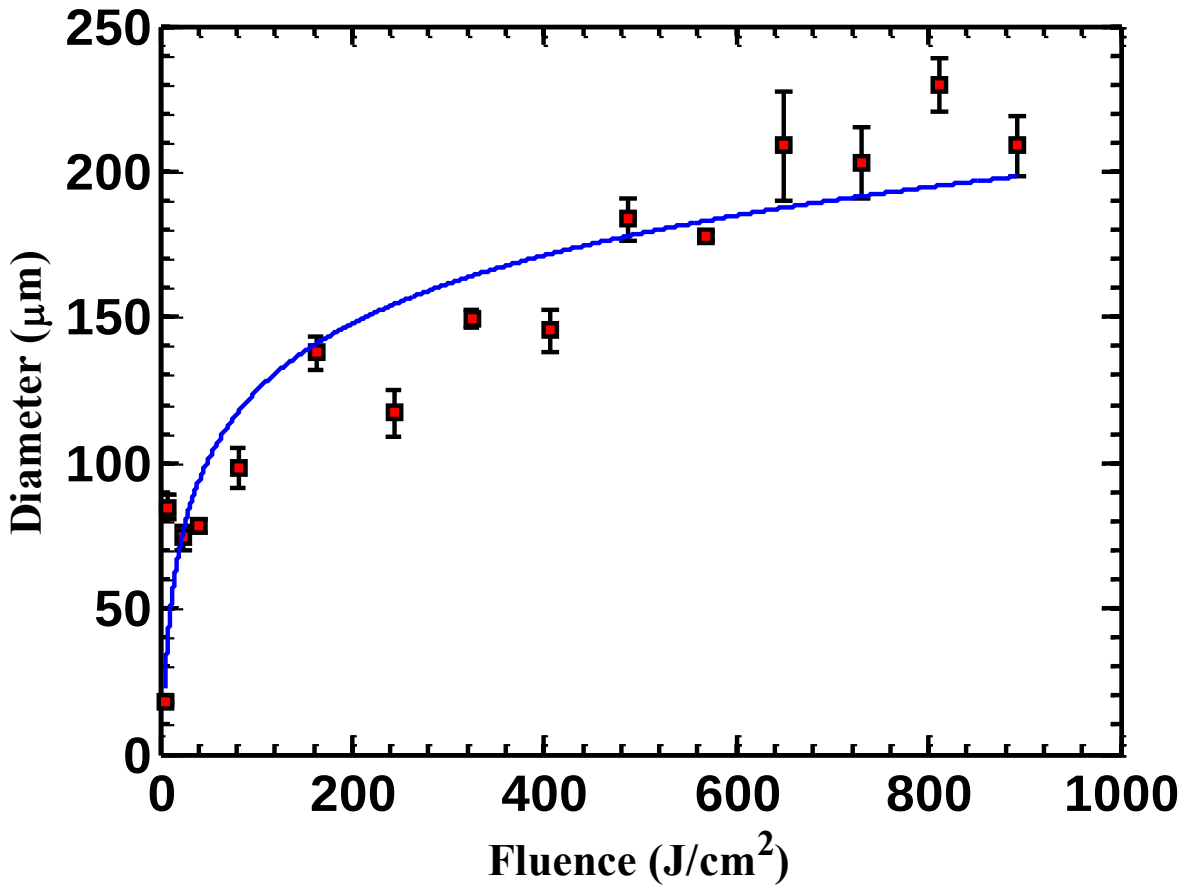

Figure 2.3 Effect of laser fluence on the width of the ablated profile

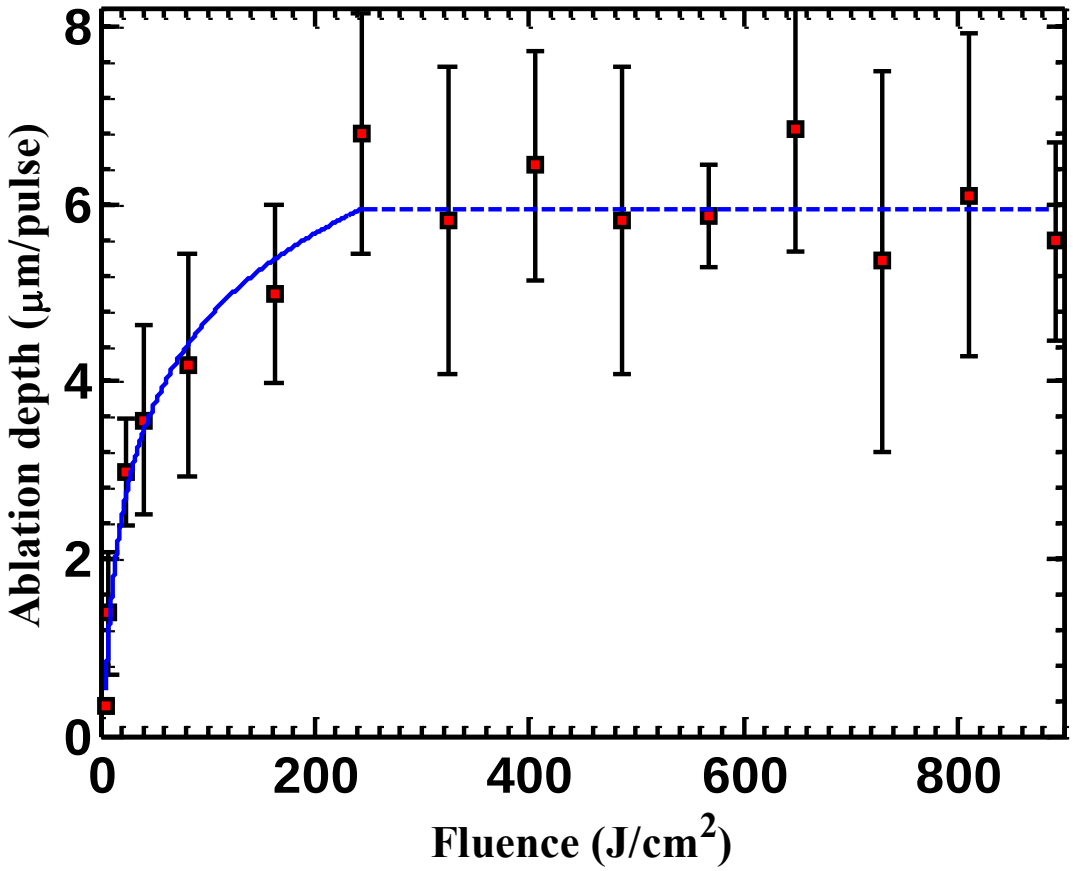

Figure 2.4 Effect of incident laser fluence on ablation depth

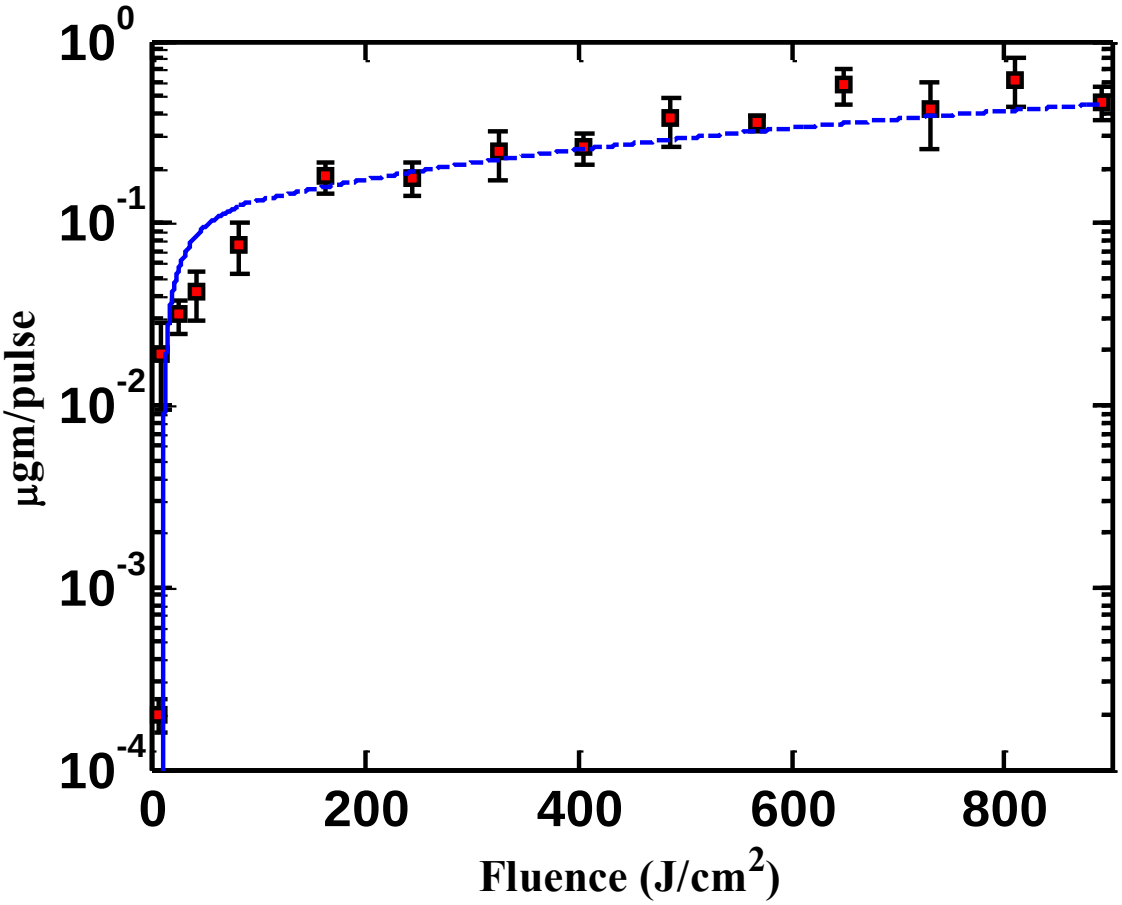

Figure 2.5 Ablated mass as a function of incident laser fluence

Understanding the dependence of the ablation crater profile and mass ablation on the incident laser fluence requires intensive investigation of the fundamental physics of laser-material interaction. In chapter 1 these fundamentals were discussed through the electromagnetic theory and two-temperature model standpoints. It worth mentioning here that, according to the electromagnetic theory not all the incident laser energy gets absorbed within the target material in practice, a fraction of this energy can only be absorbed. The material removal/ablation process occurs via depositing laser energy into a volume of target material determined by the optical penetration depth (l_s) and laser spot size (S). This heats the target material to an elevated temperature leading to melting and vaporization of the targets. During this process target's electrons gain energy from incident laser forming electronic compression wave. Energy exchange between these electrons and the target's ions creates ions with high energy consequently ionic pressure [16] causing the material to be heated and creating hot carriers (electrons and ions). These hot carriers propagate

inside the target and then transfer their energies to the lattice via creating optical and acoustic phonons. This process eventually leads to the removal/ablation of the target [41]. Previous studies [16] explored the change in the hydrodynamic properties of materials that occurs during laser irradiation using hydrodynamic simulation combined with two temperature model results showed that a big portion of the ablated mass is a direct consequence of the occurrence of material melting rather than material vaporization. Increasing the incident laser fluence leads to vaporizing the molten material rather than melt extra material. This leads to a decrease in the rate of material removal. Furthermore, the hydrodynamic simulation indicated that the gas phase propagates toward the free surface ahead of the molten material. As a consequence, this confines the liquid phase and limits the increase in the ablation depth and amount of mass that could be ejected from the target. Moreover, at low laser fluence, the laser absorption coefficient and/or the laser reflectivity varies with incident laser fluence and tends to be constant at high laser fluence as shown by numerical simulation to the microscopic properties of the material during laser irradiation [56] which limits the amount of laser energy that can be absorbed in the target, consequently limiting the amount of material that can be removed and the ablation depth that can be achieved. Conclusively, hydrodynamic simulation along with numerical simulation to the microscopic properties of material during laser irradiation is in good agreement with the findings of this work.

2.2 Nanosecond Laser Ablation

2.2.1 Experimental Setup

A 6 ns, 1064 nm, Nd:YAG laser system was used to study the characteristics of nanosecond laser-material ablation. The laser passes through a set of half-wave plate and a beam splitter, that outputs P-polarized light and tunable laser energy varies from 2 mJ to 300 mJ. As shown in Figure 2.6, the laser beam falls on the target through a quartz window, with a normal incident angle. The laser beam was focused on the target surface using a 100 mm plano-convex lens. The laser spot size on the target surface was measured to be 375 μm diameter and kept constant throughout the entire experiment. The experiment was conducted in a closed vacuum chamber (10^{-6} Torr). Two targets were used in this experiment, 1 mm thick and 99.99% Al and W. These two targets were chosen for this experiment because they have different thermal properties, mainly melting and vaporization temperatures. The target was placed on an XY translation stage. The crater profile

was characterized using White Light Profilometer (WLP). Moreover, a characterization of the molten layer resulted from the thermal effect induced by a laser pulse is reported and discussed.

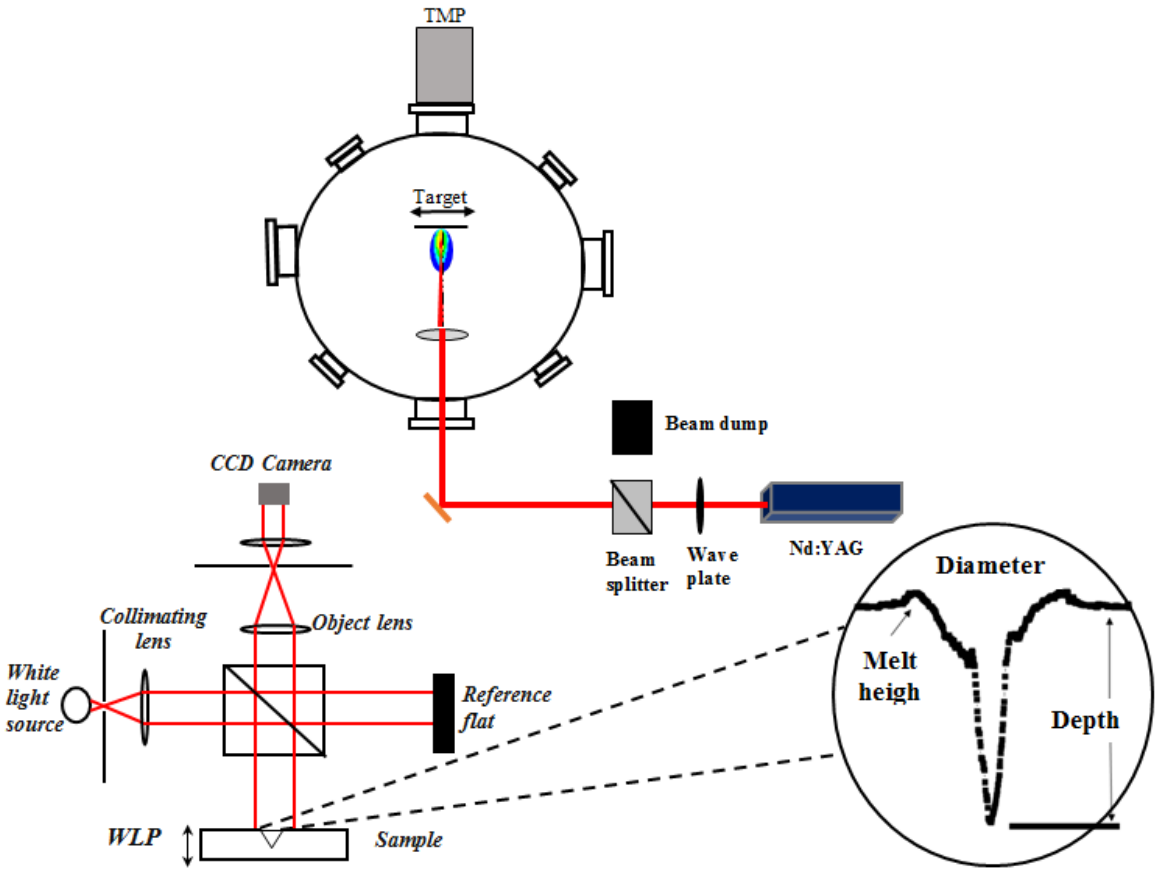

Figure 2.6 Schematic of the experimental setup.

2.2.2 Effect of Nanosecond Laser Fluence on Target Ablation

Nanosecond laser-material interaction is a process that differs from ultrafast laser-martial interaction this difference is due to the difference in the laser pulse duration. One main consequence of that difference is the thermal damage or the formation of HAZ that happens to the target material following nanosecond laser irradiation. Nanosecond laser irradiation is characterized by a pulse with a time duration long enough to permits thermal wave to propagate deep inside the target to cause thermal damage. This thermal damage is evident from the formation of molten material around the ablated spot which was completely absent as discussed in the

previous section in case of ultrafast laser irradiation. In this study, to illustrate the fundamentals of nanosecond laser-material interaction, two different targets (Al, W) that have distinct material properties such as melting temperature and heat of vaporization were exploited. Figure 2.7, shows the ablation profile resulted from nanosecond laser irradiation at different laser fluences. Similar to the ultrashort laser-ablated profile, the ablated profile shown in Figure 2.7 resembles the incident laser beam profile, i.e., Gaussian profile. Moreover, the profile obtained at different laser fluences has different depths as well as the width of. Widening the ablation profile is mainly attributed to the laser pulse wing effect that states that as the laser energy increases the energy at the wings of the incident laser pulse becomes high enough to contribute to the target ablation process and in case of long pulse duration such as nanosecond melting will occur as well. This is evident from the ablation profile of the Al that is shown to have a wide profile near to the surface then it narrows down. Such an effect was not noticed when irradiating the W target. W has a melting temperature four times higher than the Al, which minimizes the laser pulse wing effect at the energies considered in this work. A specific feature associated with long pulse duration laser such as nanosecond laser is the formation of a thick layer of molten material around the ablated spot. The morphology of this layer is irregular as it results from the splashing of the molten target's material due to the hydrodynamic pressure. This molten layer is represented in Figure 2.7 by the ridges around the ablated spot detailed discussion about this feature will be provided in the next sections. However, it worth mentioning here that these ridges around the ablated spot were not presented in the case of the ultrashort laser.

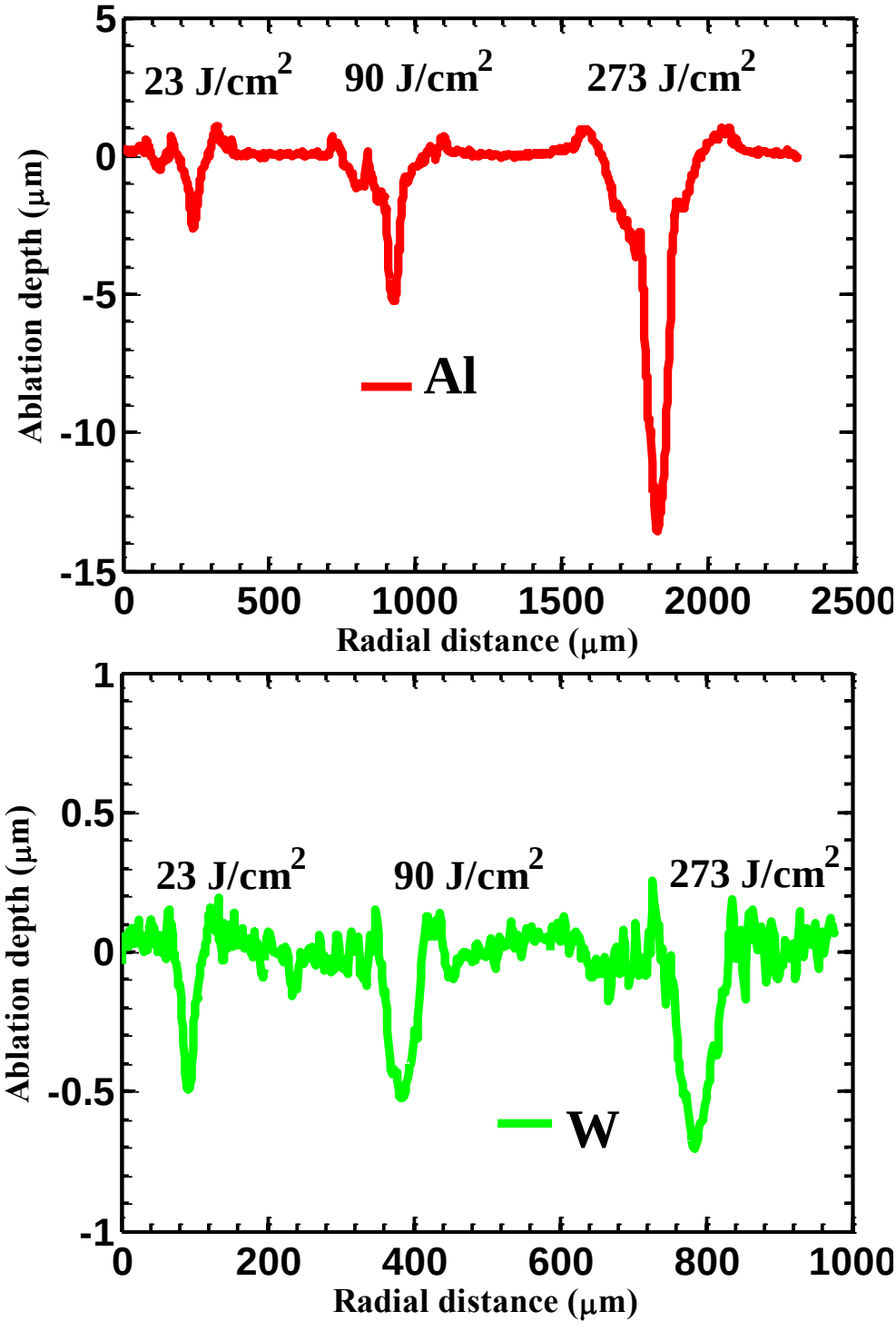

Figure 2.7 Laser ablation profile for W.

Investigating the dependence of the depth of ablation of both elements Al & W on the incident laser fluence reveals that Al has a high response to the incident laser fluence as it increases by more than one order of magnitude from 0.9 μm to 13 μm by increasing laser energy from 2 J/cm^2 to 300 J/cm^2. While for W, the response of the ablation depth to the incident laser energy is significantly weaker compared to Al as it increases only by four times over the same range of incident laser energy as shown in Figure 2.8. Comparing the ablation depth of Al and W at the same laser fluence it was found that Al has one order of magnitude higher ablation depth than W. It is also interesting to notice the difference in the trend of ablation depth between W and Al as the incident laser fluence increases, the W ablation depth levels off at laser fluence>20 J/cm^2 in contrary Al increases linearly with incident laser fluence. Furthermore, the rate of the increase in the ablation depth decreases with increasing the incident laser fluence. This reduction is obvious from the change in the slope of the curve in Figure 2.8 this is attributed to the formation of a high-density plasma during the early time of laser pulse duration. This plasma tends to shield the remaining part of the incident laser pulse from reaching the target, this phenomenon is known as the plasma shielding effect. As the plasma density reaches the critical density of the incident laser it tends to block the laser completely thus preventing any further laser penetration, as seen in Figure 2.8. and Figure 2.9. Comparing the slope of the ablation depth in Figure 2.8 for both Al and W indicates that the plasma shielding effect is more significant in W than in Al. This should be expected since W generates dense plasma compared to Al plasma.

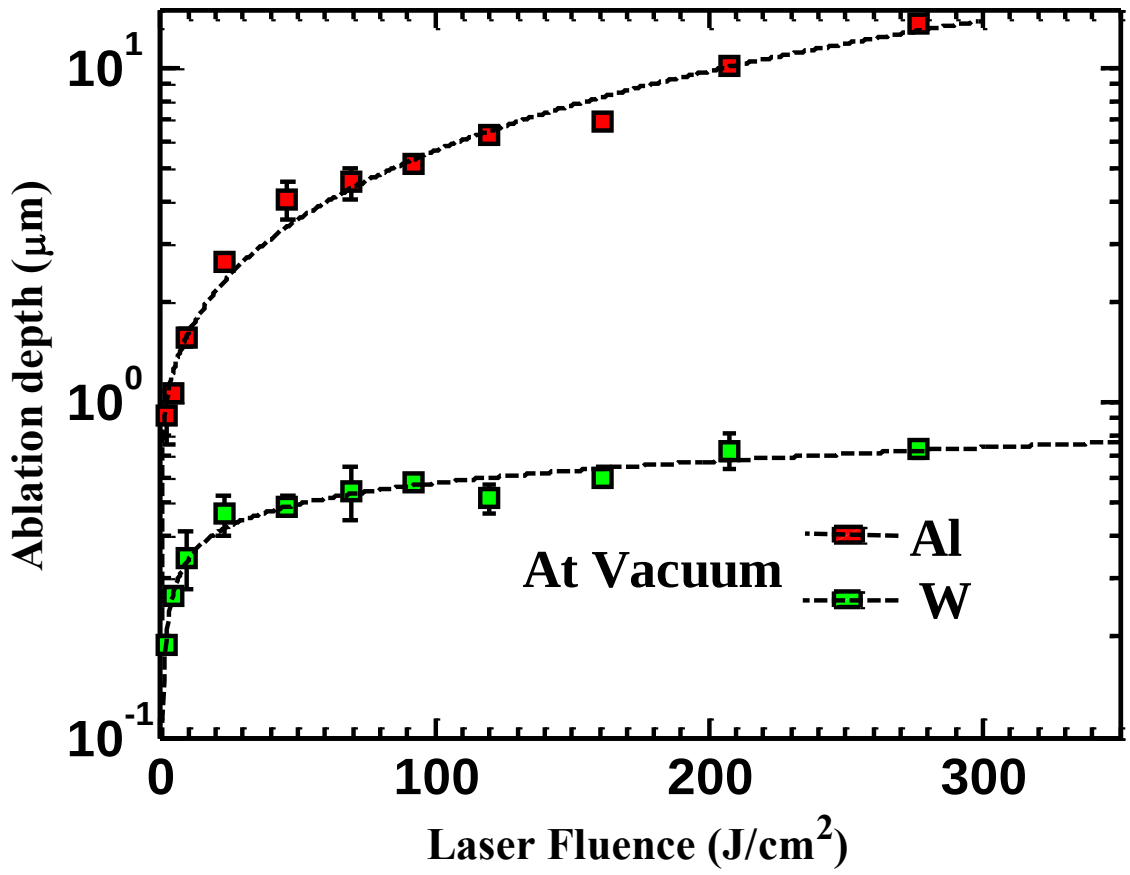

Figure 2.8. Effect of laser fluence on ablation depth.

The amount of the ablated mass removed from the target due to laser irradiation can be determined from combining results from Figure 2.8 and Figure 2.7 results, presented in Figure 2.9, which indicate that the amount of material removed from Al target increases from few nanograms up to microgram almost by three orders of magnitude while, the W shows increase in the amount of the ablated mass by less than two orders of magnitude, from 0.4 ng to 27 ng. For W, however, the ablation depth almost saturates at high fluence, the mass keeps increasing, this is due to the laser pulse wing effect discussed earlier. At laser fluences higher than 50 J/cm^2, comparing Al with W ablated mass, shows that the mass ablated from W is one order of magnitude less than mass ablated from Al.

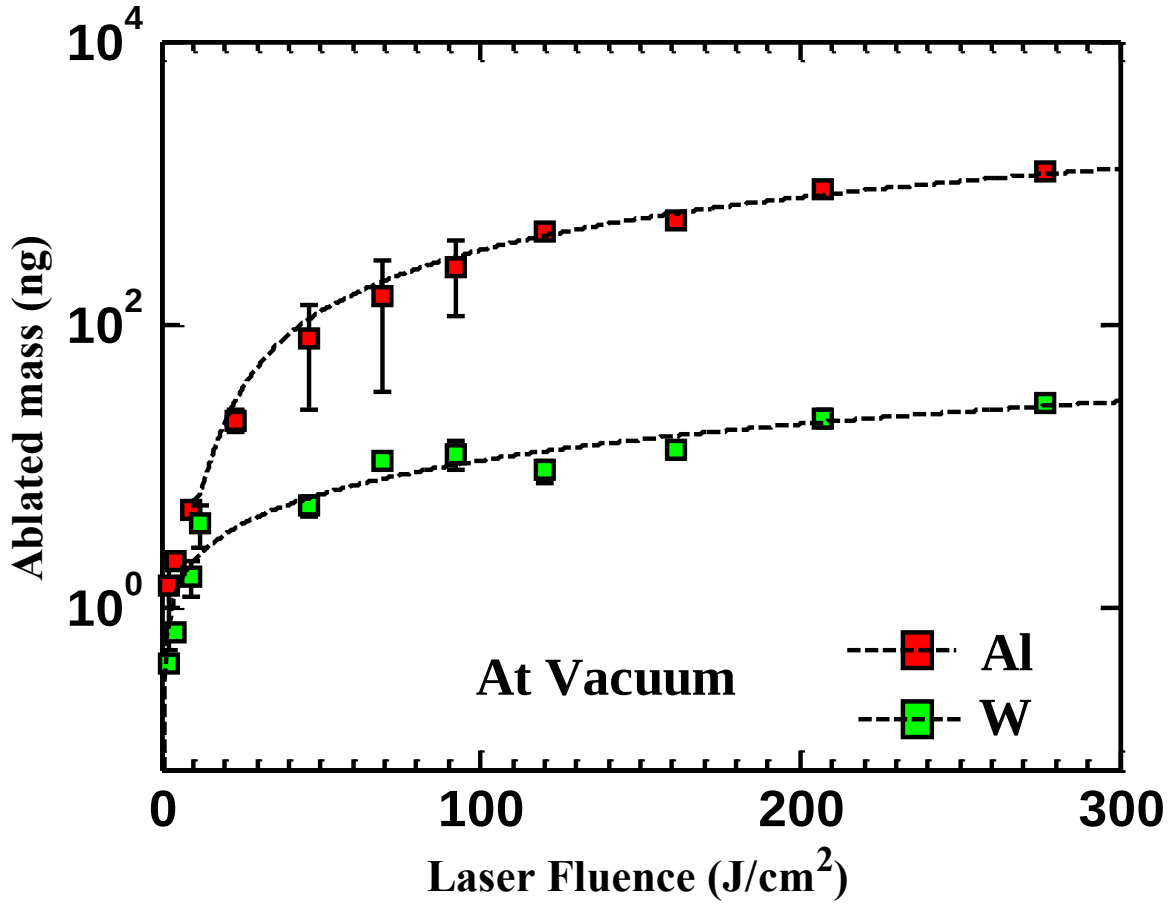

Figure 2.9. Ablated mass as a function of incident laser fluence.

As discussed earlier, the formation of HAZ characterized by an area that is thermally damaged is a phenomenon associated with the laser with long pulse duration such as nanosecond laser. So, it is important to elaborate more on the thermal damage associated with long laser pulse duration such as nanosecond lasers in this section. The thermal damage is evident in the formation of a molten layer around the ablated spot. This layer forms due to the splashing of the molten material and has an irregular morphology. In order to quantitively describe the amount of thermal damage that took place in the material, the maximum height of the molten layer was measured as a function of the incident laser fluence. The results are shown in Figure 2.10, the melt height trend is similar to the ablation depth in Figure 2.8. Quantitively, the melt height increases for Al from a fraction of micrometers up to one micrometer while, the melt height increases by <3 times from 100 nm to 270 nm in the case of W. The ratio between the ablation depth and height of the melt shows that for Al at laser fluence <20 J/cm^2 this ratio is <4 while, at higher laser fluences this ratio increases

significantly. For W, this ratio is comparable overall the entire laser fluence range used, typically <3.

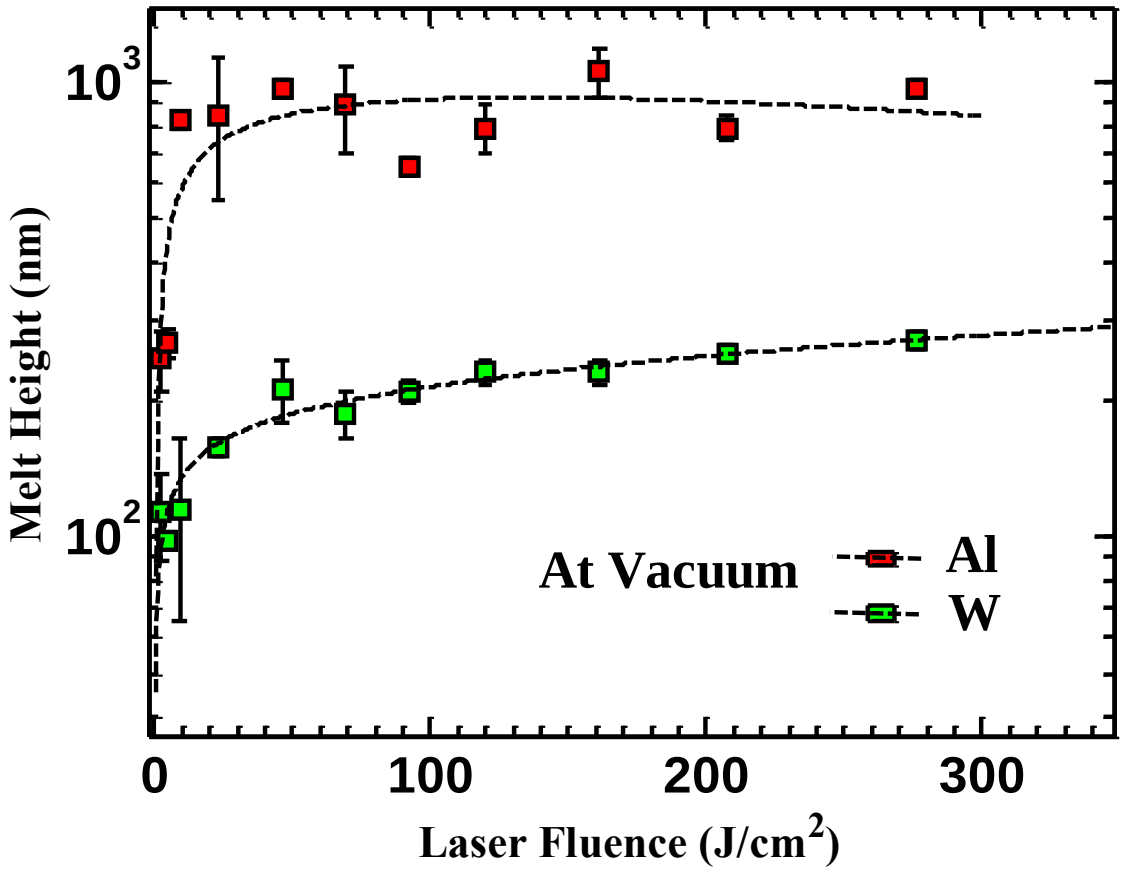

Figure 2.10 The effect of incident laser fluence on the height of the molten material.

Results discussed in this section confirm that W is more resistive to erosion induced by incident laser fluence compared to Al at the same incident laser energy which is mainly due to the differences between Al and W material properties. The results discussed above are consistent with the physical and thermal properties of the materials studied here, W and Al. The high erosion resistance of W is due to its high heat of vaporization which is 3 times higher than the heat of vaporization for Al. Also, W has a high melting point (which is ~4 times higher than Al), this makes W more resistant to the thermal effect induced by a long pulse laser. Results presented in Figure 2.8 & Figure 2.9 are shown to have a certain dependence on incident laser fluence independent of the target material. At low laser fluence, the dependence of the ablated depth and

the ablated material is shown to be a logarithmic while, at high laser fluence it tends to be linear, due to the plasma shielding effect. This effect is significant at high laser fluence at which the formed plasma becomes dense and acts as a barrier between the target and the incident laser. The plasma shielding effect limits the additional amount of material that can be removed from the target due to the minimum energy reaching the target surface [16].

CHAPTER 3. ULTRASHORT LASER PRODUCED IONS

3.1 Background

The physics of laser energy coupling with target material has been studied in the literature. As a consequence of laser energy absorption in the target material, material ablation takes place, and plasma plume forms. This plasma plume propagates in the opposite direction to the incident laser pulse. The propagating plume contains different kinds of particles such as clusters, neutral, and charged particles. The dynamics of the plume represented by ion flux, ion velocity, the angular and temporal distribution of the ejected ions are essential for many applications [57] to name a few of them, pulsed laser deposition (PLD), laser-induced breakdown spectroscopy, ion implantation, light source generation, and ion source generation, etc. Plume dynamics are complicated topics to study because it depends on laser properties (wavelength, pulse duration, and energy), material properties (thermal conductivity, the heat of vaporization, atomic mass and number), and irradiation conditions (ambient conditions, spot size). In the following, a study on the ion dynamics is provided which indicates the effect of laser and material properties.

3.2 Properties of Ultrafast Laser Produced Ions

3.2.1 Experimental Setup

In this study, 800 nm, 40 fs (FWHM), P-polarized Ti:Sapphire laser was used to irradiate pure targets of 99.99% (C, Al, Cu, Mo, Gd, W). Such a system provides a tunable laser power ranges from tens of gigawatts up to several terawatts. When using such a high laser power, the laser pre-pulse/contrast ratio must be considered. For this purpose, the noise around the main pulse was measured in the delay range of about -500 ps to 180 ps, and the picosecond contrast ratio was found to be $1x10^{-8}$. The parasitic pulses arriving at greater than 1 ns delay around the main pulse were also measured, and the nanosecond contrast ratio was found to be $1x10^{-7}$. Consequently, the effects of both post- and pre-pulses, either pico- or nanosecond, can be ignored and the output laser can be assumed to be pure femtosecond laser. A set of half waveplate and thin film polarizer positioned before the compressor enabled tuning the output laser energy. As shown in Figure 3.1, the incident laser was focused on the targets with 45º incidence angle via a 40 cm plano-convex

lens that yields an elliptical spot with a size of $3x10^{-4}$ cm^2. The targets were placed on a remotely controlled XY translation stage to have a fresh surface and kept under vacuum (10^{-6} Torr). The ion dynamics were studied by measuring the ions' TOF using the IC (Kimball Physics, Inc., model FC-71A). The IC was mounted on an angle manipulator allowing changing the measurement angle from $-\pi/2$ to $\pi/2$ with respect to normal to the target surface to measure the angular resolved ion flux and velocity. It was kept 9 cm away from the target surface and negatively biased at –40 V to repel the electrons and only collect the ions. The IC has a front aperture with a 5 mm diameter hole. The output signals from FC were acquired across a 50 Ω load resistor using a 1 GHz oscilloscope (Tektronix TDS5104). A fast photodiode was used to trigger the oscilloscope simultaneously with the laser pulse to record the ion signals. A few laser shots were used initially to clean the target surface at first. The number of cleaning laser shots varies from target to target, so the criterion was to keep the cleaning laser shots until the signal becomes stable. The ion signals reported below are obtained after cleaning and averaged over 10 successive laser shots for good statistics.

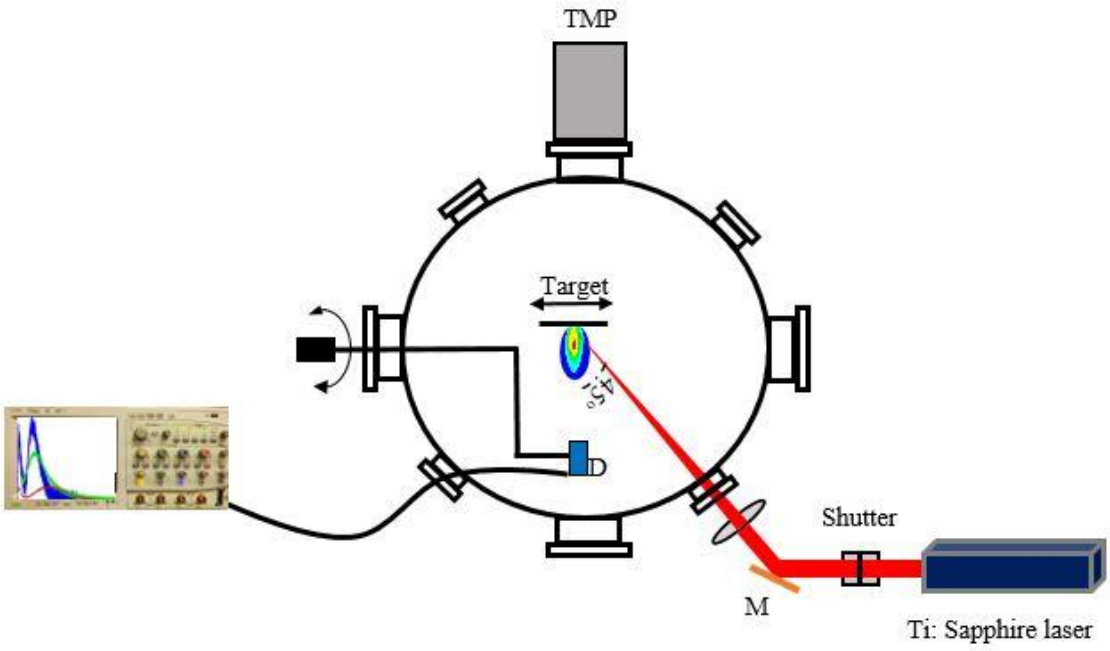

Figure 3.1 A schismatic of the experimental setup

3.2.2 Effect of Material Properties on Ultrafast Laser-Produced Ion Flux and Ion Velocity

Laser irradiation to target material induces ion ejection, the properties of these ions are studied using the Time of Flight (TOF) technique. TOF is a technique that depends on measuring the time duration the ions take to reach the detector surface after they are ejected from the target. Based on the distance from the target to the detector, the velocity of the ejected ions is determined. Furthermore, the output signal intensity of the detector is proportional to the ion flux that is being ejected and collected by the detector. In this study, different targets with different material properties were chosen to investigate the effect of material properties on the dynamics of ultrafast laser-induced ions. Ion TOF signal resulting from irradiating targets material (one at a time) using 1.2 J/cm^2 incident fluence is presented in Figure 3.2. Results in Figure 3.2 show that ion flux, indicated by the peak intensity of the TOF signal, is dependent on the target material as targets with low atomic weights elements are producing more ion flux than targets with high atomic weights. Furthermore, independent of the irradiated target there are two peaks were observed for each TOF signal. It is inferred from this dual peak TOF signal that two types of ions were generated as a result of laser irradiation based on their velocities, which is determined from the delay time of each peak; these two types of ions will be referred to as slow/thermal ions and fast/hot ions. Slow ions' TOF profile was found to follow Shifted Maxwellian Distribution (SMB), represented by Equation. 3.2.2.1. Fitting the fast ion signal with SMB distribution resulted in nonphysical meaning parameters, and it was found to be best fitted with a Gaussian distribution represented by Equation. 3.2.2.2.

$$I_1(t) = A_1 t^{-n}\, exp[-\beta(\frac{L}{t} - v_d)^2] \tag{3.2.2.1}$$

$$I_2(t) = A_2\, exp[-0.5(\frac{t-t_0}{w})^2] \tag{3.2.2.2}$$

The Gaussian peak parameters are simple with t_o being the peak center, and w being the peak width and A_1 is the amplitude. The SMB distribution depends on plasma ion temperature represented by $\beta = \frac{M}{2k_B T_i}$ which is determined by the laser fluence. The variable n is indicative of plasma density with high n values corresponding to high plasma density and vice versa. The distance L from the target to the IC was kept at 9.2 cm. Both v_d, A_1 and A_2 are fitting parameters, with v_d controlling the peak shift. From the fitting, it was found that w tends to increase with increasing target atomic

mass at the same laser fluence. The T_i was found to vary from 0.5 to 12 eV. The ejection of two types of ions, based on their velocity with each species, has a fingerprint distribution indicates the existence of different ion ejection mechanism following the absorption of laser energy in target materials, independent of the type of target material, as it will be discussed thoroughly in the following sections.

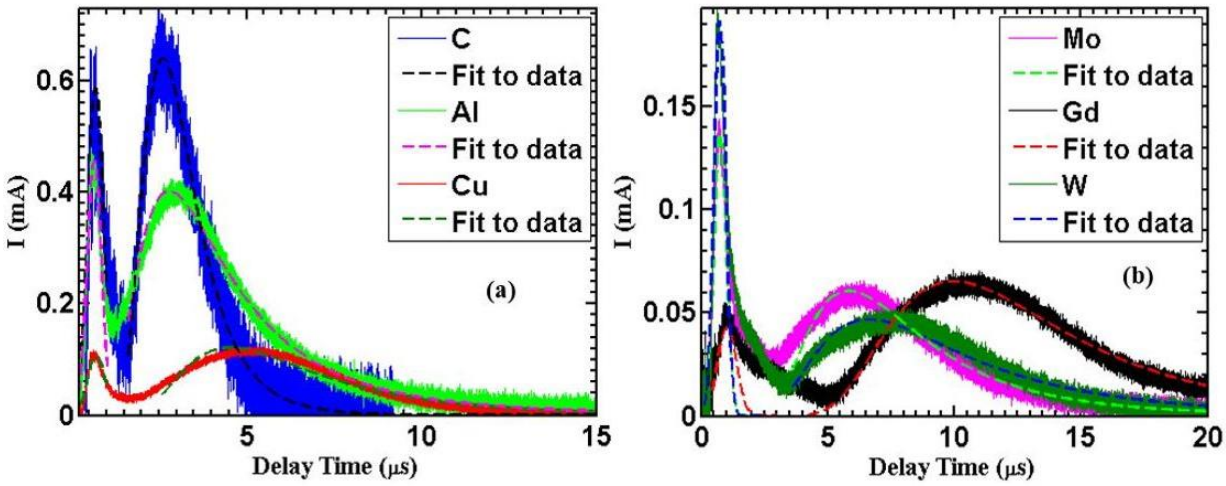

Figure 3.2 Ion time of flight for different materials

The total charge collected by IC is represented in Figure 3.3 as a function of the target's element atomic weight, by integrating the ion TOF *U(t)* of both fast and slow ions independently and divided over the load resistor $R= 50\ \Omega (\int U(t)dt\ /R)$. It is evident from the results in Figure 3.3 that the ejected total charge (slow and fast ions) shows the same trend as they tend to decrease with increasing the target atomic weight for the same laser intensity. The highest charge yield results from laser-carbon interaction, which is one order of magnitude higher than the lowest charge yield results from laser-gadolinium interaction. It is also noteworthy that the total flux is dominated by the slow ion flux.

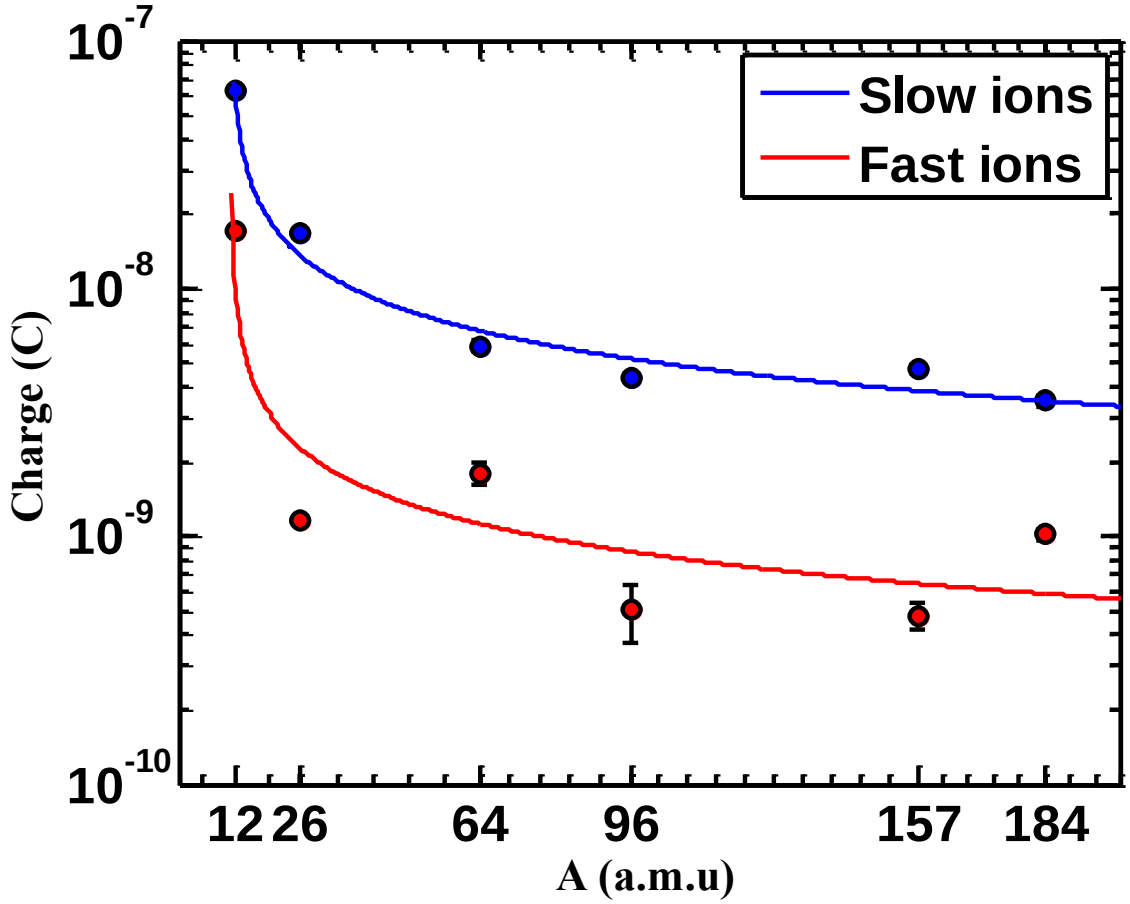

Figure 3.3. Detected ion flux as a function of the target's atomic weight

The maximum ion charge, Q_{max}, that can be ejected from target material depends on the fraction of laser energy that can be absorbed in the target, and the optical skin depth $\left(l_s \approx \frac{c}{\omega_{pe}}\sqrt{2\nu_{eff}/\omega}\right)$, that determines along with the laser spot size, *S*, the volume in which the laser energy is deposited. The optical skin depth as discussed in chapter 1 is a function of laser properties indicated directly by laser frequency, ω, and material properties represented by effective collision frequency, ν_{eff}, and electron plasma frequency ω_{pe}. The volume at which the laser energy is deposited can be assumed to be the hottest part of the target material; consequently, the free charged particles are mainly ejected from this volume. Furthermore, the ejected particles have different ionization states that determine the total ion charges. Q_{max} can be calculated by assuming that all the atoms (n_a) within a volume ($S \times l_s$), will be ionized, yielding average ionization state, Z_{avg}, of ions in the plume, the maximum ions charge can then be given by Equation. 3.2.2.3:

$$Q_{max} = eZ_{avg}n_aSl_s \qquad (3.2.2.3)$$

However, Eq 3.2.2.3 gives a simple expression to the maximum charges that can be ejected from the target material, it does express the charges that can be detected by the IC. In practice when calculating the fraction of the charges that can be detected by the ions several factors have to be considered. The first factor is the distance between the detector (IC) and the target's surface, as this factor has a pronounced effect in reducing the number of detected charges. This effect is mainly due to electron-ion recombination and ion flux attenuation as the ion travels toward the detector. The first effect can be neglected since the experiment was carried out under vacuum (10^{-6} Torr), and the second effect can be scaled as $1/r^2$, where *r* is the distance between the IC and the target surface. The second factor is the spatial distribution of the ejected particles, which is given by Eq. 3.2.2.4:

$$Q(\theta) = Q\left[\frac{1+tan^2(\theta)}{1+\beta^2\,tan^2(\theta)}\right]^{3/2} \qquad (3.2.2.4)$$

where β is the ratio between the longitudinal and transverse axis of the propagating plasma plume, which partially comprises the ejected ions. The value of β determines the shape of the plume and it varies from 2 to 5 [23] based on the target material as will be discussed. Consequently, The final

expression of the total ion charges collected by the detector (IC) in terms of the plasma plume geometry, the laser parameters, and the material properties is given by can be expressed by:

$$Q_{\max} = 2\times 10^{7} \frac{\int_{\theta_{\min}}^{\theta_{\max}} \left[\frac{1+\tan^2(\theta)}{1+\beta^2\tan^2(\theta)}\right]^{3/2} d\theta}{\int_{-\pi/2}^{\pi/2} \left[\frac{1+\tan^2(\theta)}{1+\beta^2\tan^2(\theta)}\right]^{3/2} d\theta} \frac{1}{r^2} \frac{S}{\sqrt{\omega}} \left(\frac{\rho Z_{avg}}{A}\right)^{3/4} \qquad (3.2.2.5)$$

The first term in Eq. 3.2.2.5 represents the fraction of charged particles that can be detected by the IC. The second term is a geometrical factor that represents the attenuation of charged particles during their flight. The third term shows the dependence of the ejected charges on the laser parameters (ω). While, the fourth term shows the dependence of the ejected charged particles on material properties (ρ, A, and Z_{avg}). The average ionic charge state Z_{avg} can be determined by solving the Saha equation [58] as showing in Figure 3.7. A comparison between the calculated charge and the measured charge is shown in Figure 3.4 as a function of the target's atomic weight. A comparison between the calculated charge and the measured charge shows that the calculated charge qualitatively is in a good agreement with the measured value as it exhibits a similar trend while qualitatively the calculated charge appears to be overestimated. One reason for that is the uncertainty in calculating the laser penetration depth where the maximum value of the collisional frequency was used ($\nu_{ei} \approx \omega_{pe}$) [2,4,25], instead of correcting for the collision frequency decrease with increasing electron temperature [59] ($\nu_{ei} \alpha T_e^{-1.5}$). Moreover, It was assumed that the incident laser energy is uniformly distributed; thus, all the atoms inside the volume ($S \times l_s$) will be ionized. However, in practice, neutral particles form in addition to charged particles. Eventually, the main aim of this model is to show how the ejected ions depend on the target atomic mass weight.

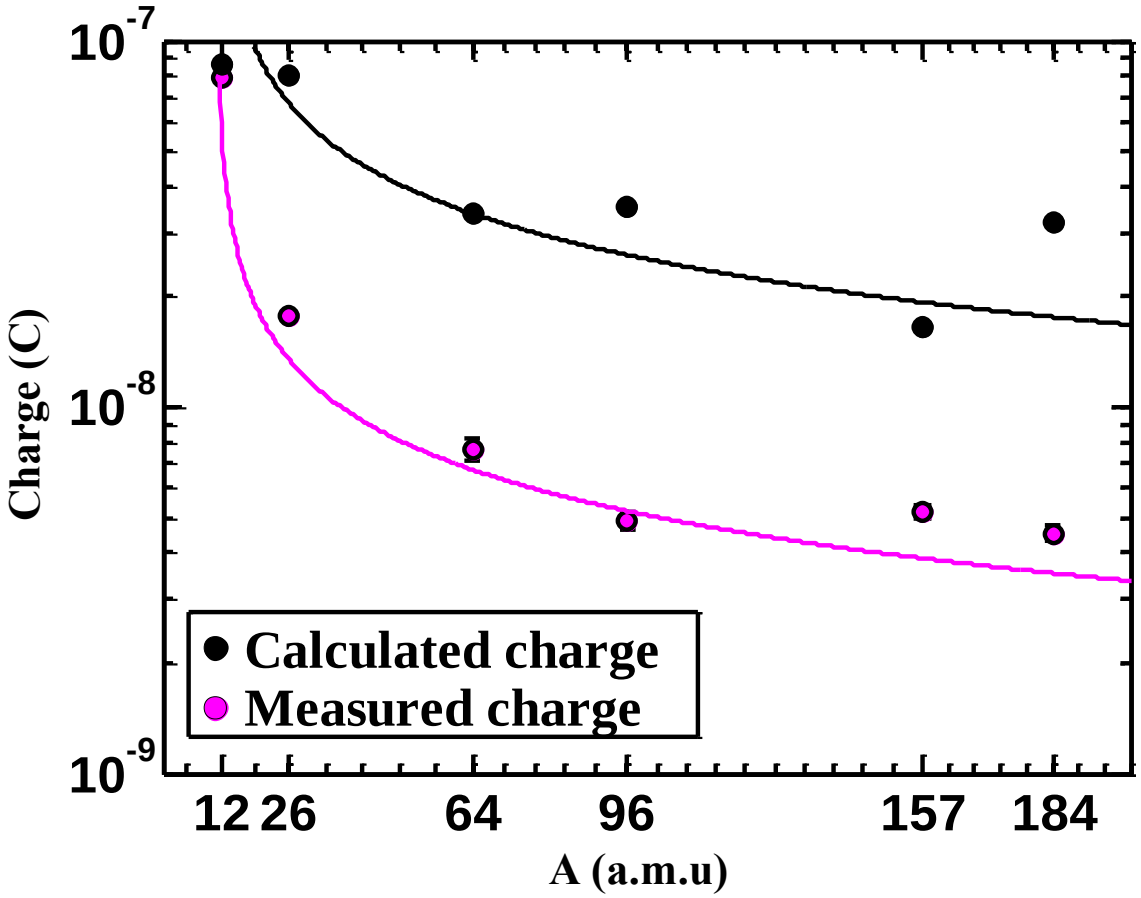

Figure 3.4 Comparison between theoretically calculated and experimentally measured ion flux

Figure 3.5 shows the ion velocity as a function of the target atomic weight. The velocity of both fast and slow ions tends to decrease as the mass of the ions increases, as should be intuitively expected ($V \propto M^{-0.5}$) assuming the same amount of laser energy is absorbed in each material. The highest velocity is shown for carbon, the lightest element among the other elements in this study, to be ~4 × 10^5 m/s and 5 × 10^4 m/s for fast and slow ions, respectively. Another observation is that the velocity of fast species is almost an order of magnitude higher than that of the slow species.

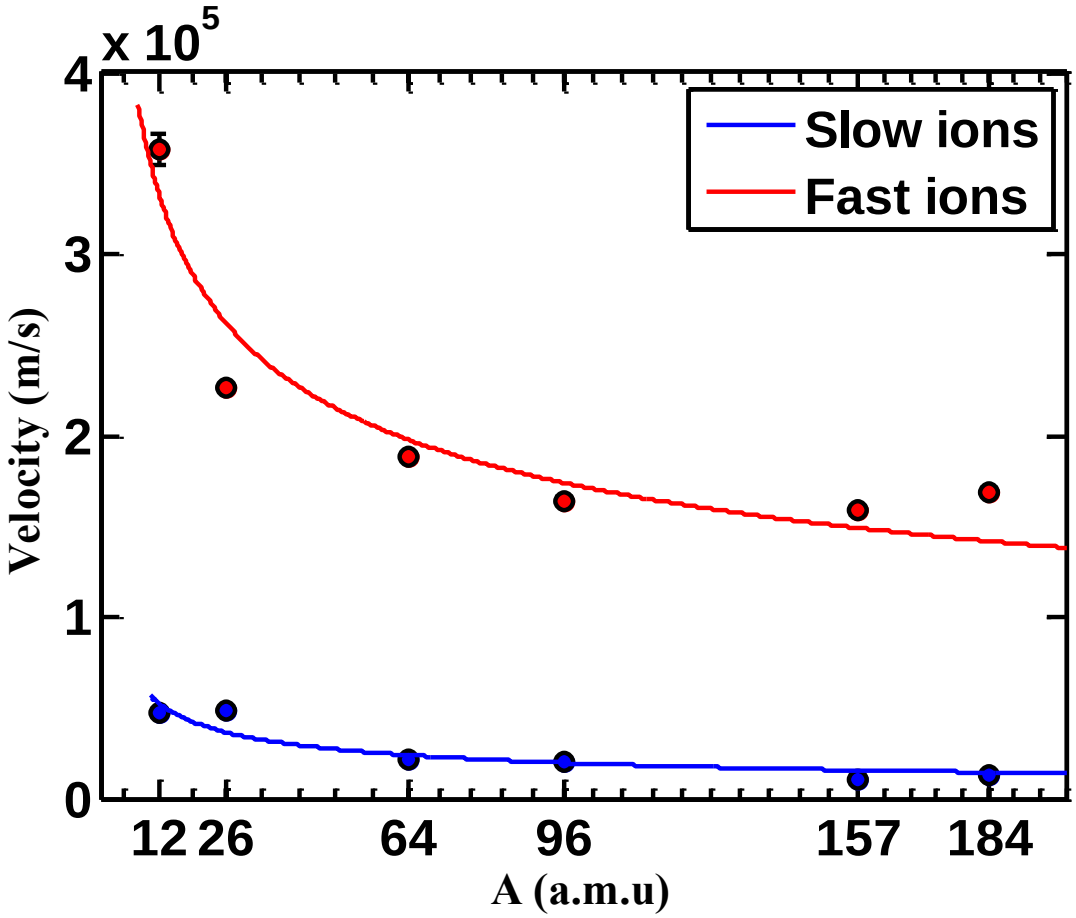

Figure 3.5. Ion velocity as a function of the target's atomic weight

3.2.3 Effect of Ultrafast Laser Fluence on Ion Flux and Ion Velocity

The effect of the incident laser fluence on the ejected ion flux is quite similar for both fast and slow ions, as shown in Figure 3.6. The ejected ions were found to increase linearly with incident ion flux. However, two distinct regions were observed. In the first region (<5 J/cm^2), the ion flux increases sharply with increasing the laser fluence. In the second region (>5 J/cm^2), the increase rate of the ion flux is significantly less. The trend in the ion flux is in good agreement with previous work. It should be emphasized that the IC signal is sensitive to the charge not to the number of ions. In other words, IC doesn't differentiate between two singly ionized ions or one doubly ionized ion; in practice, both will generate the same signal intensity. Then the question becomes the increase of the detected ion charge is due to the increase in ion charge state or the number of

ejected ions? As discussed earlier, the number of the ejected ions is limited by the number of the existed atoms in a volume given be optical skin depth, l_s, and laser spot size, S. Moreover, the charge state of ions is a function of the electron temperature that is a function of the incident laser fluence. On the other hand, the ejected ions average charge state, Z_{avg}, can be determined from the Saha equation using the approach given by and assuming the nonideal effect of plasma [23].

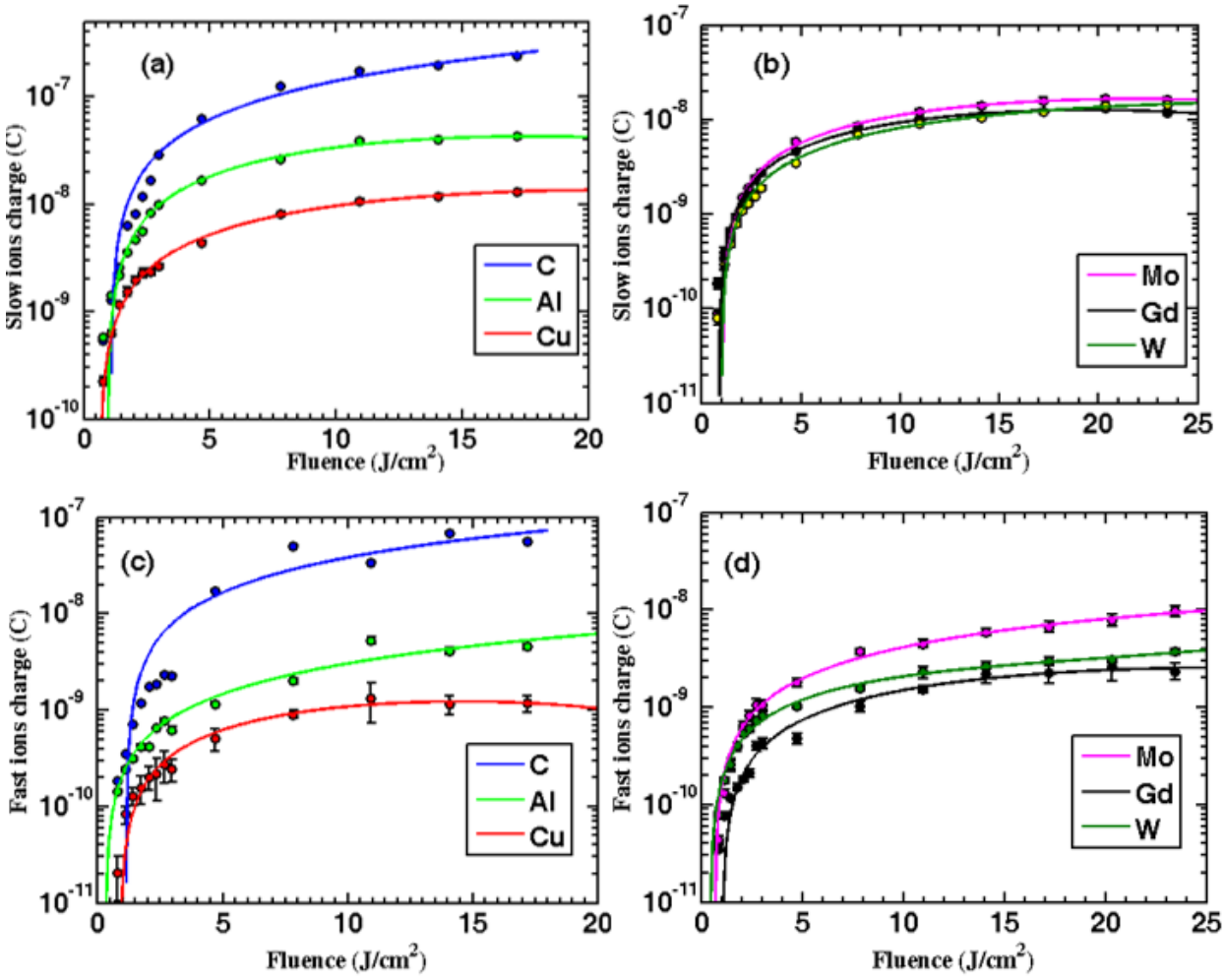

Figure 3.6 effect of incident ion fluence on both slow and fast ion flux for different materials

The solution of the Saha equation resulted in three distinct regions for Z_{avg} as shown in Figure 3.7 for Al as an example. In the first region, the Z_{avg} increases abruptly with increasing T_e. This increase continues until the outermost electrons are released from the atom (for Al there are 3 electrons at

the outer shell). afterward, further ionization becomes challenging to obtain, thus the second region shows saturation in Z_{avg}. The third region shows that a slight enhancement in the Z_{avg} can be obtained at even higher T_e. From this discussion, the reader can draw an explanation to the dependence of the ejected ion flux on the incident laser fluence. In the first regime, increasing laser fluence tends to increase the electron temperature; thus, it induces ions with higher ionization state. In this regime the laser fluence effect on average charge state hence the detected ion charges, is evident by comparing the first region in Figure 3.7 ($T_e < 11\ eV$) with the first region in Figure 3.6 ($fluence < 5\ J/cm^2$), where both trends (Z_{avg} and ion flux) show a rapid increase in average charge state and flux, respectively. Also, experimentally ions with higher ionization states were detected and measured at this regime [38]. Moreover, the effect of ion's ionization state on the total charge is investigated here theoretically by Eq.3.2.2.5. In the second region that corresponds to laser fluence higher than $5\ J/cm^2$ and an electron temperature that lies between $11\ eV$ and $30\ eV$, the ionization state of the emitted ions is independent of the incident laser fluence (see second region in Figure 3.7); thus the slight increase in the detected ion charge in the second region is due to increasing in the number of ions rather than altering the ionization state of the ions. Based on this observation, a new regime, corresponding to the third region in Figure 3.7, can be expected at laser fluence higher than 40 J/cm^2. In summary, the observed increase in the detected ion flux in Figure 3.6 is associated with the average charge state of the ions obtained in Figure 3.7, rather than increasing the number of ejected ions.

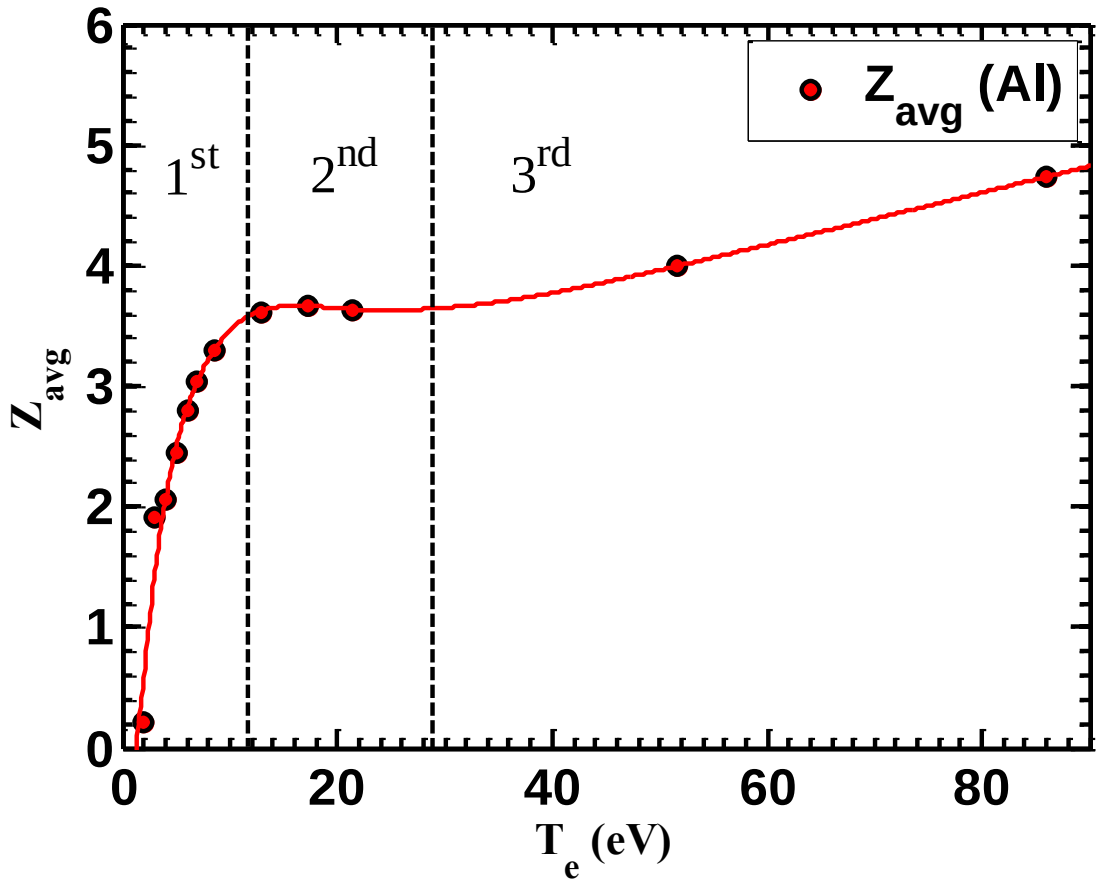

Figure 3.7. The average charge state of ejected ions as a function of electron temperature obtained from solving the Saha equation..

In contrary to the fast and slow ion flux dependence on incident laser fluence, the effect of the incident laser fluence on the velocity of the slow ions was found to be different from the effect it has on the fast ions. Slow ions were found to increase sublinearly with increasing laser fluence in a good agreement with [8], whereas fast ion tends to increase linearly with increasing laser fluence then it levels off at laser fluence >5 J/cm^2, as illustrated in Figure 3.8. This difference in ion behavior requires the existence of two different mechanisms to eject the ions from the target. The first mechanism is due to thermal vaporization, at which the charged particles are ejected from the target due to energy relaxation between electrons that first absorb the incident laser energy via inverse Bremsstrahlung and then transfer it to the lattice. Once the ions gain enough energy to overcome the target binding energy, they will be blown off/ablated from the target with speed

$C_s = \sqrt{\frac{Z^* k_B T_e}{M}}$ in the order of 10^4 m/s (where Z^* and M are the charge and mass of the ejected ion). Although the ejection mechanism of slow ions is well understood, there is a lack of understanding of the origin of fast ions. In some literature, it has been attributed to the hydrocarbon contaminations on the target surface; and in other literature, it has been attributed to the reheating of the ablated plume that can be induced by the falling tail of the incident laser pulse.

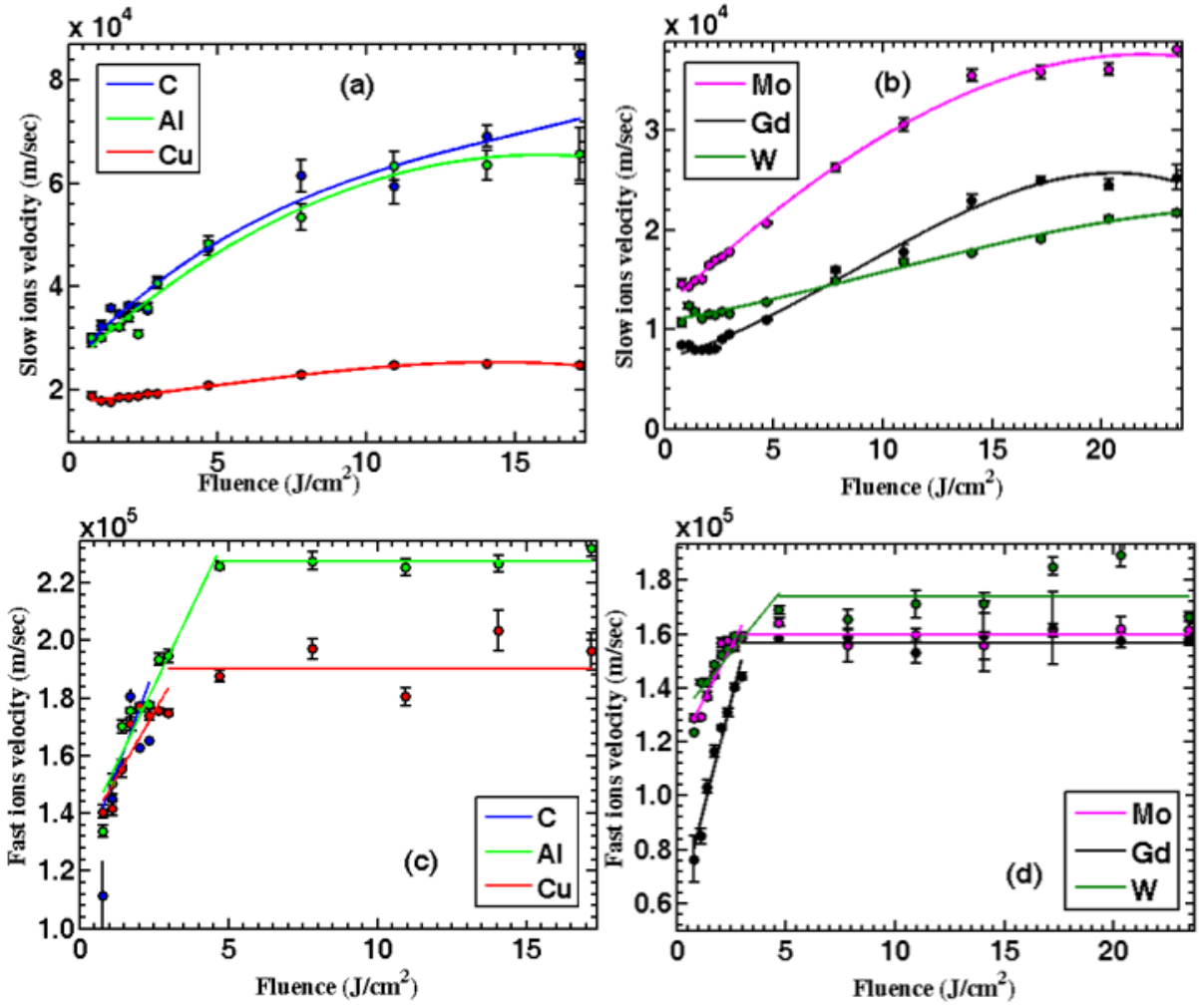

Figure 3.8. Effect of incident laser fluence on both fast and slow ions' velocity

In this work, in order to resolve this confusion, multiple laser shots were used at first to clean the target surface to rule out the possibility that these ions are due to surface contamination. Moreover,

ablation of the target with an ultrashort laser pulse (40 fs) rules out the possibility that the incident laser pulse can interact with the ablated plume. To further illustrate this point, it is worth mentioning here that the time scale of interaction of incident laser energy with target material: ionization to target's electrons at such laser intensity (fluence divided by laser pulse duration) presented in this work occurs within few femtoseconds typically much shorter than the incident laser pulse duration (in this work pulse duration is 40 fs). In the presence of the free electrons, the absorption of laser energy becomes dominated by inverse Bremsstrahlung, the electron-electron equilibrium time is typically the order of magnitude of the reciprocal of the electron plasma density; for metal $\omega_{pe}^{-1} \sim 10^{-2}$ fs, it is once again much shorter than the incident pulse duration. Consequently, the electron energy transfers lattice and then forms a plasma plume. Relaxation between the free electron and the lattice ions occur, and so the plasma forms in picoseconds. This time is longer than the incident laser pulse duration [8]. Accordingly, for subpicosecond or femtosecond laser pulse duration the laser pulse ends before the formation of the plasma plume consequently the plasma plume heating due to laser-plasma interaction as a potential mechanism to eject fast ions can be ruled out. Below, the main mechanism behind the ejection of fast ions will be discussed.

Following the time frame of the laser-material interaction discussed above that states during the laser pulse duration electrons cannot transfer their energy to the ions so this forms two species of particles based on their energies, these two species are hot electron are having temperature T_h and cold ions. This in turn will induce an ambipolar electric field this field ejects the ions out of the target material. To visualize this picture, it can be considered as a capacitor consists of two plates of opposite charges hot electrons and cold ions and in between, there is an electric field. This electric field exerts accelerating force on the ions, leading to their ejection and acceleration. On contrary, it exerts a decelerating force on the ejected electrons, leading to decelerating the electrons. The ions will gain energy as they follow the electrons resulting in decelerating the electrons. Thus, the acceleration process will be slowed down or truncated, as presented by many studies. Once the ions catch up with the electrons, no more acceleration can occur to the ions, and ions continue drifting with constant velocity. Based on the model discussed by Gibbon [1], the ions maximum kinetic energy is dependent on the ions' charge state and hot electron temperature, T_h, and can be estimated as follows:

$$E_{max} = Z_{avg} T_h \qquad (3.2.3.1)$$

Plotting the ion's kinetic energy that was measured experimentally, as shown in Figure 3.8, versus the obtained average charge state of the emitted ions, shown in Figure 3.7, shows that the ion kinetic energy is a linear function of the emitted ion average charge state, as shown in Figure 3.9. The obtained result is in agreement with the model provided by Gibbon [43] and presented by Eq. 3.2.3.1. In summary, it can be concluded that the establishment of an ambipolar time-dependent electric field by hot electrons and ions is the driving mechanism for hot ions ejection from the target. Recently, extensive work was dedicated to detecting and studying this electric field by P. Nica et al. [60].

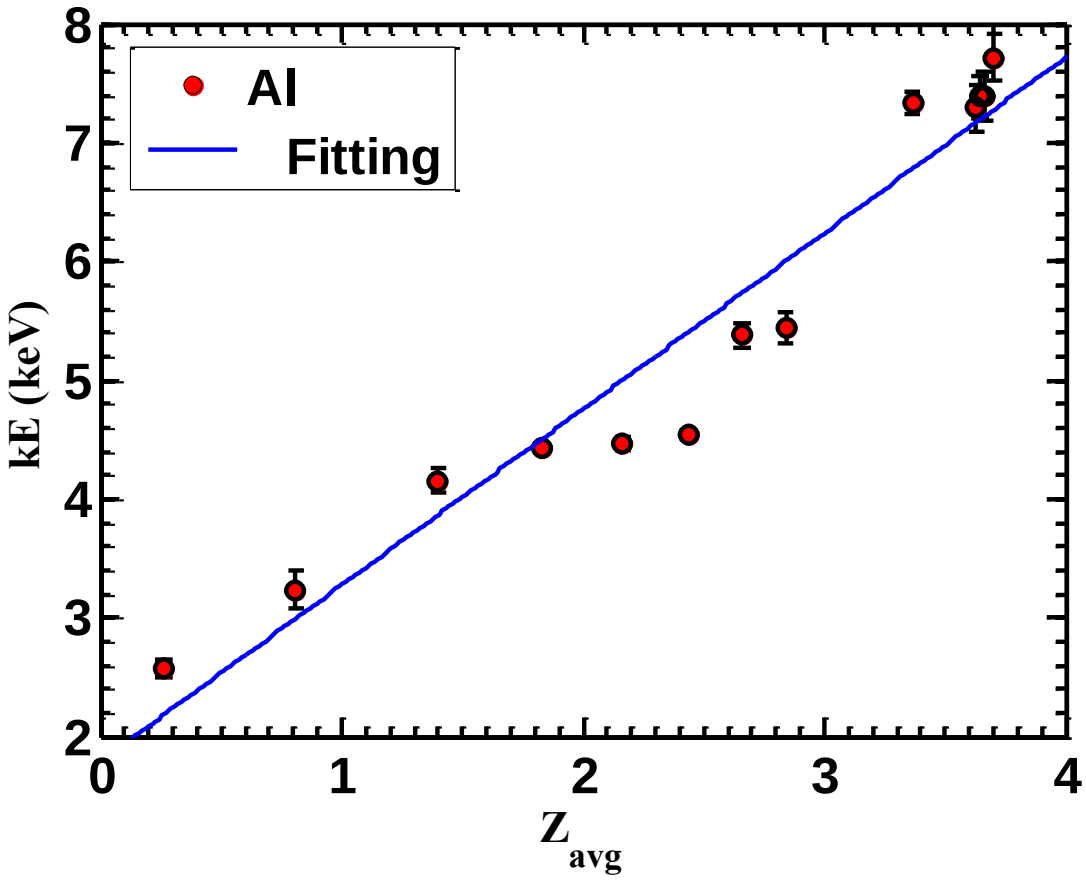

Figure 3.9. Fast ions kinetic energy as a function of ions' average charge state

The two ejection mechanisms that are discussed in this work, namely thermal vaporization and the ambipolar electric field, which are responsible for the ejection of slow and fast respectively, were both observed for all elements that are experimented in this work and also under the same conditions of laser irradiation (ambient condition and laser fluence). However, the relative contribution of each of these two mechanisms in ion acceleration is a function of incident laser fluence and the target's material properties. This is illustrated by taking the ratio of fast ions' kinetic energy to the slow ions' kinetic energy for each element as a function of incident laser fluence, as shown in Figure 3.10. Results indicate that the ambipolar electric field mechanism becomes significant at intermediate laser fluence ~ 4 J/cm^2 while less significant at higher laser fluence. At lower fluence, the ambipolar electric field effect increases with increasing laser fluence, as shown in Figure 3.10. This is explained from Figure 3.8 that shows fast ions velocities level off at fluence higher than 5 J/cm^2, while slow ions velocity continues to increase. At higher fluence, it is possible that both peaks overlap, and it becomes difficult to resolve the two peaks unless a higher ionization state is reached to enable fast ions' velocity to increase instead of leveling off, as the maximum kinetic energy that can be gained by fast ions is a function of average ionization state (Equation 3.2.3.1). Moreover, results in Figure 3.10 show that the ratio is small for light elements and increases as the ion's mass increases. This explains the difficulties encountered in previous work, wherein it was hard to resolve the fast ion peaks for both C and Al, and why it was more noticeable in the case of Cu.

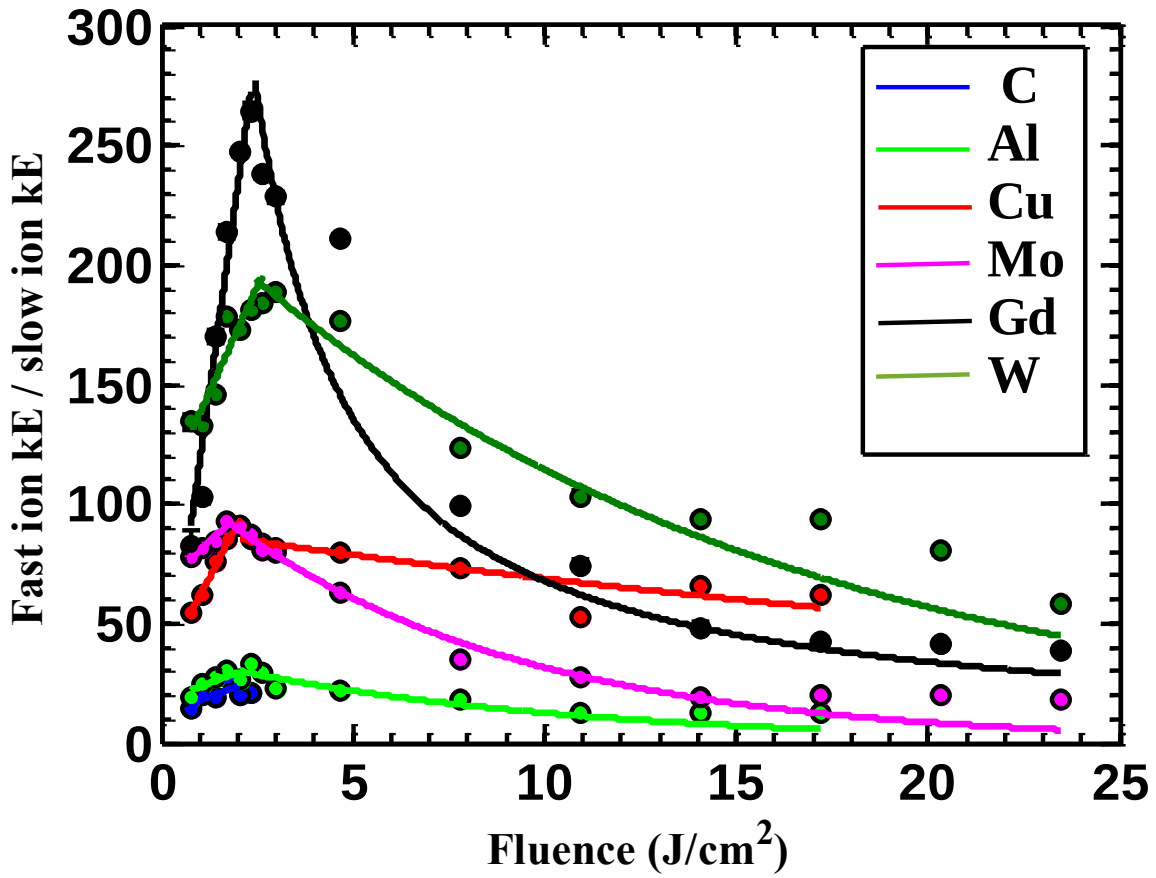

Figure 3.10 The ratio between fast ion kinetic energy and slow ion kinetic energy as a function of incident laser fluence

3.2.4 Angular Distribution of Ultrashort Laser-Produced Ion Flux and Ion Kinetic Energy

As the TOF technique enables studying the time distribution of laser-induced ions, it can be also used to study the angular distribution by varying the angle of ion detection while maintaining the distance between the target to IC/detector. Results in Figure 3.11 show the angular distribution of both fast and slow ions measured from -90º to +90º with respect to normal to the target surface. The angular resolved ion flux illustrates that the maximum ion flux peaks at an angle normal to the target surface. It can be concluded that the emission direction of the ablated plasma plume is independent of the ablated target's material, and the ion emission mechanism. Furthermore, along with other published work, the angular distribution of the ejected ion flux is also independent of the laser incident angle, which is 45º in this case. The angular distribution of the ablated plume was studied assuming an isentropic, adiabatic self-similar expansion of the ablated plume at the

end of laser pulse. This model provided an analytical formula of the shape of the emitted plume given by Eq. 3.2.2.4, discussed earlier. Fitting the experimental data with this model provides valuable information about the geometry of the emitted plume through the forward peaking factor β. Once again β is defined as the asymptotic ratio of the longitudinal and the transverse axis of the plume. In other words, if $\beta>1$, this means the plume is forward peaked and has an elliptical shape, although if $\beta<1$, that means the ablated plume is more like a spherical shape. Fitting to the experimental data, it was found that β varies from 2 to 5, depending on the material. Furthermore, fast ions were found to be more collimated than thermal ions.

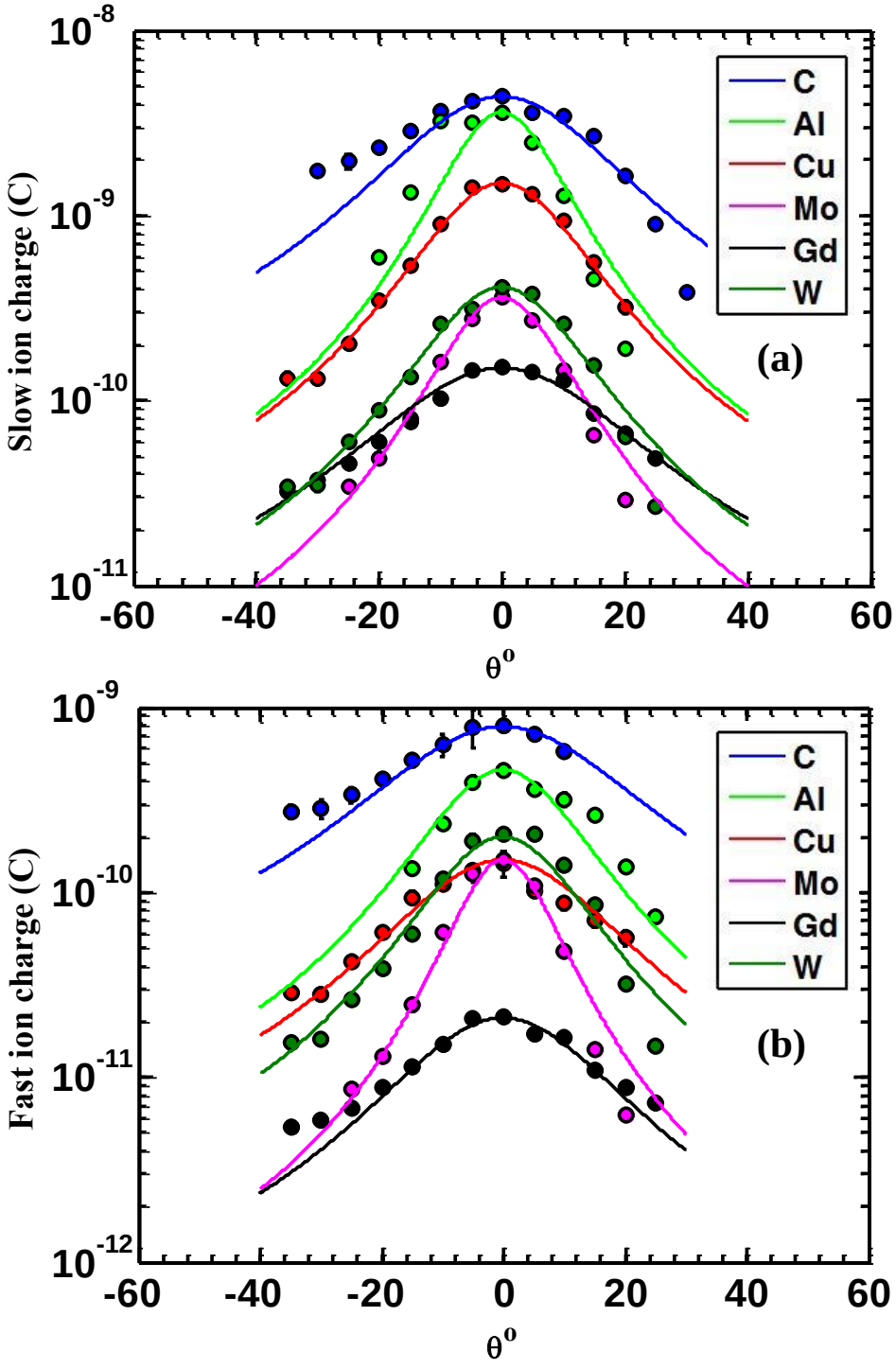

Figure 3.11 The spatial distribution of ejected ion flux

Similarly, the angular distribution of ion kinetic energy was also measured. Eq. 3.2.2.4 was found to provide a good fitting to the ion kinetic energy angular distribution, as shown in Figure 3.12.

Fast ions were found to be more collimated than slow ions. The angular distribution of both fast and slow ions has a peak that is normal to the target surface. The kinetic energy angular distribution is consistent with the ion flux angular distribution obtained above.

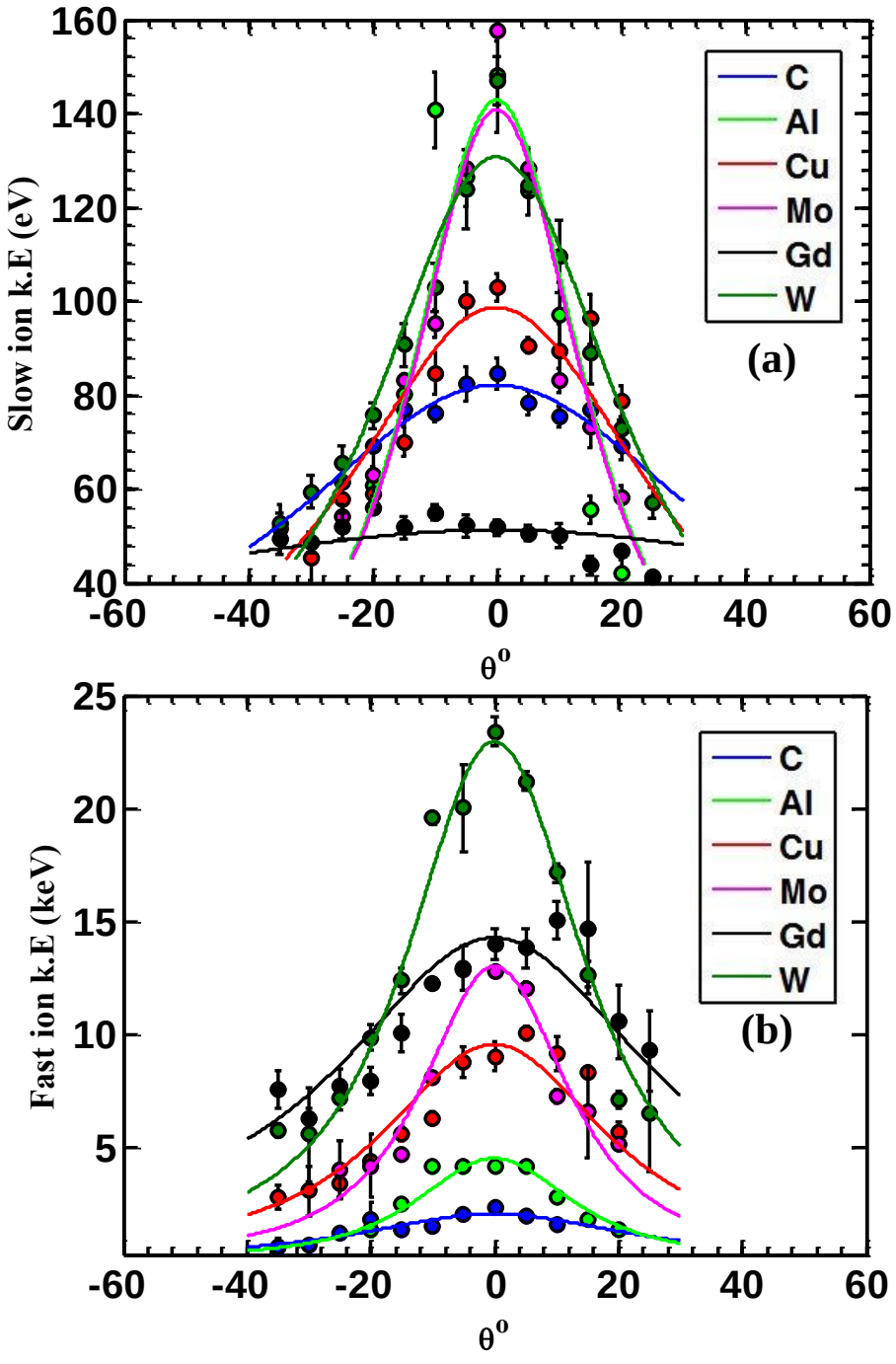

Figure 3.12. The spatial distribution of ejected ion's kinetic energy

CHAPTER 4. PROPERTIES OF NANOSECOND LASER-PRODUCED IONS

4.1 Properties of Nanosecond Laser Produced Ions

4.1.1 Experimental Setup

A 6 ns, 1063 nm, P-polarized Nd:YAG laser was used to generate ions from solid different targets. The laser pulses pass through a set of half-wave plates and a beam splitter that outputs P-polarized light and tunable laser energy varies from 2 mJ to 300 mJ. As shown in Figure 4.1, the laser beam incident on the target surface at a 45º angle measured from normal to the surface. A 20 cm Plano-convex lens was used to focus the laser beam on the target surface to a 200 μm diameter. The spot size was kept constant during the entire experiment. Five targets were used to study the laser-produced ions with 99.99% purity (Al, Fe, Co, Mo, and Sn). The targets were mounted on a remotely controlled X-Y translation stage to assure a fresh surface and to avoid drilling the target. The experiment was performed in a vacuum chamber ~1.0×10^{-4} Torr.

An IC has a 2 mm aperture diameter mounted on an angle manipulator 11.4 cm away from the target surface was used to measure the ions' TOF. A 30 V negative bias voltage was used to repel the electrons and detect only the ions. The output signal was measured and stored using a 50 Ω load resistor 5 GHz oscilloscope.

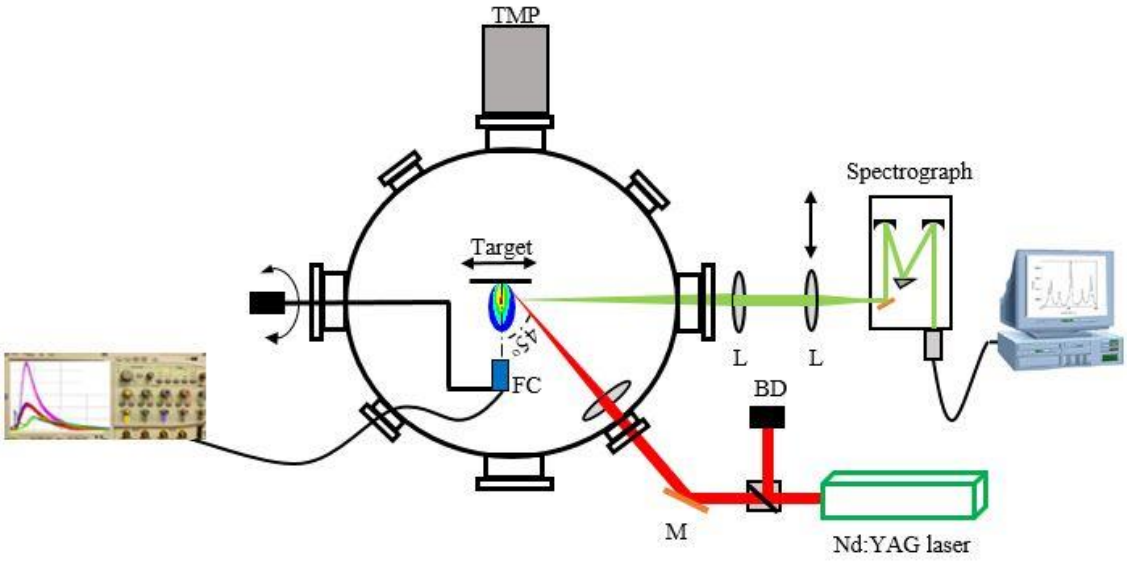

Figure 4.1 Schematic of the experimental setup

4.1.2 Effect of Material Properties on Nanosecond Laser-Produced Ion Flux and Ion Velocity

The effect of material properties on nanosecond laser-produced ions was studied using different target material with different material properties (i.e., melting temperature, sublimation energy, the heat of vaporization, thermal conductivity, etc.). This effect is evident from the TOF measurement of the ions shown in Figure 4.2. Both the amplitude and the peak location of the TOF signal is strongly dependent on the target material, indicating a dependence of both ion flux and ion velocity on the properties of the target material. Moreover, heavy metals exhibit two peaks corresponding to the existence of two species of ejected ions (i.e., the fast and slow ions). On contrary, light metals yield only one type of ejected ion, with properties consistent with slow ions. Slow ions were found to follow the Shifted Maxwell Boltzmann distribution (SMB) given by Eq. 3.2.2.1, whereas fast ions were found to be best fitted by Gaussian distribution function given by Eq. 3.2.2.2.

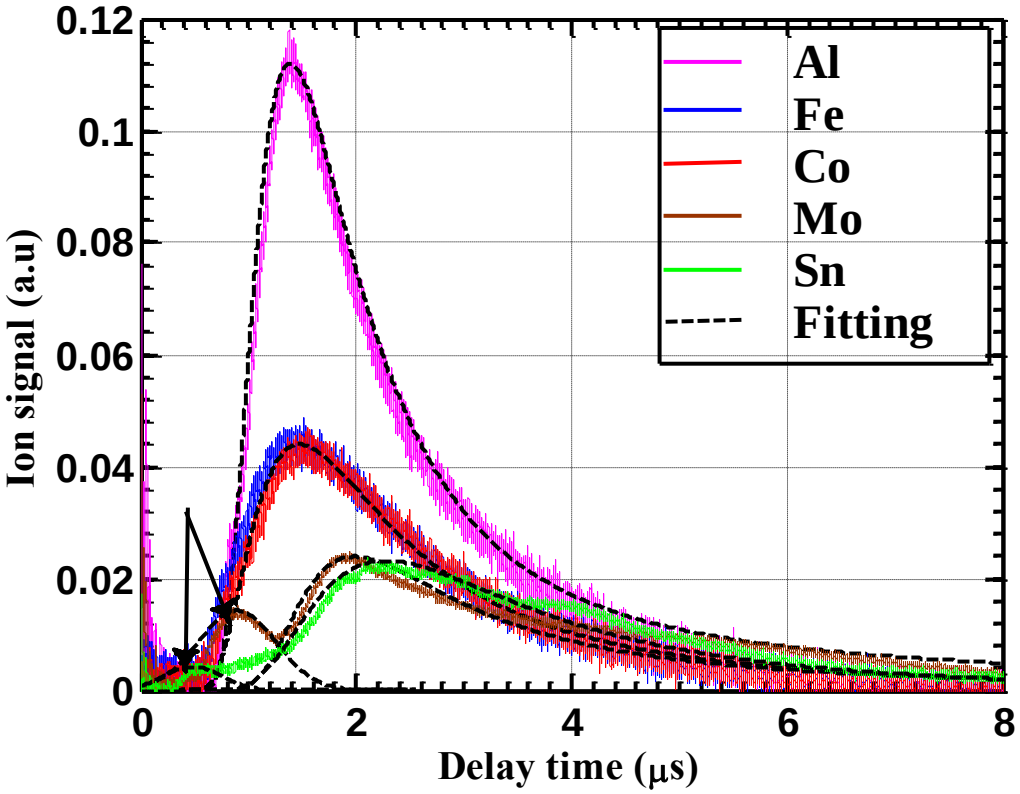

Figure 4.2 Ions' Time-of-Flight for different targets

From the TOF measurements, the dependence of the ion flux and ion velocity on the target material can be extracted. Figure 4.3 shows that the ion flux drops drastically with increasing the target's atomic weight to reach 40% of its maximum value (Al ion flux) for Co and Fe. The flux attenuation continues to decrease at the heaviest studied element (Ta). The slow ion flux was found to be correlated to material's melting temperature and heat of sublimation [61].

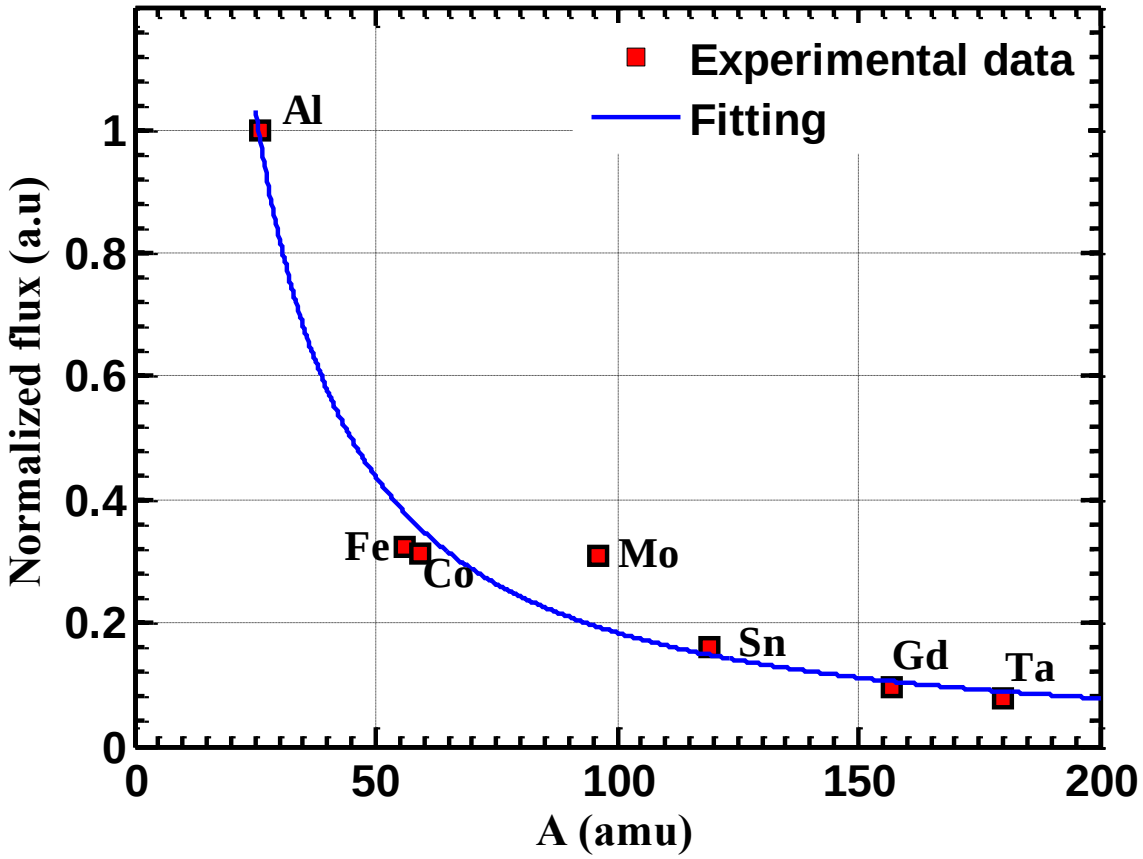

Figure 4.3. Ejected ion flux as a function of the target's atomic weight

Figure 4.4 indicates the dependence of the ion velocity on the target's atomic weight. Linear fitting of *log (V)* versus *log (A)* shows that the velocity is scaled as $A^{(-0.45\pm0.10)}$. This is in good agreement with the expected inverse square root dependence on the mass ($A^{-0.5}$) from the energy balance.

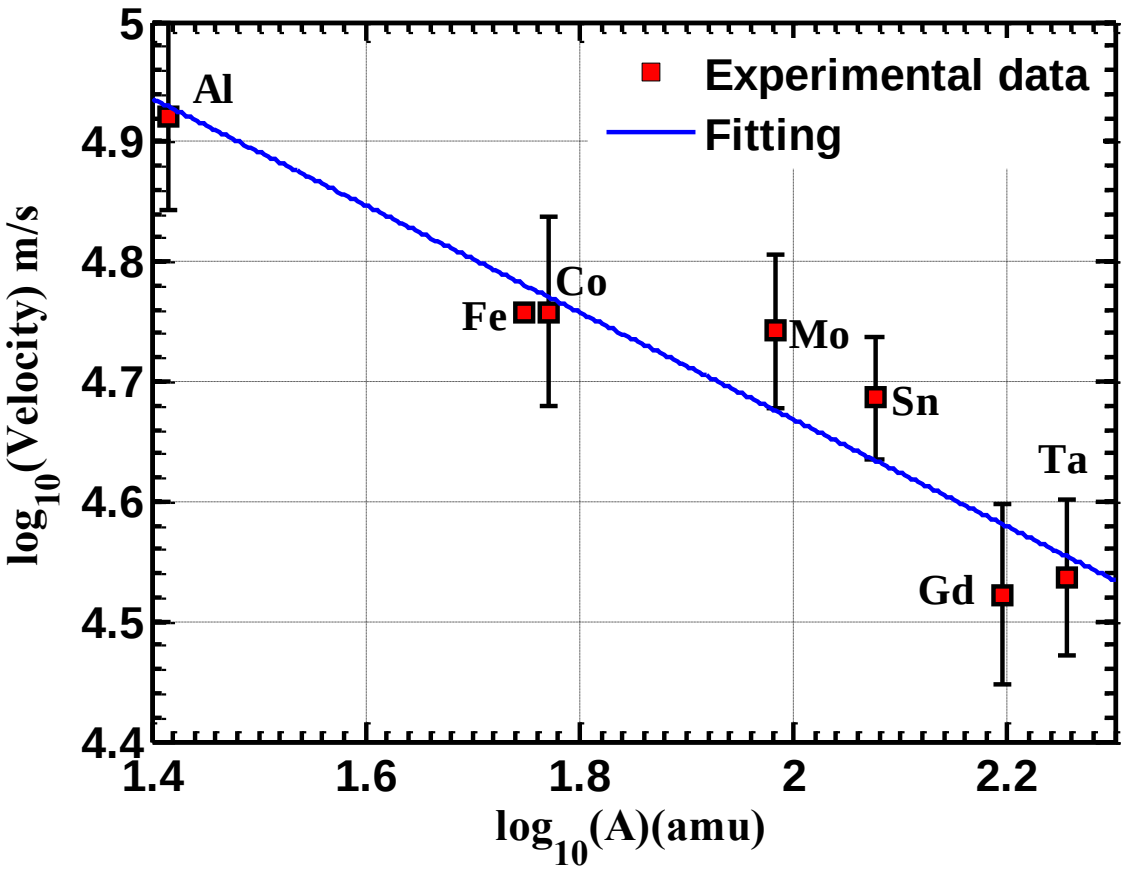

Figure 4.4. Ejected ion velocity as a function of the target's atomic weight

4.1.3 Effect of Laser Intensity on Nanosecond Laser-Produced Ion Flux and Ion Velocity

Mo target was used to investigate the effect of incident laser intensity on both the flux and the velocity of the ejected ions. A slight enhancement in the ejected ion flux was observed with increasing the laser intensity by one order of magnitude from 1.0×10^{10} W/cm^2 to 1.0×10^{11} W/cm^2, as shown in Figure 4.5. The slow ion flux tends to increase quadratically in contrast to fast ion flux, which exhibits a linear increase with incident laser intensity, as shown in Figure 4.6. From Figure 4.5 and Figure 4.6, it can be inferred that the effect of incident laser intensity on slow ion flux is more significant than its effect on fast ions.

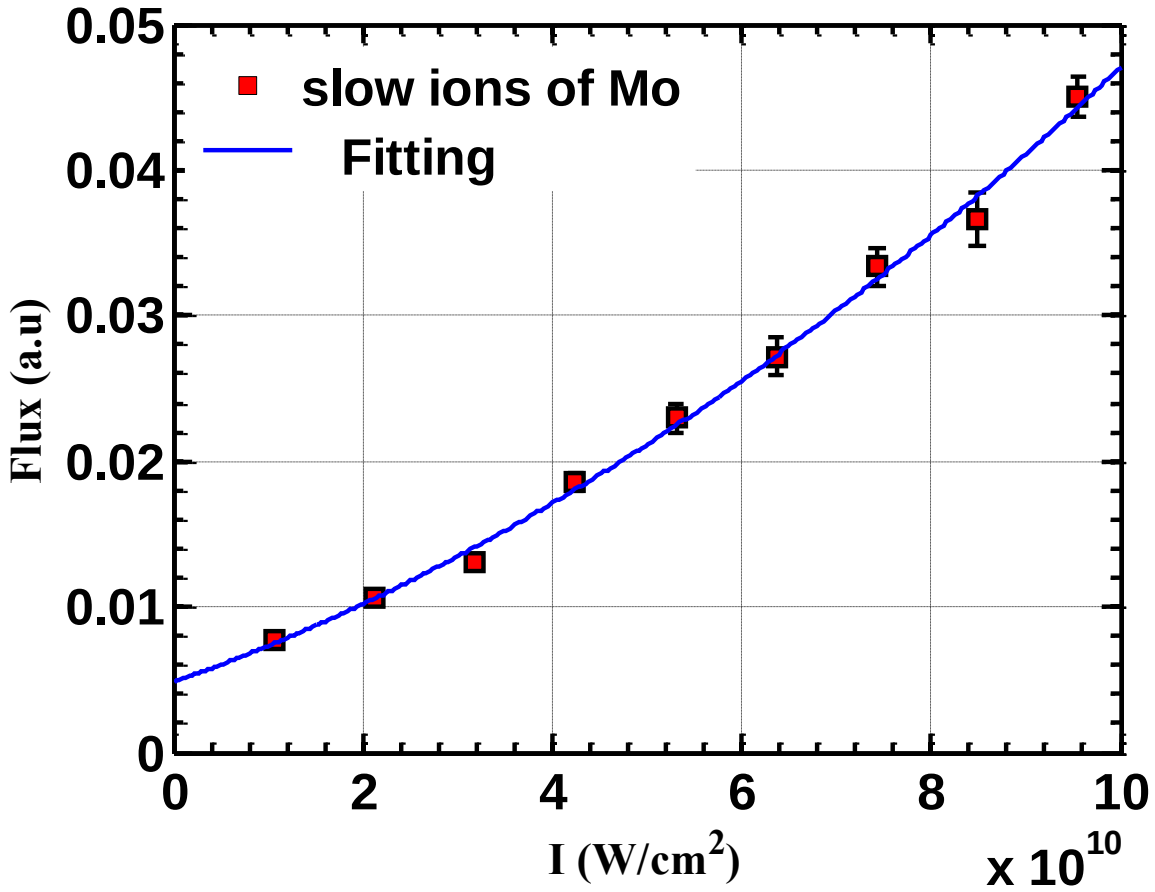

Figure 4.5 The effect of the incident laser intensity on slow ion flux

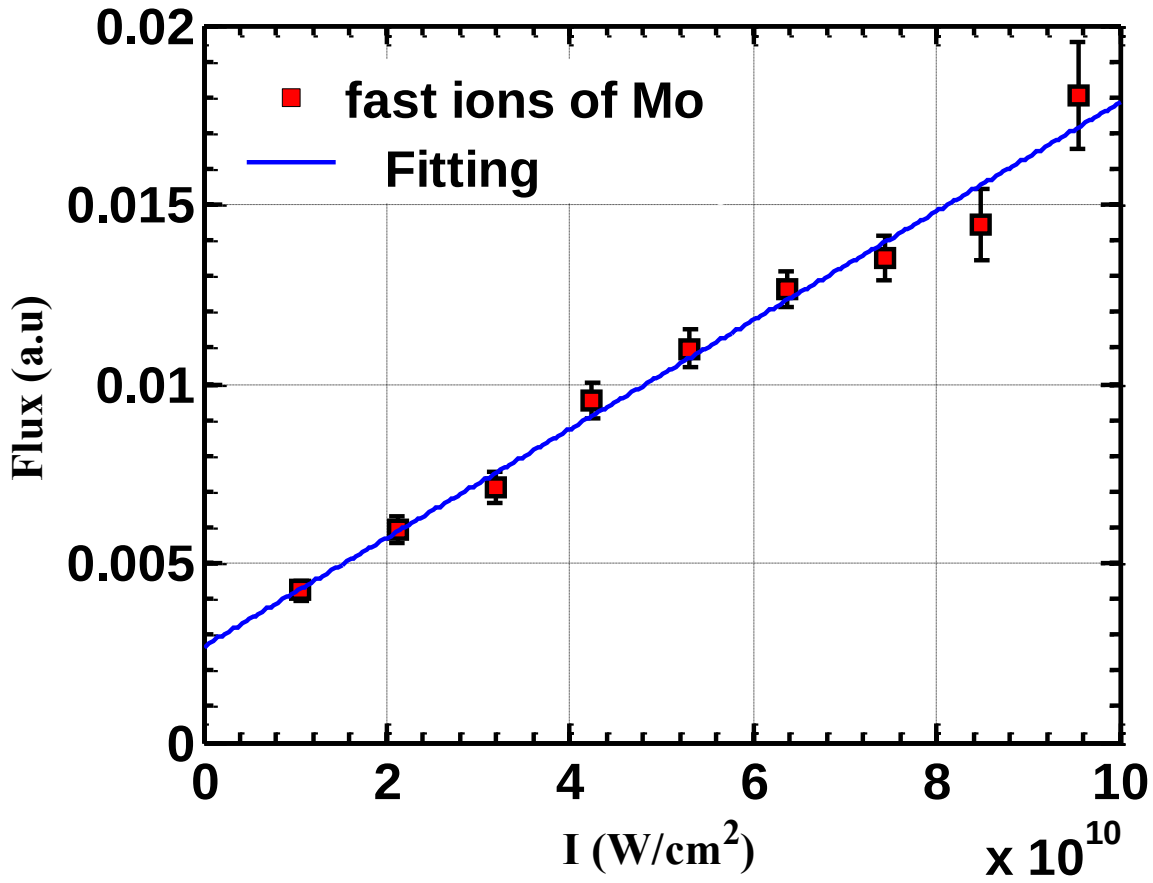

Figure 4.6 The effect of the incident laser intensity on fast ion flux

Similarly, the enhancement of slow ions' velocity was found to be more pronounced than in the case of fast ions, this is evident from Figure 4.7 and Figure 4.8. Furthermore, fast ion velocity was found to be one order of magnitude higher than what was observed for slow ions.

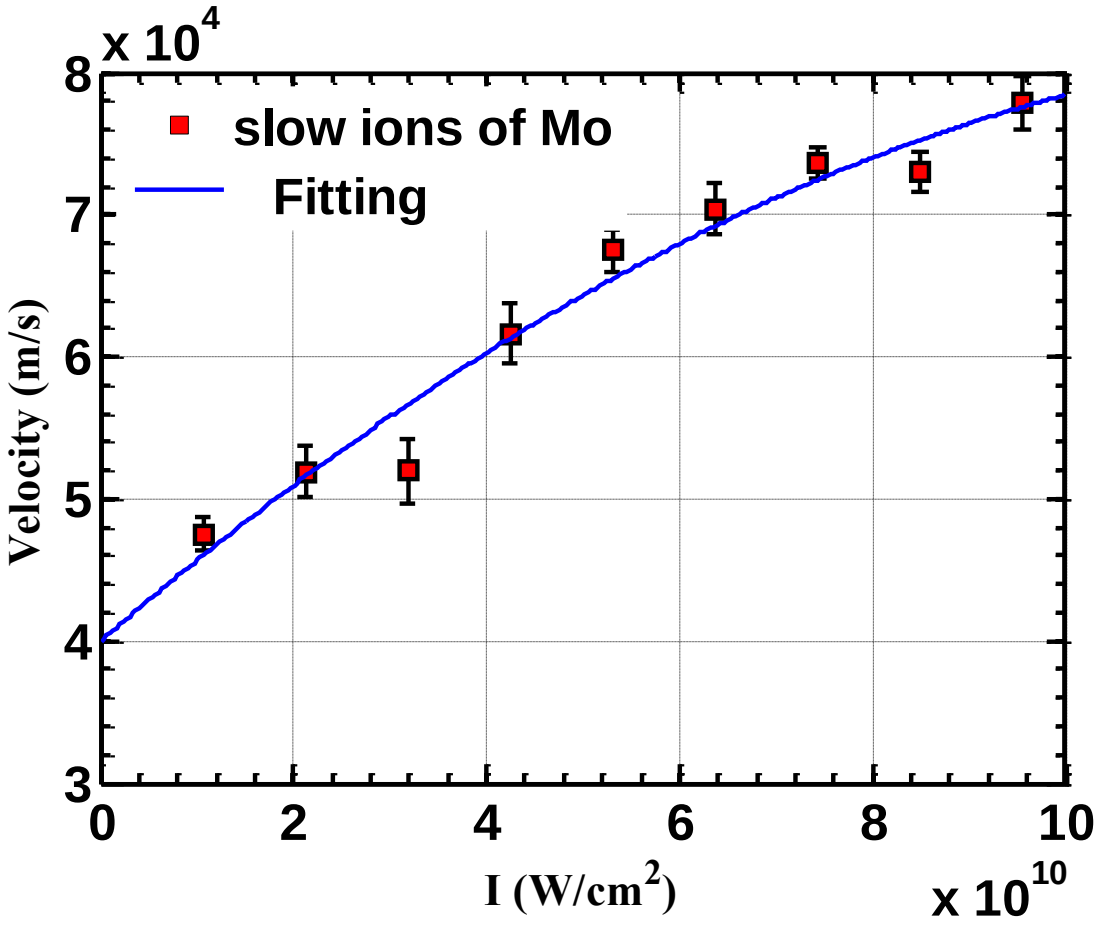

Figure 4.7 Effect of the incident laser intensity on slow ion velocity

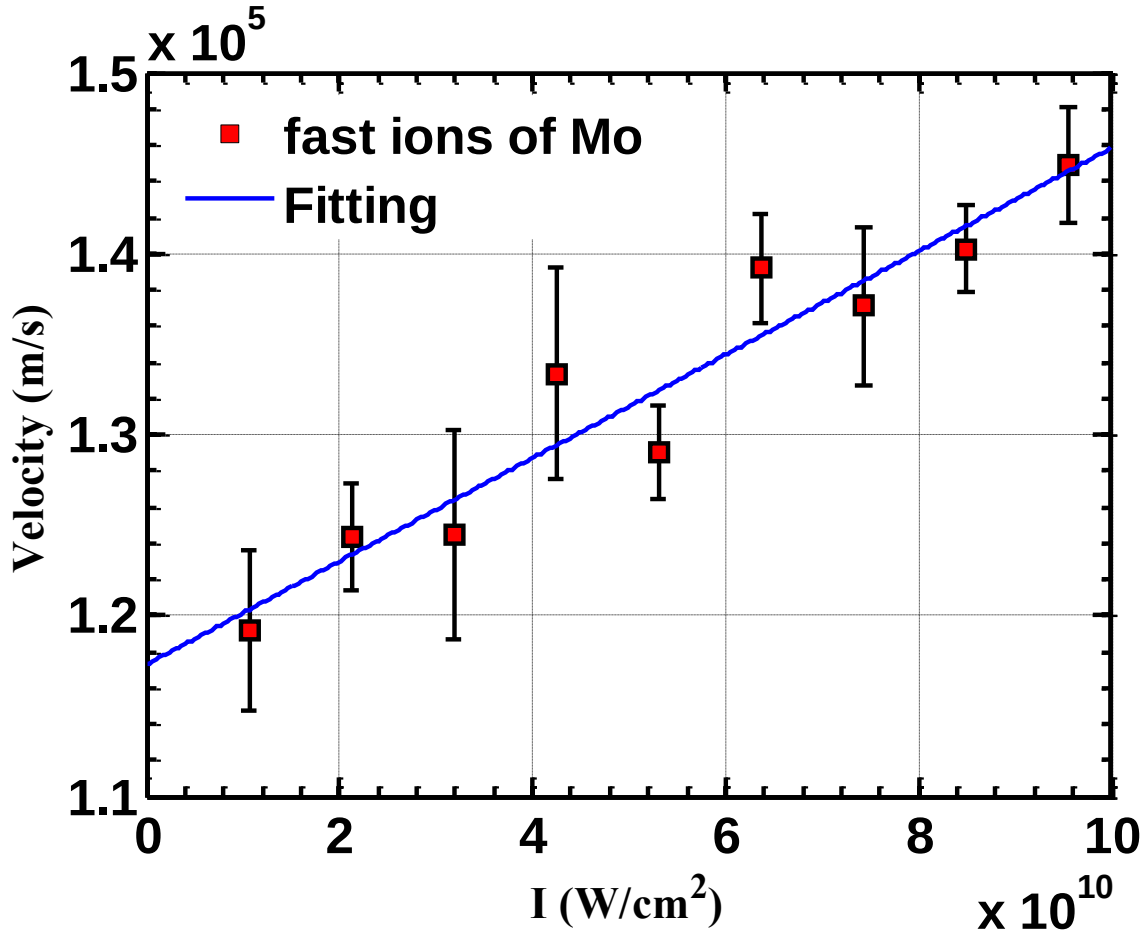

Figure 4.8 The effect of the incident laser fluence on the fast ion velocity

4.1.4 Angular Distribution of Nanosecond Laser-Produced Ion Flux and Ion Kinetic Energy

The dynamics of the propagation of ejected particles are of special interest for many applications, including, but not limited to, pulsed laser deposition (PLD), ion implantation, and fundamental physics. Figure 4.9 shows that slow ions flux for both Mo and Al peaks at an angle normal to the target surface. The results for both high-z and low-z materials reveal that the spatial distribution of slow ions is independent of the type of material. A model discussed in section 3.2.2 was used to fit the experimental data, (solid lines in Figure 4.9). Fitting parameters provides valuable information about the geometry of the ejected plume through the expansion ratio, β. The value of β was found to be 1.90±0.15 for Mo and 2.1±0.20 for Al. The expansion ratio illustrates that the plasma plume expands elliptically independent of the target atomic weight. On contrary, the spatial

distribution of fast ions was found to be significantly different as shown in Figure 4.10. The ion flux peaks at a 40º angle, and it has a dissimilar trend to slow ions. A previous experiment by N. Farid et al. 2013 conducted on Mo target, using Nd:YAG laser providing 1064 nm, 180 mJ focused down to 400 μm diameter falling normal to the target surface, found that the there is a fast ion peak at a 30º angle as shown in Figure 4.10. This result is in agreement with the work presented here. However, further work is still needed to explain why there is a fast ion flux peak at a larger angle.

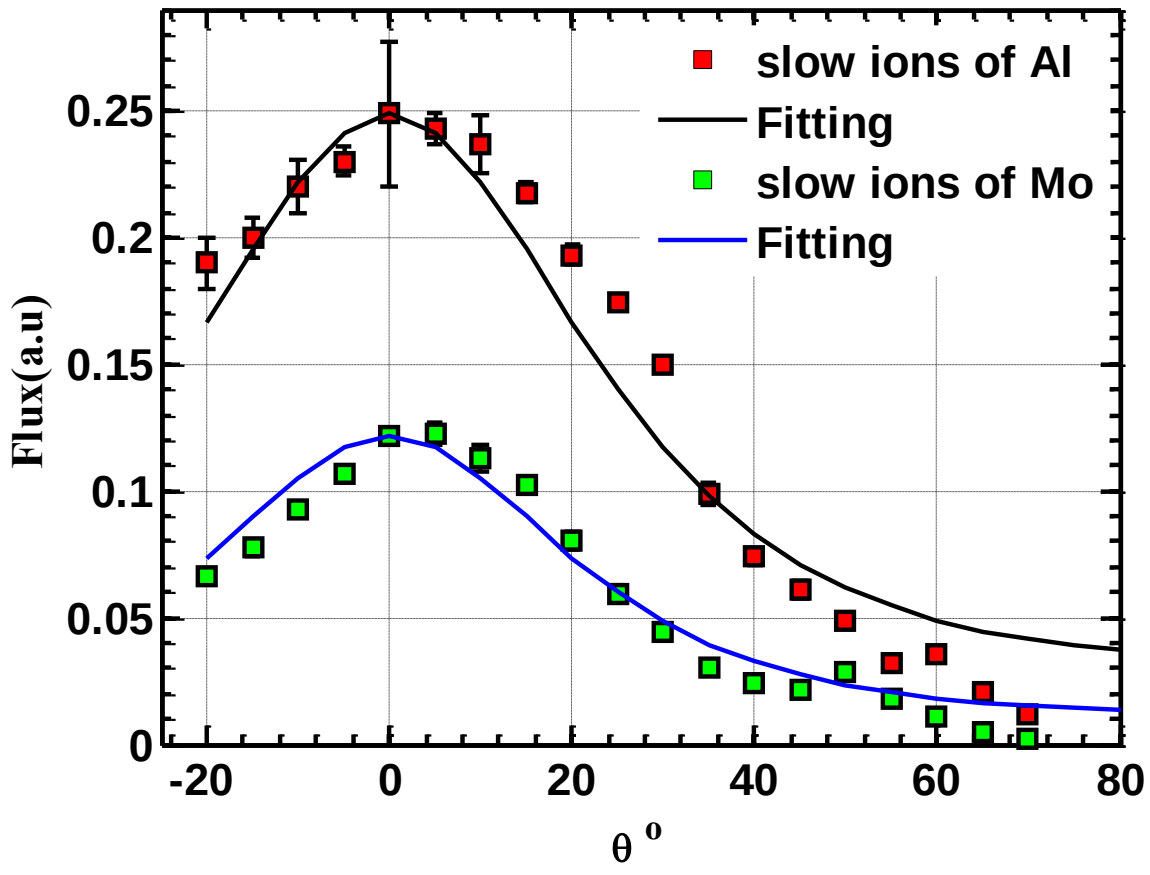

Figure 4.9 Spatial distribution of slow ion flux

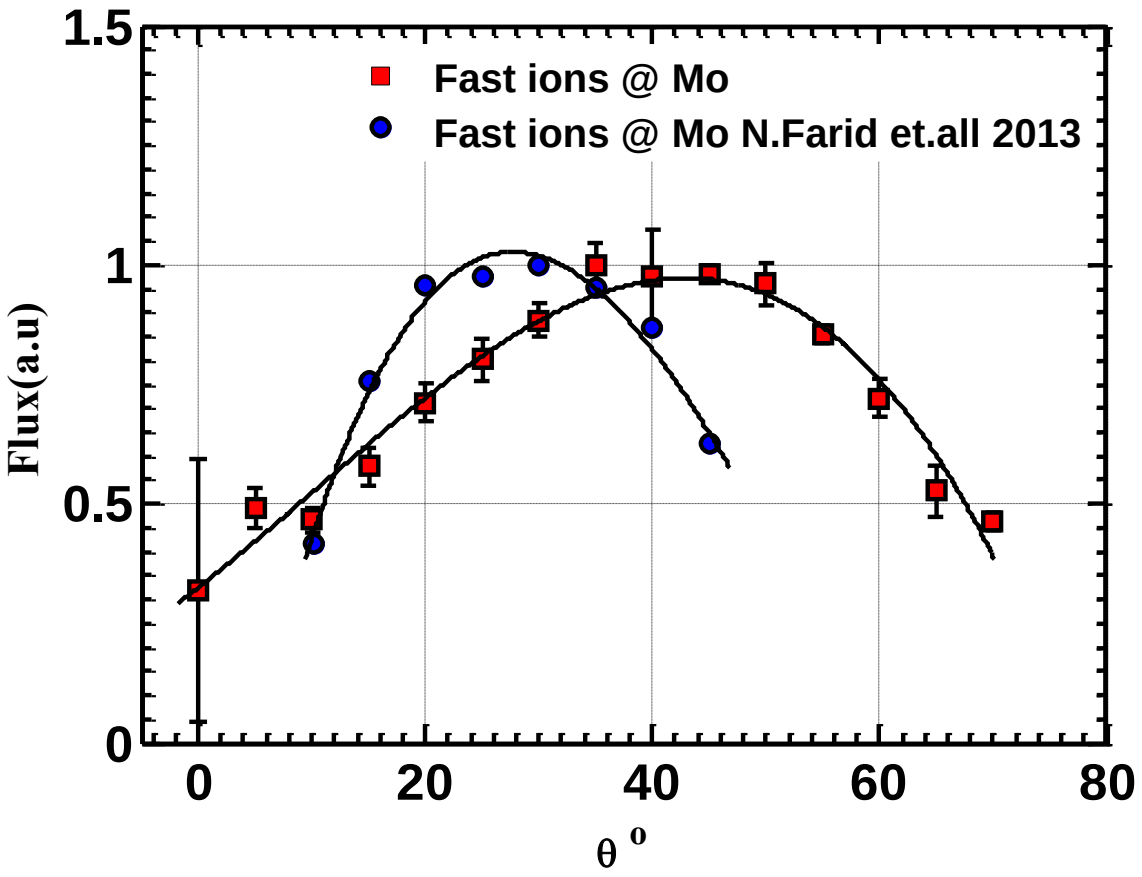

Figure 4.10. Spatial distribution of fast ion flux

In summary, the effect of nanosecond laser on low-Z and high-Z laser-produced ions was investigated. Results show that the tendency of both ion flux and velocity to decrease with increasing target's atomic weight for the same laser intensity and tendency to increase with increasing incident laser intensity. Ion flux was found to correlate to target atomic weight. Heavy metals TOF exhibited multiple peak structures while this was absent in light metals. Previous studies [62,63] were conducted to study the properties of laser-produced electrons showed that an ejection of high-energy, prompt electrons from heavy metals with temporal distribution coincide with the incident laser pulse along with thermal electrons with a wide temporal distribution in the order of microseconds. Furthermore, an extensive work has been done recently on the dynamics of prompt electrons, ions, and neutral particles [64], the electrons were ejected from the tungsten target via irradiating it with 8 ns pulse duration laser. The existence of a strong emission from ambient gas at an early time (~5 ns), which preceded the emission from the tungsten (the target),

was evidence for the existence of prompt electrons. Furthermore, these electrons were found to have a temporal profile that follows the temporal profile of the incident laser. Furthermore, temporal distribution for slow ions was found to follow shifted Maxwell Boltzmann (SMB) distribution, while fast ions followed Gaussian distribution. Moreover, the angular distribution for slow metal ion was observed to maximize at 0^{o} angle independent on the target atomic weight, while fast ions peak at large angles ~40^{o}. Conclusively, this difference in both spatial and temporal ion distribution, along with the fact that heavy metals ablation shows evidence to the ejection of prompt electrons [62,63], is an evidence of the different ion ejection mechanisms during nanosecond laser-material interaction, and the prompt electrons are responsible for emission and acceleration of fast ions. However, more studies are still required to investigate why fast ions tend to peak at larger angles. Angular flux distribution was used to measure the ablated plume asymptotic expansion ratio for both heavy metal (Mo) and light metal (Al). This ratio revealed that the shape of the ejected plasma plume is elliptic.

CHAPTER 5. LASER-PRODUCED PLASMA

5.1 Background

Electron plasma density and temperature are two fundamental parameters for plasma characterization. The optical emission spectroscopy technique is a well-established method to measure both electron plasma density and temperature, so it was proven to be a powerful and flexible diagnostic mechanism for both quantitative and qualitative analysis [65–67]. Attention has been devoted to Sn laser-induced plasma, mainly semiconductor lithography industrial applications, as Sn is currently the leading candidate material for EUV light sources for microchips with features size less than 32 nm. So, the current work is extended to study nanosecond and ultrashort laser-induced Sn plasma in time and space by investigating the spatial and temporal evolution of plasma density and electron temperature as the key parameters of laser-ablated plume [57]. The profile of the spectral lines is affected directly by the plasma density; the denser the plasma, the wider the spectral line. Multiple mechanisms contribute to widening the spectral line's profile. These broadening mechanisms include Doppler, Start, and natural effect [65]. The line profile is dependent on the dominant broadening mechanism, the Doppler broadening effect, resulting in the Gaussian profile, while stark as well as natural broadening effects result in a systematic Lorentz profile [65]. Stark effect is mainly due to collisions with electrons, with minor contribution due to collisions with ions [65]. And Doppler broadening is due to different Doppler shifts given by $\Delta\lambda = \lambda v_z/c$ (where λ is the wavelength), experienced by the ablated particles having different velocity components v_z in the detection direction [68]. Under normal conditions in LIBS, natural broadening can be neglected, and a velocity range of ~10^4 m/s, the FWHM of Doppler line width for Sn-I 317.505 nm, is in the range of ~ 0.1A, which can be also neglected. Consequently, the dominant broadening effect that determines the plasma density becomes the Stark effect [65]. FWHM line broadening resulted from stark effect is given by $\Delta\lambda_{1/2} \sim n_e \times \omega_{1/2}/10^{16}$, where $\Delta\lambda_{1/2}$ is half-width at half maximum, n_e is electron plasma density in cm^{-3}, $\omega_{1/2}$ [69] is half-width at half maximum measured at 10^{16} cm^{-3}. Electron plasma temperature, *Te*, on the other hand, was measured using optical emission spectroscopy by Boltzmann plot method, formula and further details can be found in ref. [65].

5.2 Experimental Setup

Ti:Sapphire (CPA) laser was used to irradiate 99.99% Sn target. This laser system generates 800 nm, 40 fs (FWHM), P-polarized laser pulses. Such a system provides a tunable laser power ranges from tens of gigawatts up to several terawatts. When using such a high laser power, the laser pre-pulse/contrast ratio has to be considered. For this purpose, the noise around the main pulse was measured in the delay range of about -500 ps to 180 ps and the picosecond contrast ratio was found to be $1x10^{-8}$. The parasitic pulses arriving at greater than 1 ns delay around the main pulse were also measured, and the nanosecond contrast ratio was found to be $1x10^{-7}$. Consequently, the effects of both post- and pre-pulses, either pico- or nano-second, can be ignored and the output laser can be assumed to be pure femtosecond laser. A set of half waveplate and thin film polarizer positioned before the compressor enabled tuning the output laser energy. As shown in Figure 5.1, the laser was focused onto the target surface with a 45^{o} incidence angle via a 40 cm plano-convex lens that yields an elliptical spot with a size of $1.5x10^{-5}$ cm^2. The targets were placed on a remotely controlled XY translation stage to have a fresh surface and kept under vacuum (10^{-6} Torr). Time-resolved plasma emission was measured using a 0.5 mm triple grating (1800, 600, and 150 lines/mm) spectrograph coupled to ICCD, which collected the dispersed spectral features of the laser-induced plasma. The emission light was focused on the spectrograph inlet using two 40 cm lenses outside the chamber, while the emitted light passed through a quartz window; all were mounted perpendicular to the plume expansion direction. The last lens was mounted on a translation stage to allow space-resolved measurements. A 50 ns gate width and 600 lines/nm grating were light emission spectroscopy measurements. A programmable time generator was used to control the delay time between the laser pulse and the emission light detection system.

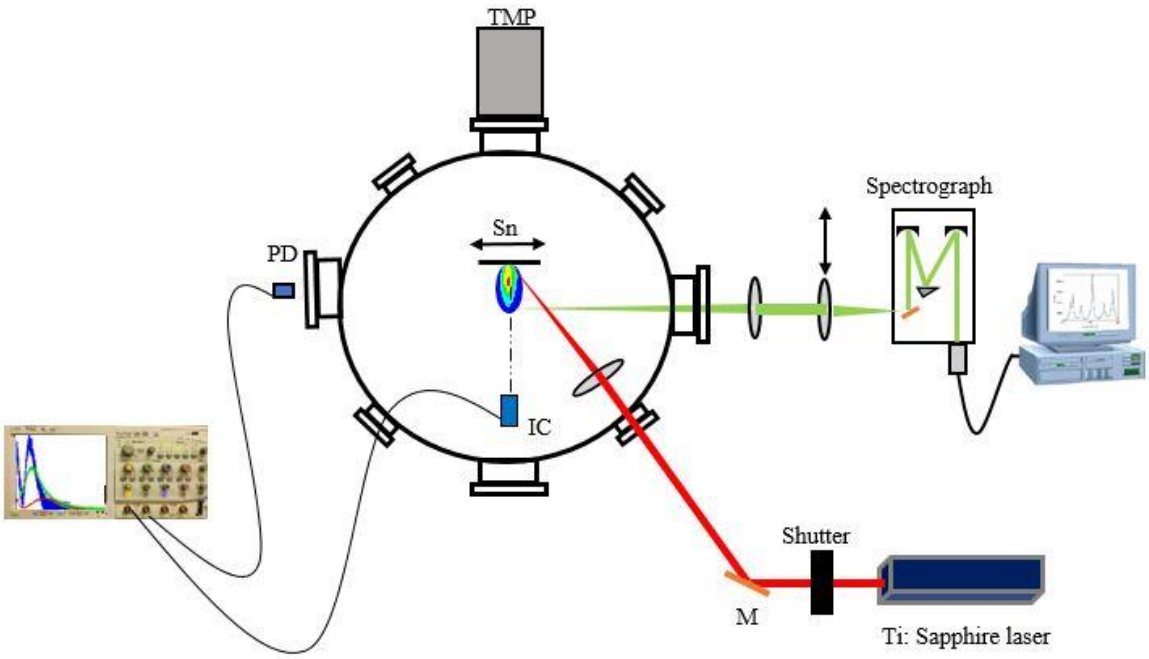

Figure 5.1. A schematic of the experimental setup

5.3 Ultrashort Laser Produced Plasma

Figure 5.2 shows the evolution of the Sn plasma density as a function of time, measured at 0.5 mm away from the target surface and induced by 5.8 x10^{15} W/cm^2 laser fluence. Three different regions can be observed in Figure 5.2. At the early time, the electron plasma density has a maximum density in the order of 4.5x10^{17} cm^{-3}. This is followed by another region in which the electron plasma density decreases gradually with time to reach a minimum density of 2.5x$10^{17}$$cm^{-3}$ after 120 ns, almost half of its maximum value. The third region is found after 120 ns in which the plasma density remains almost constant. In this region, the line emission spectrum is relatively weak, and the background light is relatively high.

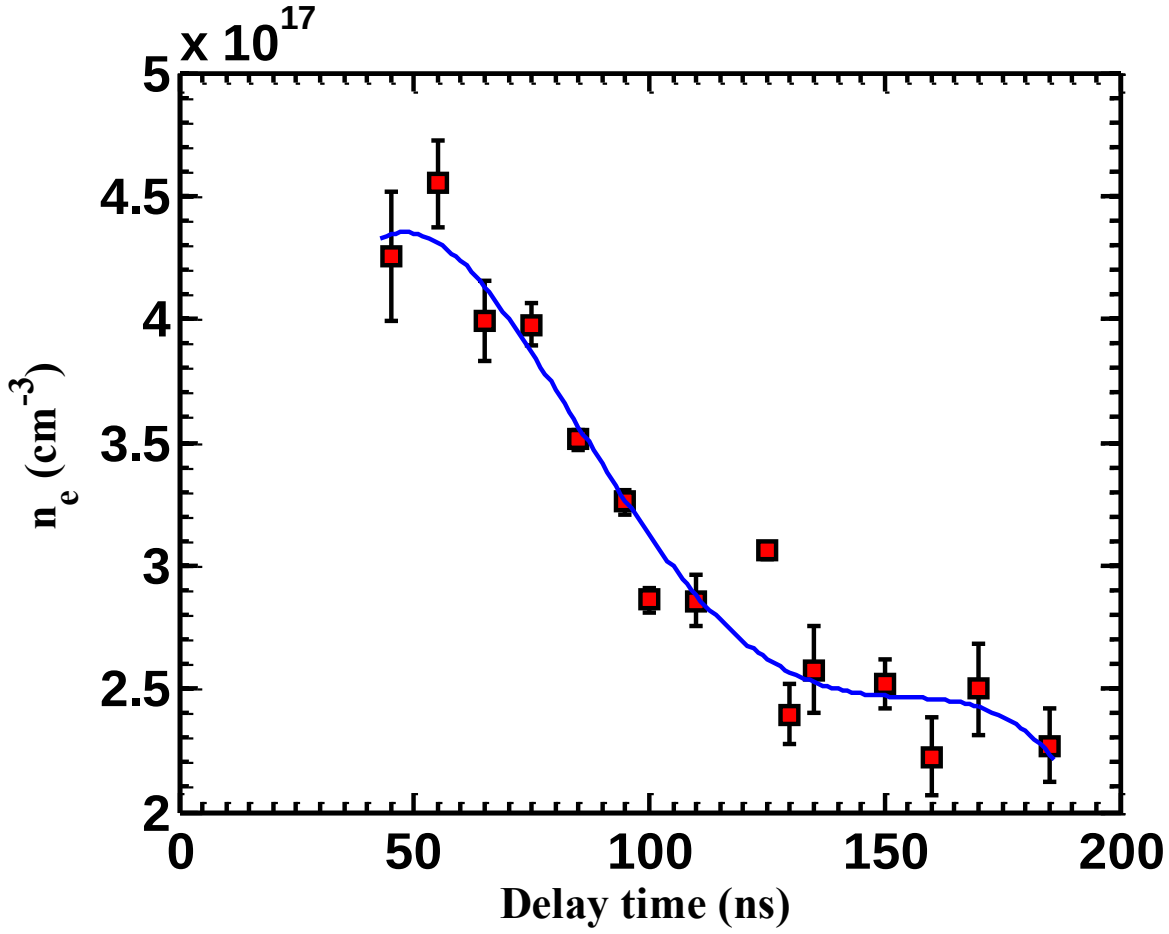

Figure 5.2. Temporal evolution of electron plasma density

Figure 5.3 shows that at an early time, the electron plasma temperature is 1.57×10^4 K corresponding to 1.4 eV. Hereafter, the temperature decreases slowly with time to reach 1.27×10^4 K or ~ 1.0 eV at a later time. As mentioned above the emission spectrum is characterized by weak line intensities and high background at a larger time delay. The plasma can be thought of like a hot gas under high pressure. Once this gas is initiated in a medium it experiences sudden expansion. Therefore, at early times, the electron plasma density, as well as the electron temperature, are relatively higher. and at a later time, two factors start to play a role in cooling down the plasma. These factors are; plasma adiabatic expansion and electron-ion recombination. A slow decreasing rate, as shown in Figure 5.2 and Figure 5.3, suggests a favored expansion direction, likely to be the forward direction as it was studied in chapter 3 by measuring the forward peaking factor β that was instructed from measuring the ion flux angular distribution [70].

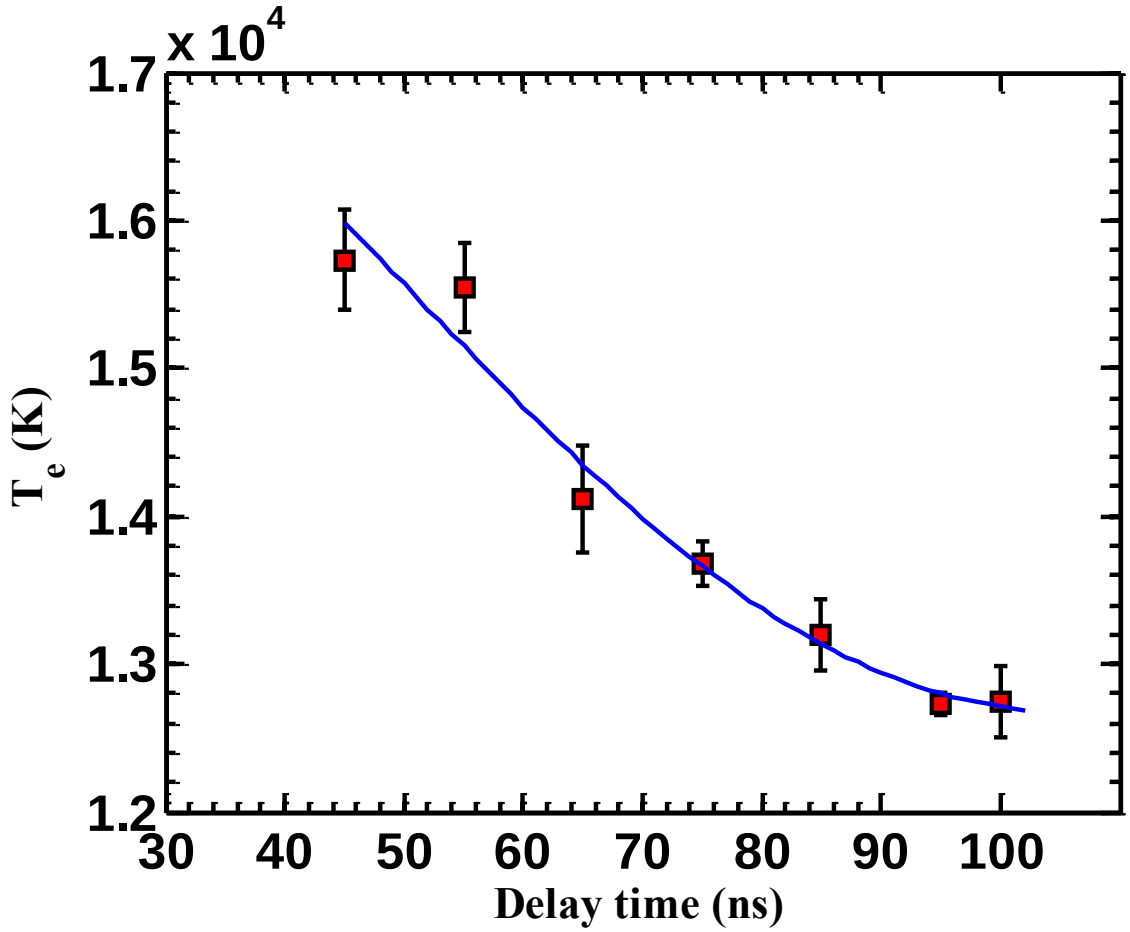

Figure 5.3. Time evolution of electron plasma temperature

5.4 Nanosecond Laser Produced Plasma

The femtosecond laser system used in the experimental setup in section 4.2 was replaced by Nd:YAG laser system, which generates 1064 nm, 6 ns P-polarized nanosecond laser pulses. The experimental setup is shown in Figure 5.1, the laser spot size is measured on the sample surface to be 200 μm in diameter. This experimental setup was used once again to investigate the fundamentals of laser-produced plasma when using longer pulse duration. The same target was used (Sn) in order to rule out the effect of material properties on the physics of produced plasma. And the data were acquired and averaged over 100 ns gate width. Figure 5.4 and Figure 5.5 show that the plasma density and plasma temperature reach their maximum values at an early time and then decrease due to the effect of plume expansion. A maximum plasma density of 6.6×10^{17} cm^{-3}

and 1.2 eV electron plasma temperature were measured at an early time and 3.5 mm away from the target surface. It bears mention here that the gate width used in this measurement is 100 ns. At an early time of the plasma within the laser pulse duration, the plasma tends to expand isothermally. After the termination of the laser pulse, when laser energy is no longer pumped into the plasma, the adiabatic expansion will take over. Consequently, the plasma density drops almost linearly with time to reach 90% of its maximum value after 800 nanoseconds. As shown, the drop in the plasma density during the 800 ns is not severe. On the contrary, the plasma temperature attenuates dramatically in the first 150 nanoseconds to reach a value of 0.6 eV ~50% of its initial value and decrease slowly after that.

The lifetime of the plasma was found to be the main difference between femtosecond and nanosecond laser-produced plasma. The lifetime of nanosecond laser-produced plasma is almost is in the range of 800 ns while femtosecond laser-produced plasma is 200 ns. This difference is attributed to the difference in the pulse duration of the incident laser. The relaxation time between the free electrons (freed by incident laser), and the lattice atoms are in the order of picoseconds. This means that after picoseconds from laser irradiation, the plasma starts to expand and propagate in the surrounding medium. A pulse duration longer than picoseconds has a definite chance to interact with the plasma plume. This ultimately happens when using a nanosecond laser pulse to produce plasma while it ultimately has no chance to occur when using a femtosecond laser pulse to produce plasma. The long pulse duration tends to deposit extra energy to the propagating plume. This, in turn, compensates for the decay of plasma due to the isothermal expansion effect. However, the plasma density and temperature ware found to be in the same order of magnitude.

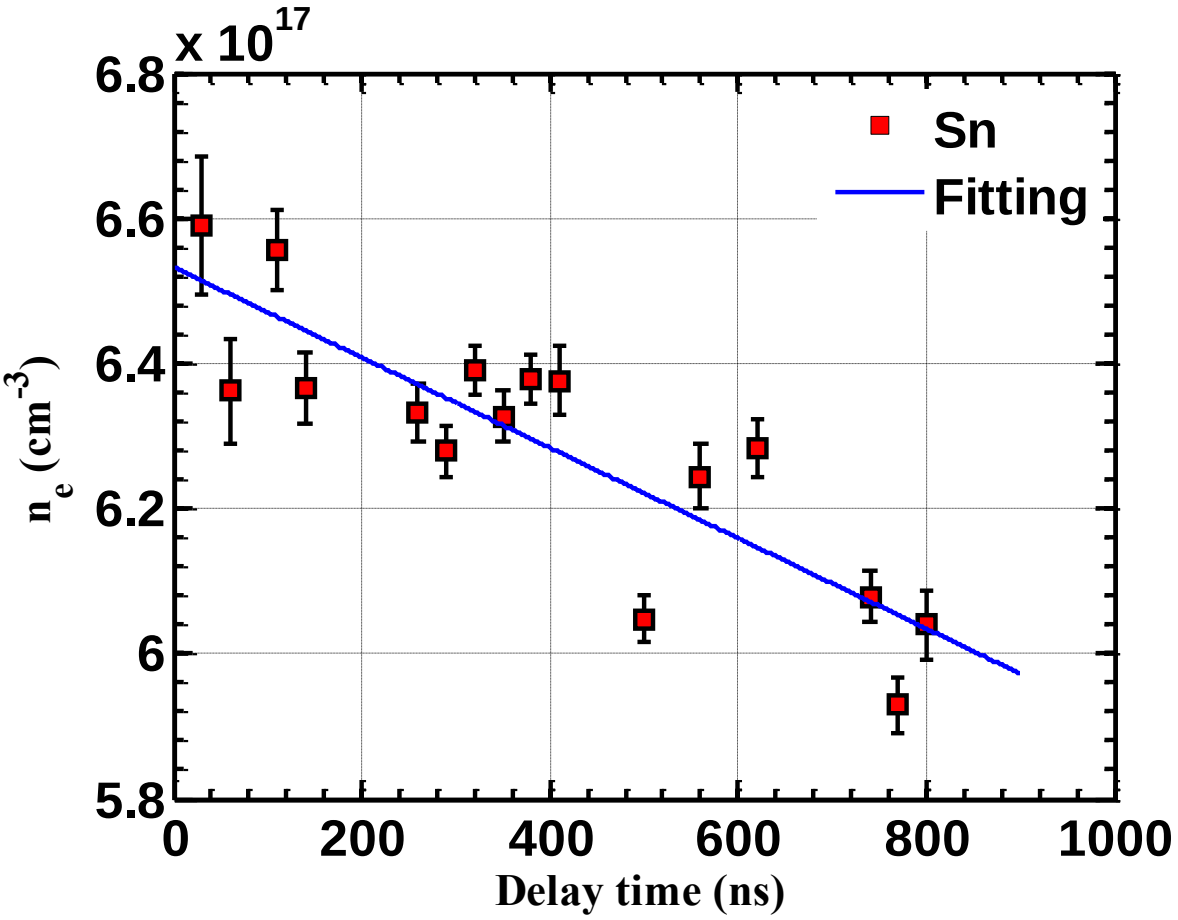

Figure 5.4. Time evolution of electron plasma density

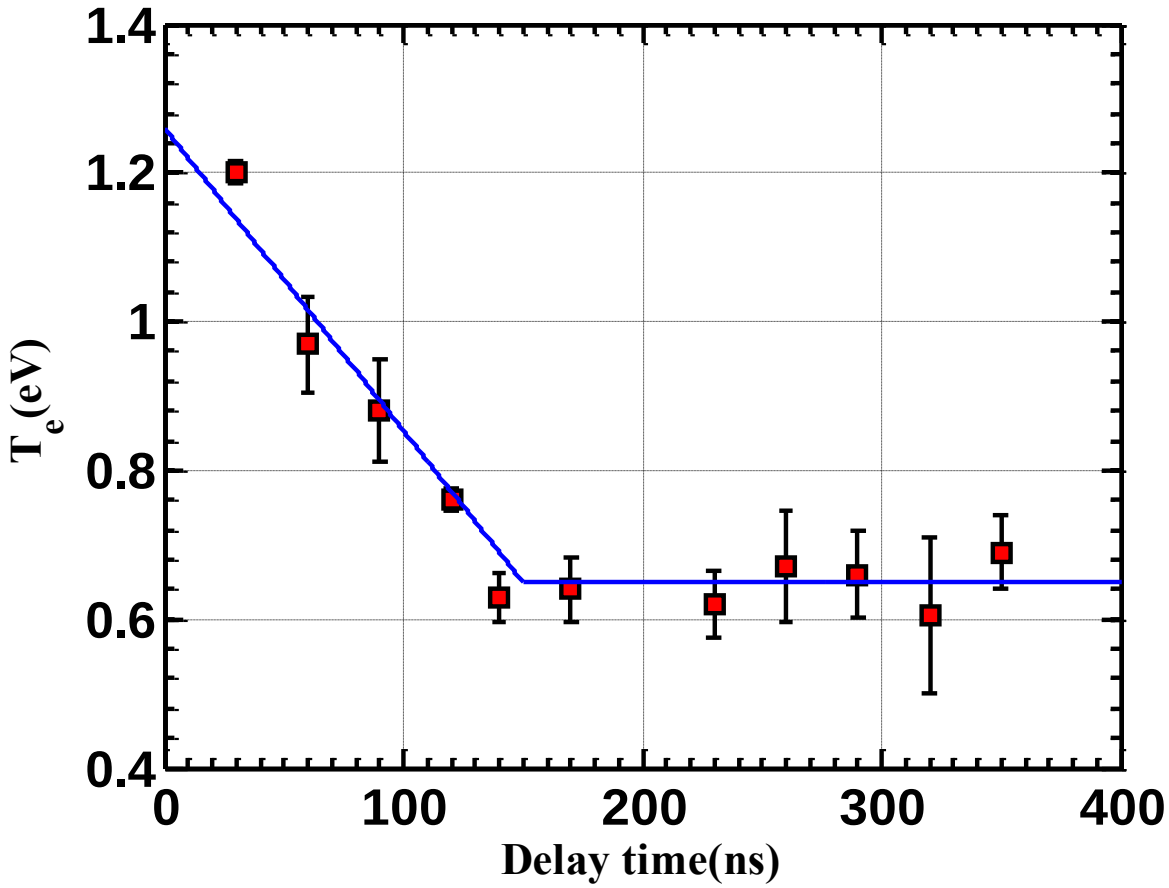

Figure 5.5. Time evolution of electron plasma temperature

The spatial evolution of electron plasma density and temperature were measured after 180 nanoseconds from the laser pulse, as shown in Figure 5.6 and Figure 5.7. Both plasma density and temperature increase close to the surface ~0.5 mm away from the target surface. Then the temperature and density decay due to plume expansion. A maximum plasma temperature was measured to be 1.3 eV, 0.5 mm away from the surface, while at 4 mm away from the target surface the temperature was found to be 0.4 eV. A similar observation was also noticed on the behavior of plasma density, 8.0×10^{17} cm^{-3} maximum density was observed at ~0.5 mm after 180 nanoseconds, followed by a rapid decrease, to a minimum value of 5.0×10^{17} cm^{-3}, 4 mm away from the target surface.

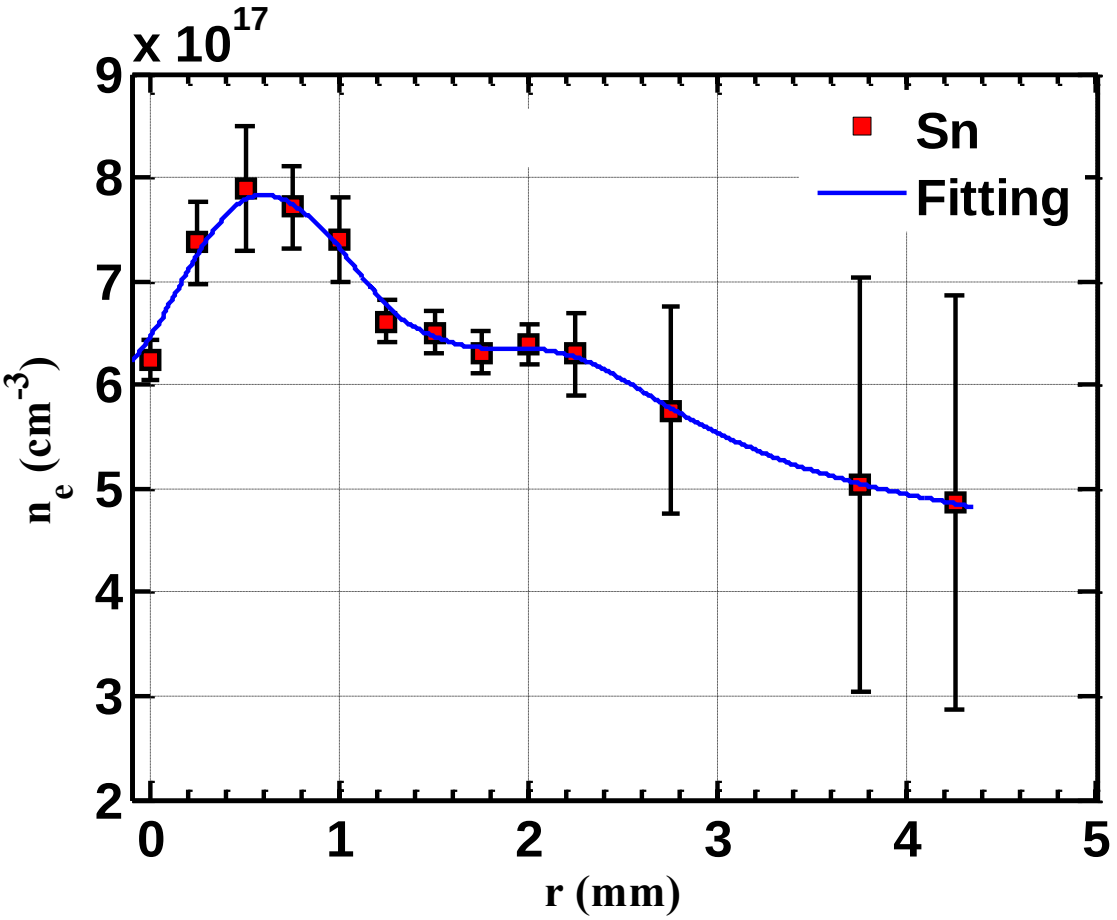

Figure 5.6. Spatial evolution of electron plasma density

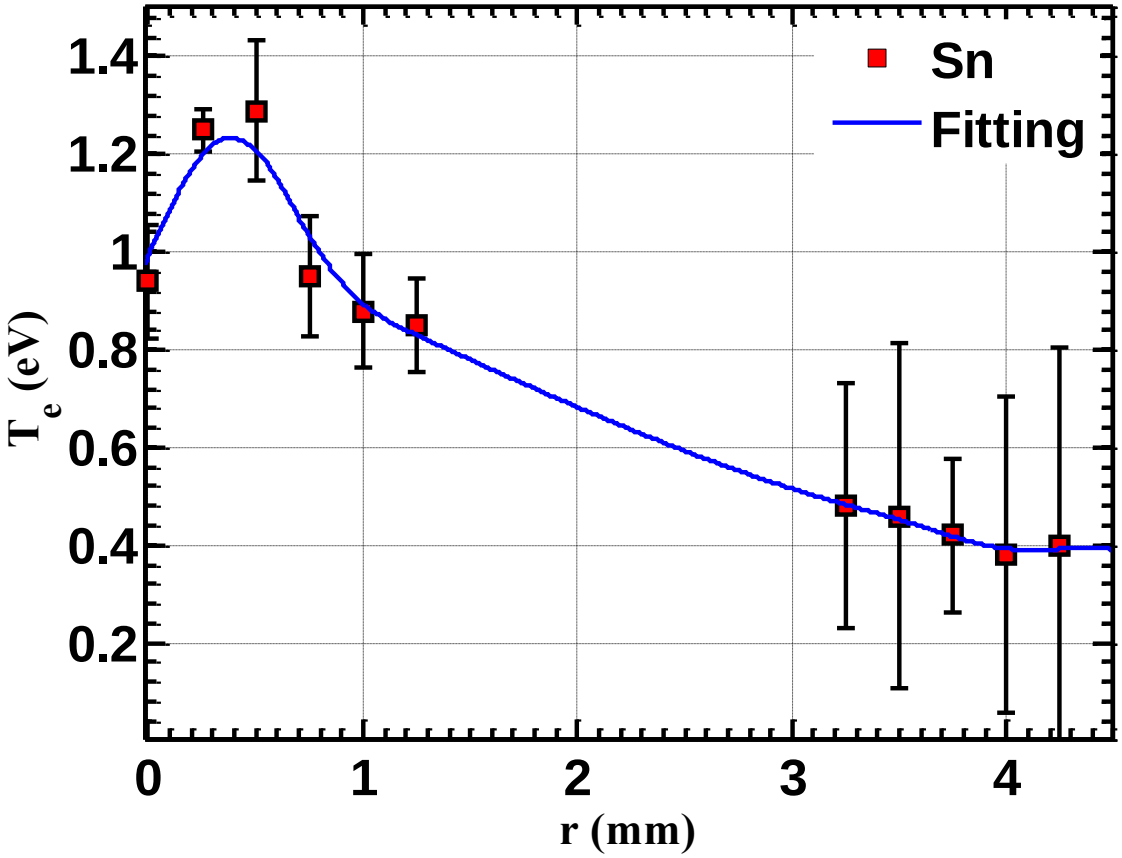

Figure 5.7. Spatial evolution of electron plasma temperature

CHAPTER 6. ABLATION OF METALS AT DIFFERENT AMBIENT CONDITIONS

6.1 Background

Ablation of metals under different ambient conditions became an interesting topic for many applications such as a plasma-facing component in magnetic and inertial fusion reactors [71] especially at high laser fluence, laser micromachining and metallic etching [72], pulsed laser deposition [6], fundamental physics, and so on. To model this process is costly and complicated as it involves multiple phenomena such as melting, vaporization, changing in material properties, and so forth, all are interconnected and occur simultaneously. In this work, the effect of laser fluence, ambient gas, and ambient pressure were studied on material ablation induced by nanosecond laser irradiation. Aluminum target material was used for this study. Nanosecond laser radiation as a condensed source of energy provides a powerful tool to study the ablation resistivity of such material.

6.2 Experimental Setup

A 1 mm, 99.99% aluminum targets were exposed to extreme irradiation conditions using 6 ns, 1064 nm, Nd:YAG laser. Such a laser system provides laser energy ranging from 2 mJ up to 800 mJ. A set of half-wave plate and a beam splitter was used to tune the laser energy. The laser beam was focused down to 375 μm diameter on the surface of the target using a 100 mm plano-convex lens. The laser is focused on the target passing through a quartz window normal to the target surface as shown in Figure 6.1. The target was mounted on an XY translation stage inside the ablation chamber. Feedthrough was connected to the chamber to allow ambient gas injection. A White Light Profilometer (WLP) was used to characterize the ablation profile. To get an idea about the thermal effect and melt occurring during the laser pulse irradiation, the melt height around the crater was measured and reported as well. The main key parameters for this experiment are laser fluence, ambient gas, and ambient pressure. Argon and air were used to study the effect of ambient gas on the laser ablation. A pressure of 10 Torr and 760 Torr were chosen to study the role of ambient gas pressure on the ablation process. For each experiment, the ablation depth, amount of

mass ablated, and height of the molten layer on the edge of the ablated spot were measured and reported as a function of incident laser fluence that varied from 2 J/cm^2 to 300 J/cm^2.

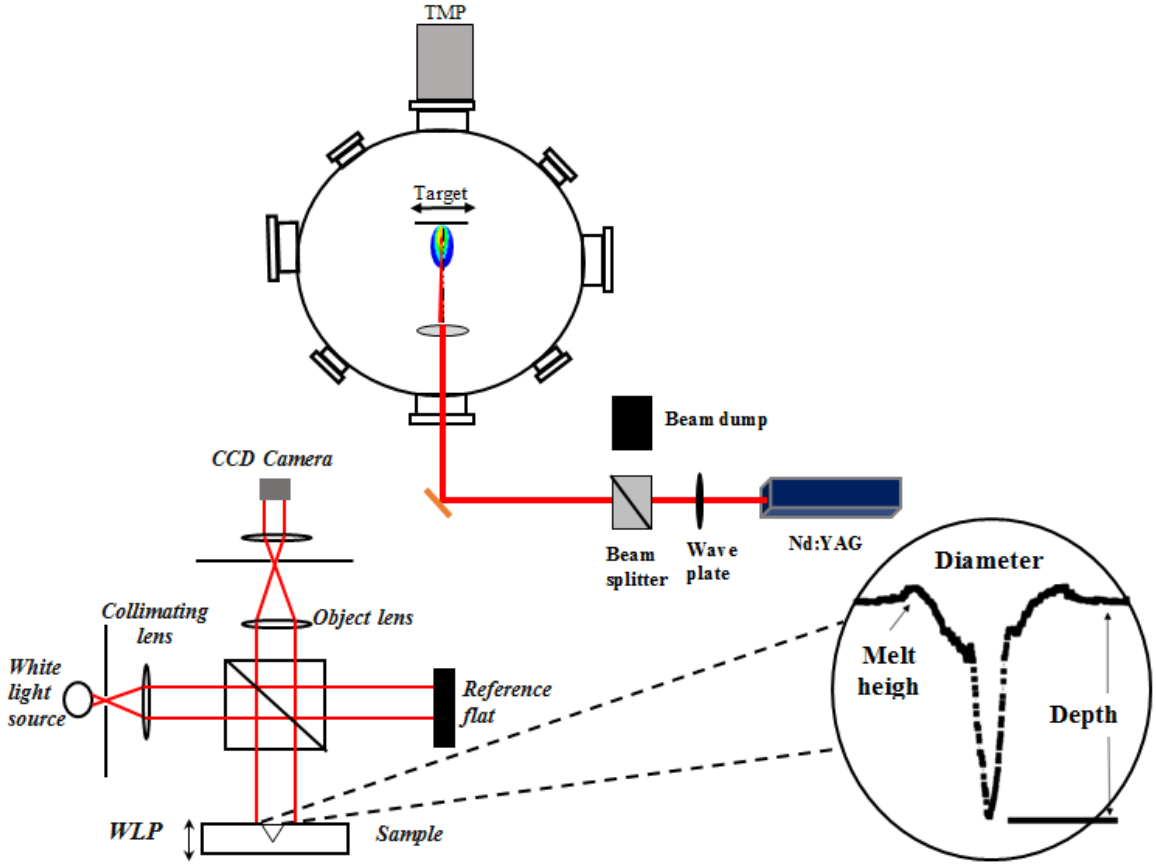

Figure 6.1. A Schematic Diagram of the experimental setup

6.3 Effect of Ambient Gas on Laser Ablation

Injecting argon and air gases, one at a time, in the ablation chamber and irradiating the target over a wide range of laser fluence, while maintaining the ambient pressure constant at 1 atm, enables studying the effect of ambient gas on laser ablation. Results presented in Figure 6.2 show that the ablation depth tends to level off at laser fluence higher than ~23 J/cm^2 for both air and argon ambient gas with a relatively smaller ablation depth obtained at argon gas. A similar trend was also observed for the ablated mass and melt height. It is noticeable that the ejected mass in the case of argon and air ambient gas is almost the same considering the uncertainty. This can be seen from the overlapping in the measured data. This overlapping suggests that the laser ablation process has

a weak dependence on the type of ambient gas used in this study (air and argon). Comparing the results of laser ablation at 1 atm pressure using Ar and air ambient gas shown in Figure 6.2 to the results of laser ablation under vacuum discussed earlier in chapter 2, Figure 2.8, Figure 2.9, and Figure 2.10 shows another effect that arises from injecting ambient gas into the ablation chamber. This comparison shows that (1) from Figure 6.2(a) and Figure 2.8, the reduction in the ablation depth due to the presence of ambient gas is significant and varies from 50% to more than 90%, depending on the laser fluence; (2) from Figure 6.2(b) and Figure 2.9, at a high laser fluence (>23 J/cm^2), the reduction in the amount of mass removed from the target due to the presence of ambient gas can reach up to 95% reduction; and (3) from Figure 6.2(c) and Figure 2.10, a reduction in the height of the molten layer is also observable in the case of argon gas and can reach up to 72% reduction.

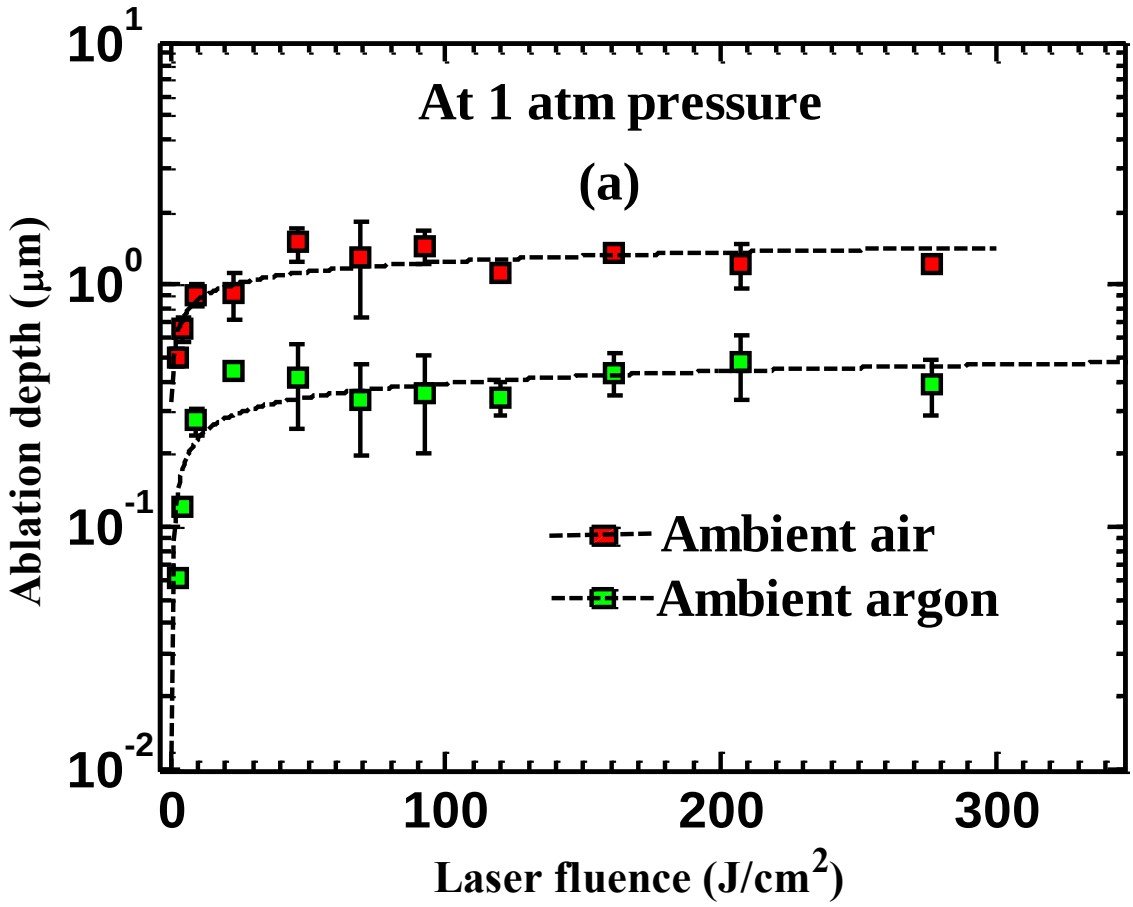

Figure 6.2. Illustrates the effect of ambient gas on laser ablation of aluminum: (a) ablation depth, (b) ablated mass, and (c) melting height.

Figure 6.2 continued

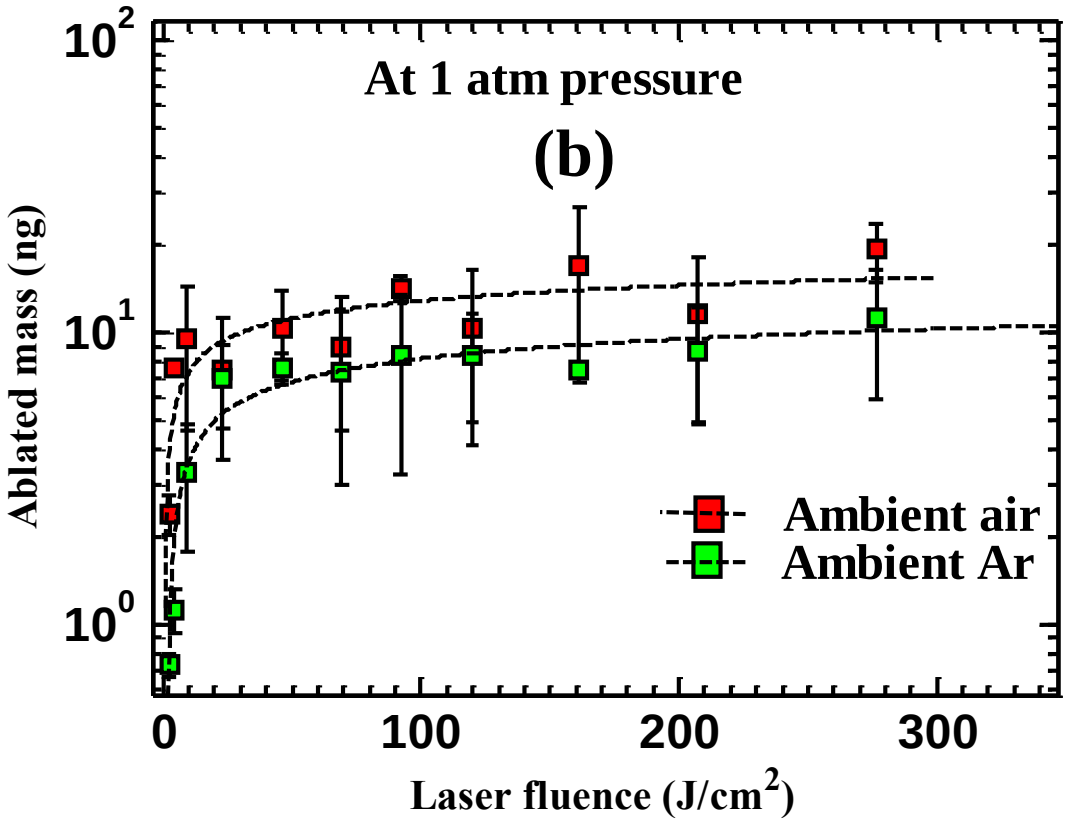

Figure 6.2 continued

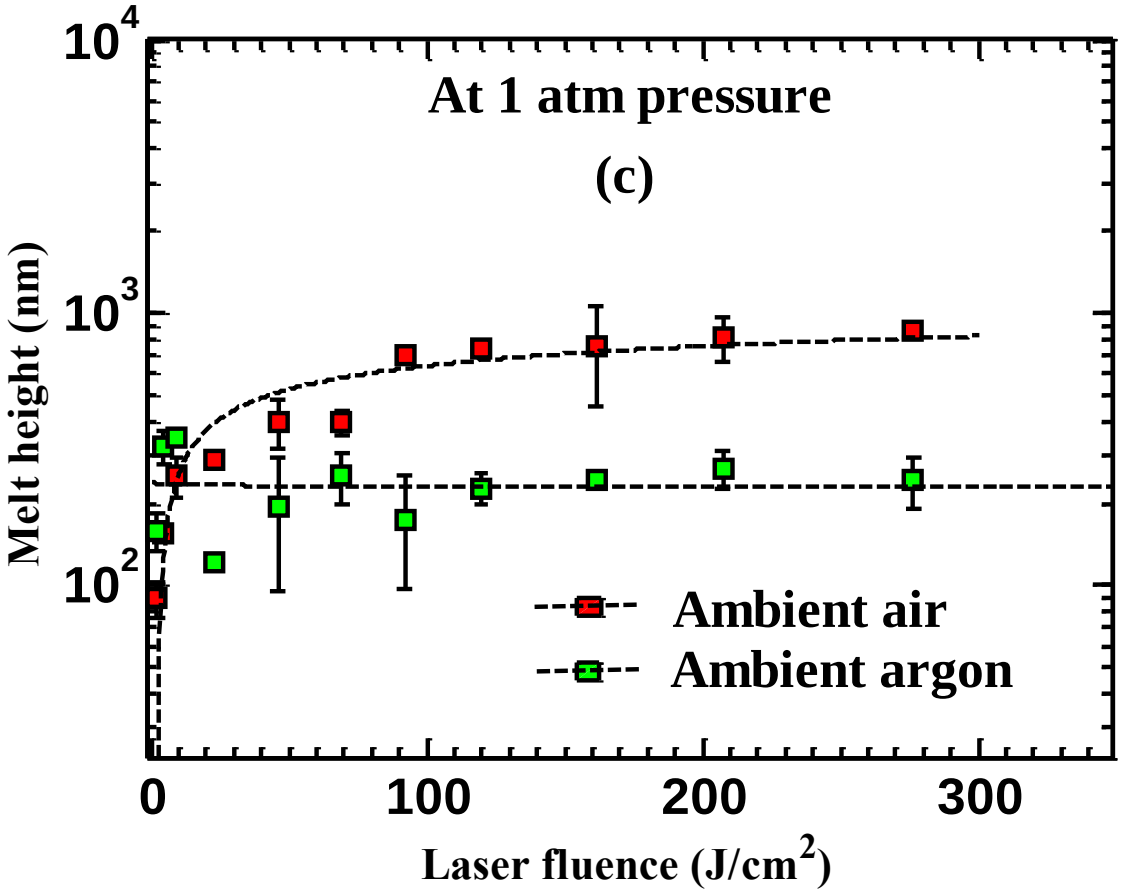

In practice, the ablation yield is a process controlled mainly by the dynamics (the propagating speed, the expansion rate, plasma density, and plasma temperature) of the ablated plume. Figure 6.3 is a time-scale diagram to illustrate the evolution of the ablated plume on a time scale relative to the laser pulse duration. The formation of the ablated plume occurs at an early time with respect to the laser pulse duration. At an early time with low plasma density, the pressure inside the plume is negligible compared with the ambient pressure; consequently, the pressure on the target surface is equal to the ambient pressure. Afterward, as the plasma density and pressure in the plume increase significantly as a result, the pressure on the target surface tends to be equal to the pressure at the bottom of the plume. Consequently, the plume propagates freely, independent of the type of ambient gas as long as it is under the same pressure [73,74]. This made the effect of the argon and air ambient gas on the total mass ablation negligible. Simultaneously, due to the relatively long pulse duration of the incident laser pulse, the plume tends to interact with the remaining part of the

incident laser pulse either via absorption of laser energy in the plume by inverse bremsstrahlung or direct ionization by incident laser photons. This is followed by a significant increase in the electron plasma density in the plume [75]. Gradually, as the electron number density increases, the amount of laser energy that can reach the target's surface decreases. Once the electron plasma density reaches the critical plasma density of the incident laser pulse, the plasma shields the remaining part of the incident laser energy completely; this is called the plasma shielding effect [76]. The plasma shielding effect, in turn, terminates the amount of mass that can be removed from the target. The plasma shielding effect is significant at high laser fluence as shown in Figure 6.2 and pronounced when ablating the target in the presence of ambient gas as shown in Figure 6.2, as the ambient gas limits the adiabatic expansion of the plume. It worth mentioning here that the adiabatic expansion of the plume decreases the electron plasma density. Once the plume propagates in the ambient gas, it creates an external shockwave. This external shockwave compresses the gas in front of the plume. Consequently, on the one hand, this compressed layer of ambient gas tends to confine the ablated plume, and on the other hand, it tends to interact with the incident laser, via either photon absorption or photon scattering. Consequently, this compressed ambient gas tends to act as another barrier along with the plasma plume to prevent the laser energy from reaching the target surface.

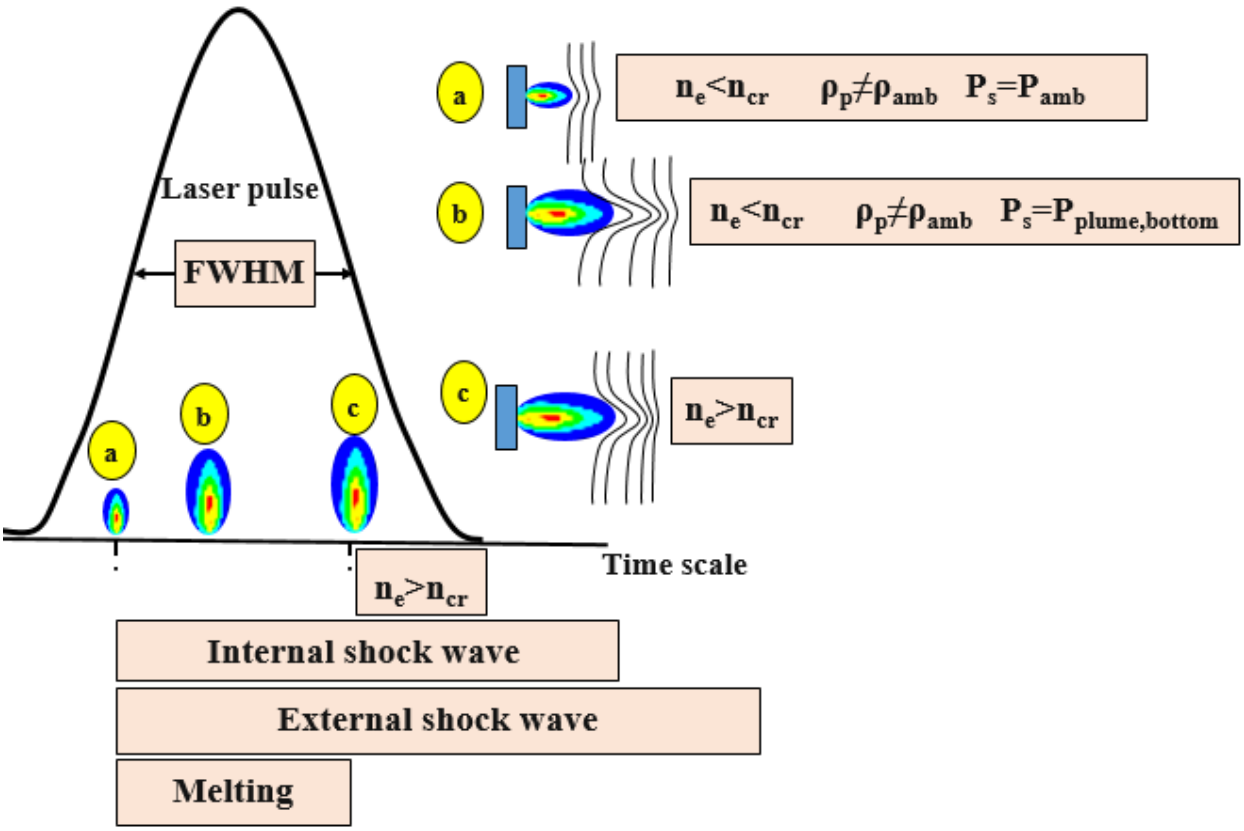

Figure 6.3. Schematic illustrating the temporal evolution of the ablated plume relative to the laser pulse duration

6.4 Effect of Ambient Gas Pressure on Laser Ablation

To understand the role of the ambient pressure on laser ablation, another experiment was conducted at two different ambient pressures (10 Torr and 760 Torr) using argon as a background gas. The results of this experiment are shown in

Figure 6.4. Increasing the ambient pressure from 10 Torr to 760 Torr has a pronounced effect on the laser ablation process, mainly at high laser fluence. This effect can be seen from decreasing the ablation depth,

Figure 6.4(a), ablated mass,

Figure 6.4(b), and the height of the molten layer. This reduction of the ablation yield resulting from increasing the ambient pressure is consistent with the physical picture of plasma plume dynamics that was drawn in the section above. Furthermore, saturation in ablation depth at laser

fluence >20 J/cm^2 indicates a strong plasma shielding effect, while as the pressure decreases, the ablation depth exhibits a continuous increase with increasing the incident laser fluence. Comparing ablation depths obtained at 10 Torr and 760 Torr at high fluence, it is shown that ablation depth decreases by 50 times at 760 Torr. Similarly, results in

Figure 6.4(b) indicates that, the mass removal has the same trend as the ablation depth

Figure 6.4(a). At high pressure (760 Torr) the mass removal rate stops to increase for fluences higher than 20 J/cm^2, while at low pressure (10 Torr), a slight increase is still observable. Two orders of magnitude of mass reduction were observed due to an increase in ambient gas pressure from10 Torr to 760 Torr. The height of the melt was also observed to decrease by one order of magnitude because of increasing ambient gas pressure from 10 Torr to 760 Torr. Comparing the Al results obtained at high pressure of 760 Torr with the results obtained under vacuum (chapter 2) illustrates the importance of ambient gas pressure on metal ablation. First, a significant reduction in ablated mass is observed. This reduction can be more than 95%, depending on the laser fluence. Second, the shielding effect is significant when using high pressure ambient gas. This is evident from the termination

of material removal observed at laser fluences >20 J/cm^2.

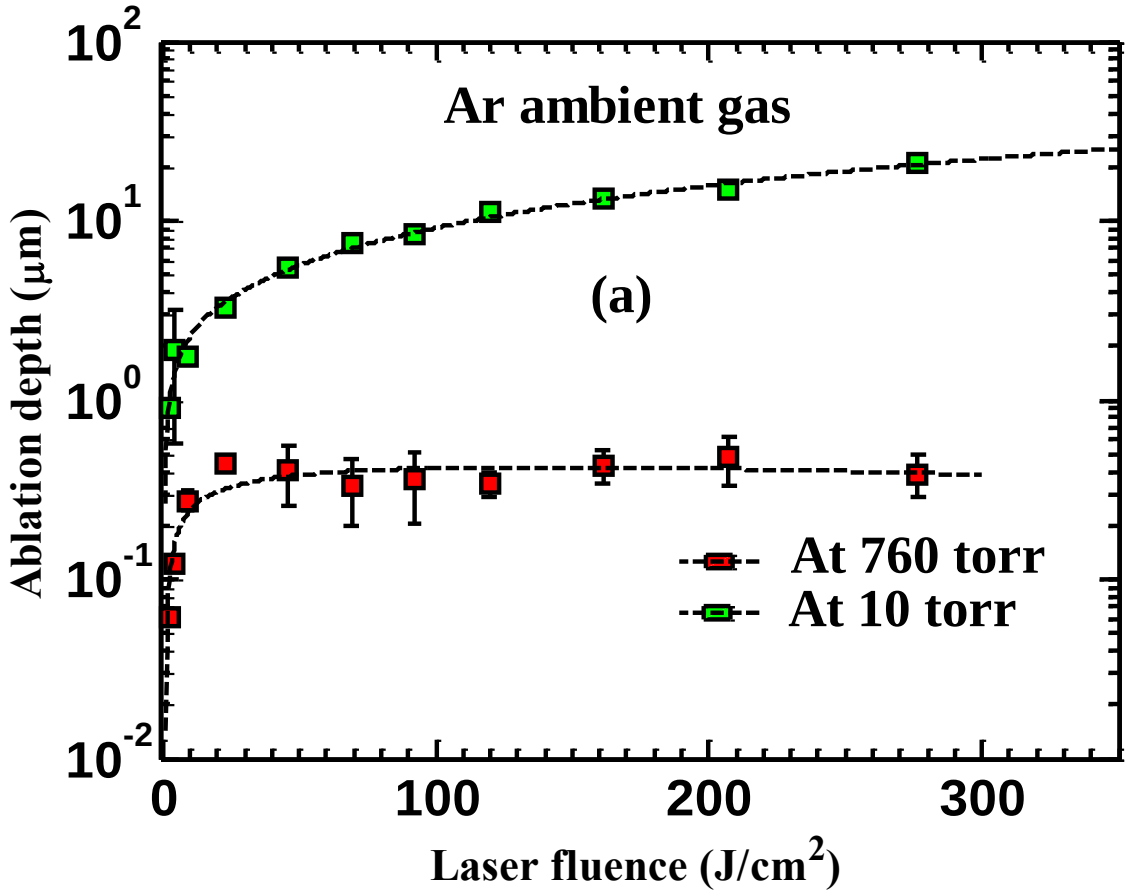

Figure 6.4. Effect of ambient pressure effect on the ablation of aluminum: (a) ablation depth, (b) ablated mass, and (c) melting height

Figure 6.4 Continued

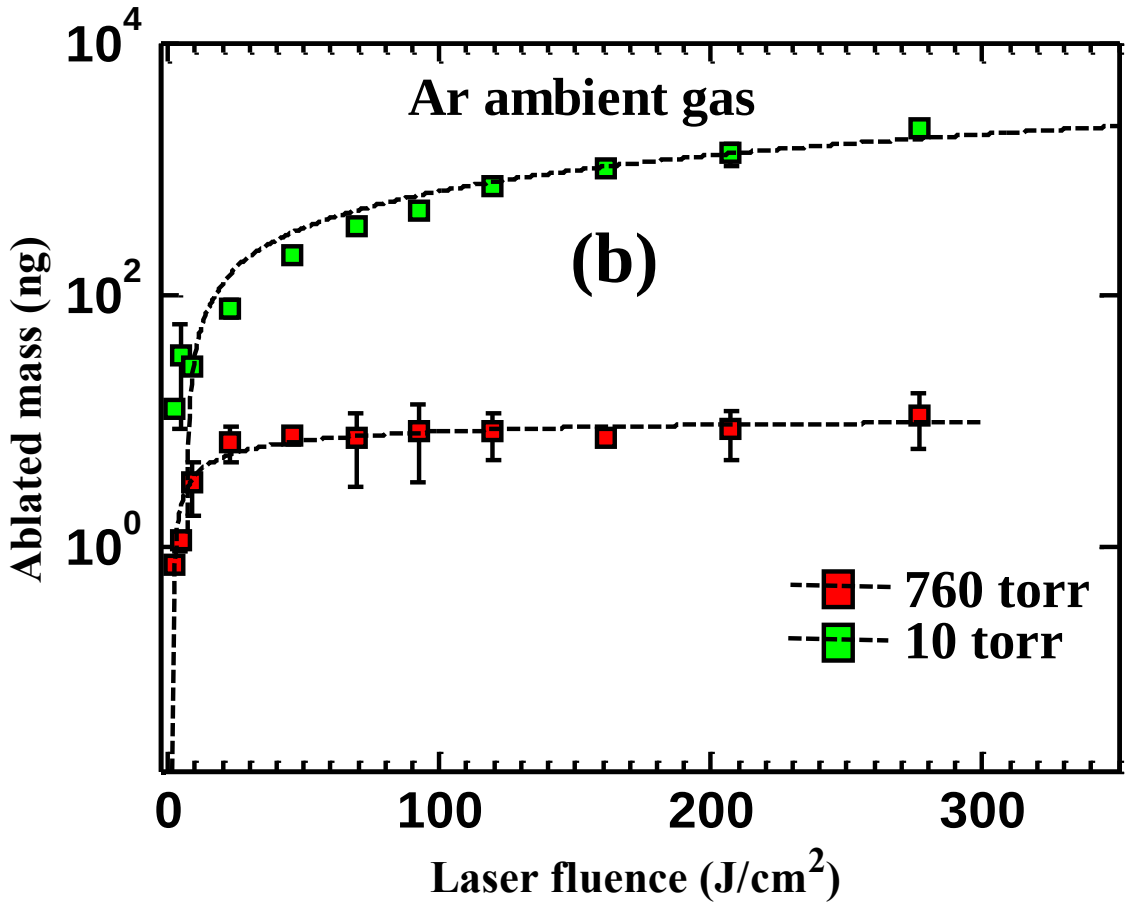

Figure 6.4 Continued

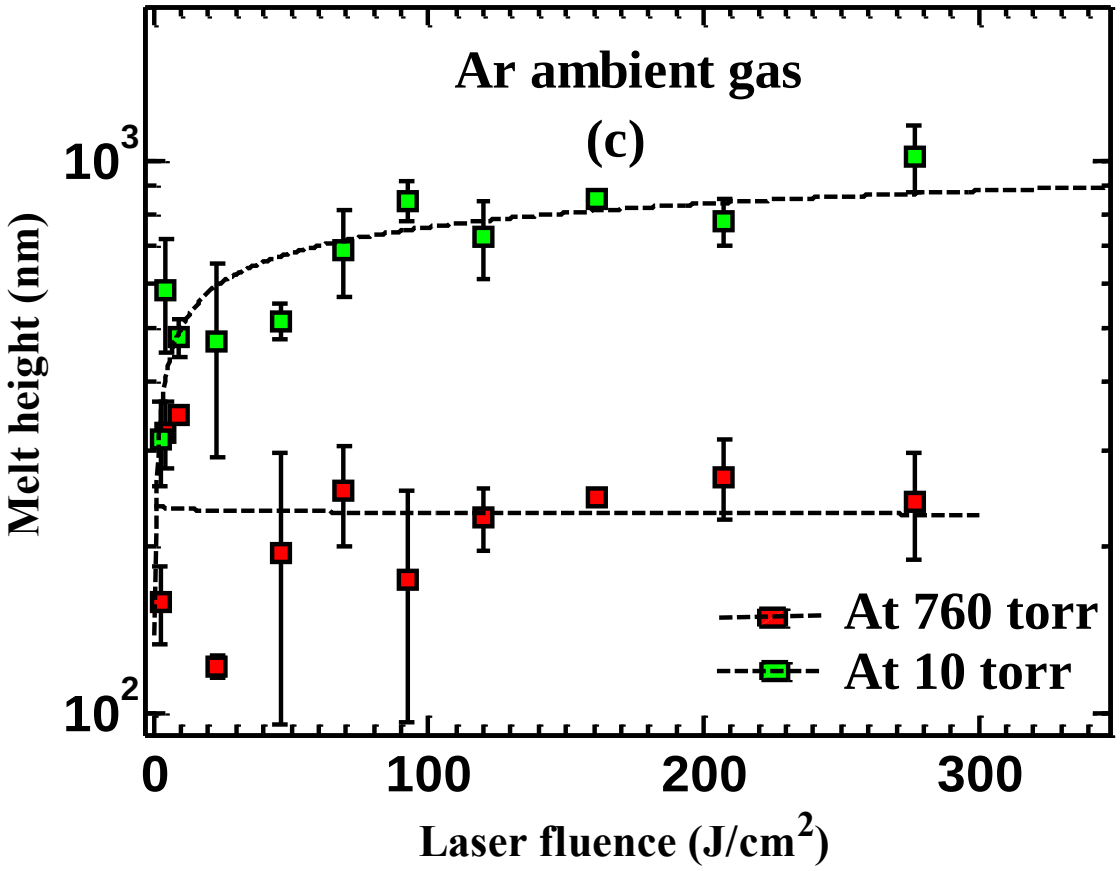

In summary, ablated plume tends to play a major role in nanosecond laser-material interaction. This role becomes more significant as the ambient pressure increases. The presence of ambient pressure and ambient gas makes the plasma shielding effect more pronounced; consequently, the amount of laser energy that can reach the target material decreases. Plasma plume dynamics expressed in its propagating speed, expansion rate, temperature, and plasma density are factors that are influenced by the ambient conditions. Confining the plume due to the presence of ambient gas at high pressure leads to exposing the target material to extreme conditions of irradiation consisting of ion, electron, photon, and thermal radiation occurring simultaneously. Such conditions can be used to study the erosion that happens to the material when exposed to an environment of elevated temperatures and high flux and energy radiation similar to the fusion reactor.

CHAPTER 7. ULTRAFAST LASER-PRODUCED NANOPARTICLES

7.1 Background

Nowadays, nanoparticles play an essential role in medical and industrial applications. The capability to load the drug on nanoparticles then deliver it to the affected cell caused a revolutionary improvement in cancer treatment. Solar cell fabrication and semiconductor industries that require thin film fabrication are mainly dependent on the formation of nanoparticles. Conventionally, ion beam sputtering and nanosecond pulsed laser were widely used for thin film fabrication and nanoparticle formation. In this chapter, the physics involved in this process were intensively studied and some limitations were stated, such as the formation of microdroplets and particulates on the deposited film, nanoparticles size control, and yield efficiency.

7.2 Experimental Setup

For this experiment we used a chirped pulse amplifier (CPA) laser system that consists of SynergyTM Mirror-dispersion-controlled Ti:Sapphire oscillator producing 75 MHz, 40 fs at full width at half maximum (FWHM) pulse duration, 800 nm wavelength, and 10 nJ laser beam. The beam passes through a stretcher to increase the pulse duration hence decreasing the laser intensity, regen-amplifier for power amplification, and then is compressed back to the 40 fs pulse duration. The final output is a P-polarized laser pulse of 10 Hz, 40 fs, 800 nm, with 110 mJ maximum energy. Such a system provides a tunable laser power ranges from tens of gigawatts up to several terawatts. When using such a high laser power, the laser pre-pulse/contrast ratio must be considered. For this purpose, the noise around the main pulse was measured in the delay range of about -500 ps to 180 ps, and the picosecond contrast ratio was found to be $1x10^{-8}$. The parasitic pulses arriving at greater than 1 ns delay around the main pulse were also measured and the nanosecond contrast ratio was found to be $1x10^{-7}$. Consequently, the effects of both post- and pre-pulses, either pico- or nanosecond, can be ignored, and the output laser can be assumed to be pure femtosecond laser. A set of half waveplate and thin film polarizer positioned before the compressor enabled tuning the output laser energy. Outside the compressor, the laser beam goes through a 14-mm aperture shutter. The shutter was controlled by a delay time generator to allow a single pulse ablation mode. A

99.99%, 1 mm thick Sn was used as a target for this study and it was placed on an XY translation stage inside a vacuum chamber (10^{-6} Torr) as shown in Figure 7.1. The laser entered the chamber through a quartz window and then focused on the sample using a 10 cm plano-convex lens. The laser spot size on the target surface was measured to be 100 µm diameter and kept constant throughout the entire experiment. The ejected particles got deposited on a Si wafer mounted 20º off normal to the target and kept 3 cm away from the surface. Atomic Force Microscope (AFM) was used to measure the size of the ejected nanoparticles.

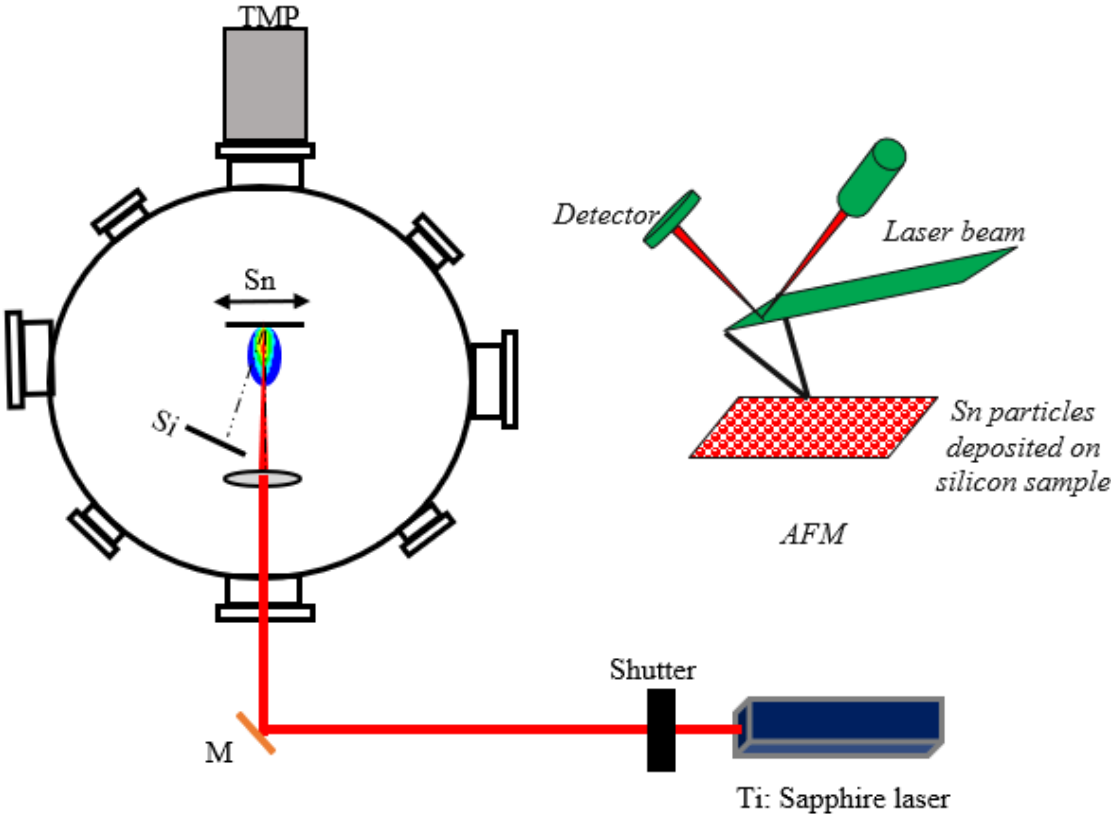

Figure 7.1. Schematic of the experimental setup

7.3 Ejection of Nanoparticles Using Ultrafast Laser

For this purpose, the Sn target was irradiated at different fluences, and the ablated particles were deposited on a Si wafer mounted 3 cm away from the target and at 20º off normal to the target surface. Irradiating the target surface with 5.4 J/cm^2 laser fluence demonstrated that as a result of

100 successive laser shots, the size distribution of the ejected particles follows a log-normal distribution. This distribution varies from 20 nm to 60 nm in diameter and has a peak value at 25 nm and a standard deviation of 3.4 nm, as shown in Figure 7.2(a). A previous study [40] was conducted on Si sample to generate Si nanoparticles using 0.5 J/cm^2 laser fluence, 780 nm wavelength, 120 fs FWHM pulse duration, reported that the nanoparticles have a peak value at 14 nm in diameter. This result is in a close agreement with what is observed at laser fluence 5.4 J/cm^2, given the difference in material properties between Si and Sn in addition to the difference in laser pulse duration. At a higher laser fluence (40.5 J/cm^2), the particle size distribution shifts to a larger size, and the distribution shows a peak value at around 40 nm and yielding a wider distribution with a 10 nm standard deviation.

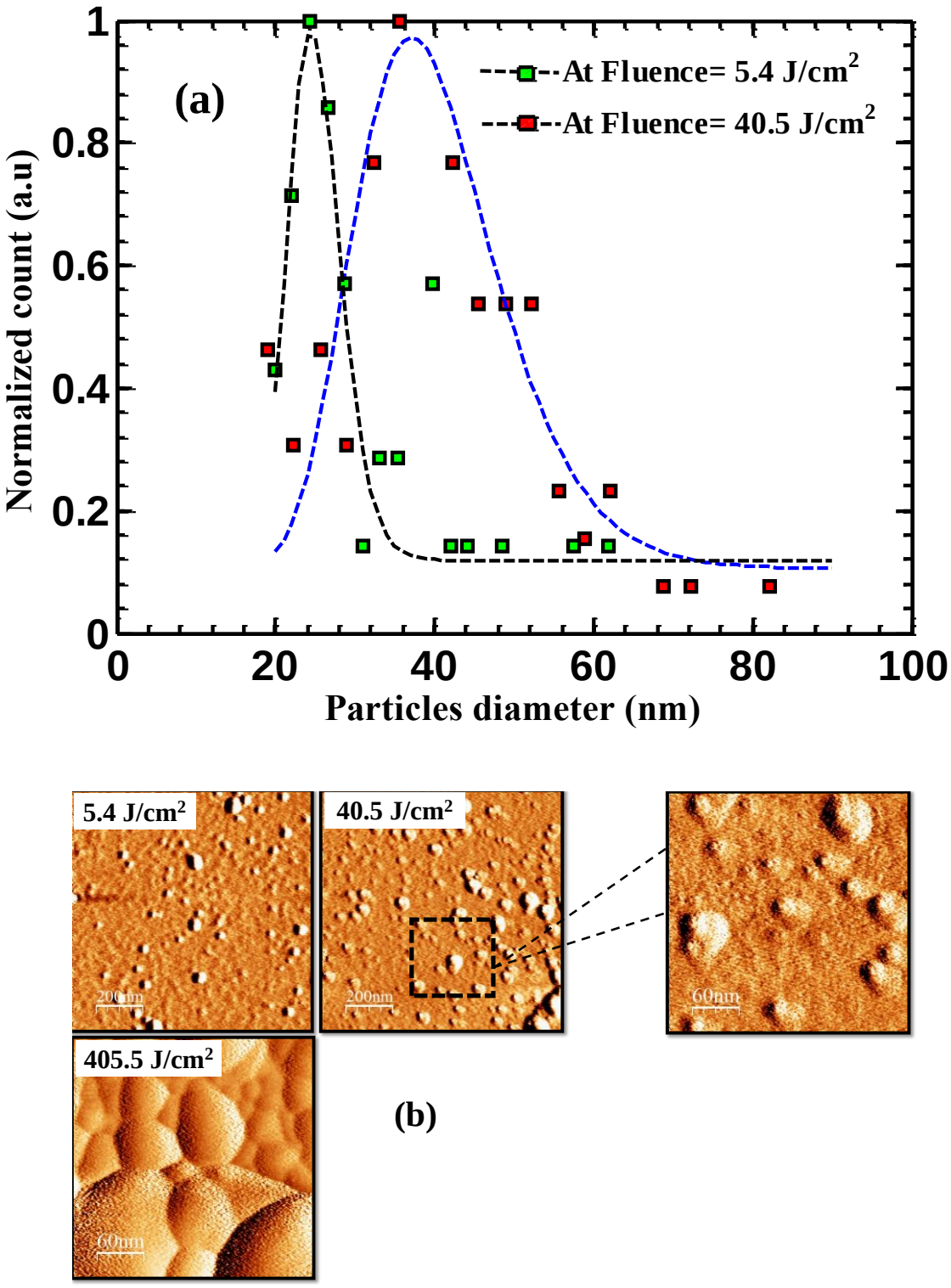

Figure 7.2. Size distribution of Sn nanoparticles generated from ultrafast laser ablation at different fluences: (a) particle size distribution, (b) AFM images to show the coagulation occurs at higher laser fluence.

The driving mechanism for nanoparticles formation using ultrafast laser ablation has been studied and predicted via simulation [41,42]. At such laser fluence, compared to ablation threshold fluence, the relaxation of the thermoelastic stress that is caused by rapid heating to the target after laser irradiation induces a high-speed expanding fluid. This creates spatially nonuniform high strain rates. Consequently, this high strain gradient leads to mechanical bond breakage and fluid fragmentation, hence nanoparticle formation. According to these models [41,42], as the lattice temperature increases the gradient in the expanding fluid's velocity increases as well, and hence the initial strain. Consequently, increasing the incident laser fluence should generate fragments/nanoparticles with a smaller size. These models, however, provide a description of the particles formed during the initial stages of ablation, but experimentally, these nanoparticles can coagulate during transportation and deposition on the wafer forming larger particle sizes on the wafer surface. Additionally, using 100 successive laser shots would further lead to the accumulation of the particles on top of each other at the wafer surface after each shot, particularly at higher fluences. This is clear from Figure 7.2(b) where nanoparticles coagulation can be seen at 40.5 J/cm^2 and even more pronounced at 405.5 J/cm^2, at which it forms a solid thin film compared to results from 5.4 J/cm^2 fluences. It should be noted that increasing the incident laser fluence increases the total ablated particles, too, leading to a high probability of particles coagulation.

CHAPTER 8. EXTREME ULTRAVIOLET (EUV) LIGHT SOURCE GENERATION FOR LITHOGRAPHY APPLICATIONS

8.1 Background

Extreme ultraviolet (EUV) photons are currently considered as the light source for the next generation of semiconductors and nanofabrication. Discharge-produced plasma (DPP) devices were intensively studied as sources for EUV light generation. However, the low conversion efficiency of the DPP devices and other factors affecting the lifetime of these devices have impeded significant progress. Consequently, laser-produced plasma (LPP) is currently being pursued as the prime EUV light source. The EUV generated from LPP was found to have higher power conversion efficiency compared to DPP devices. However, the conversion efficiency from LPP devices is still insufficient for the throughput required by industry for high-volume manufacturing. Furthermore, the debris generated during LPP exhibits a serious challenge for the sensitive and expensive optical collection system. The deposition of plasma debris on mirrors used for EUV photon collection decreases the reflectivity and lowering the lifetime of such a mirror. Currently, the EUV light is generated from laser interaction with liquid droplets injected at high frequency. The conversion efficiency and the repetition rate are still a major challenging task. In this chapter the debris generated from Nd:YAG laser-planar Sn target interaction, and a way to mitigate them, is discussed.

8.2 Experimental Setup

Figure 8.1 is a diagram of the experimental setup used in this study to mitigate the ion debris accompanying EUV photon generation. The EUV photons were generated using a 6 ns pulse duration (FWHM), 1064 nm wavelength, P-polarized Nd:YAG laser that delivers up to 300 mJ energy that was focused down to 1.8×10^{-4} cm^2 spot size on the target surface using an f/40 Plano-convex lens. The generated EUV energy was measured using a calibrated EUV power tool mounted at 45º off-normal to the target. The EUV power tool consists of two 200 nm Zr filters, a Mo/Si mirror, and a EUV photodiode, which collects 13.5 nm wavelength light within a 2% bandwidth. To detect and characterize the generated ions, a Faraday Cup (FC) ion collector placed at 20º off-normal to the target at 10 cm away from the target surface was used to measure the ion

Time-of-Flight (TOF). Signals from the FC and EUV power tool were acquired and stored using a 1 GHz digital Tektronix oscilloscope. To mitigate the ions' debris and prevent them from reaching the surface of the collecting mirror, an ultrafast laser was used first to fragment the target to generate a cloud of fragments (charged particles, neutral atoms, and nanoparticles) that act as an attenuating medium to the ions generated Nd:YAG laser-target interaction. The ultrafast laser has Ti:Sapphire crystal and delivers 40 fs pulse duration (FWHM), 800 nm wavelength; P-polarized Ti:Sapphire laser delivers up to 2 mJ energy focused down to 0.8×10^{-5} cm^2 spot size on the target surface using an f/50 Plano-convex lens. The Ti:Sapphire laser was delivered first to ablate a 1 mm thick 99.99% tin target. Ablating the tin target generates charged particles, neutral atoms, and nanoclusters. These ablation products expand away from the target at different speeds. The expanding particles were imaged using an f/10 Plano-convex lens that forms an inverted image on an Andor ICCD camera used for fast imaging. The fast imaging technique was used along with a neutral density filter to image tin ablated plume at a different time delay. A Si wafer placed 1 cm away from the target was used to collect the nanoparticles produced from Ti:Sapphire laser-tin target ablation. Then, an Atomic Force Microscope (AFM) was used to measure the size of these nanoparticles. A WLP was used to measure the ablation profile consequently the total ejected mass. A time delay generator was used to synchronize the Ti:Sapphire and Nd:YAG lasers in addition to the ICCD camera. The experiment was conducted under 10^{-6} Torr.

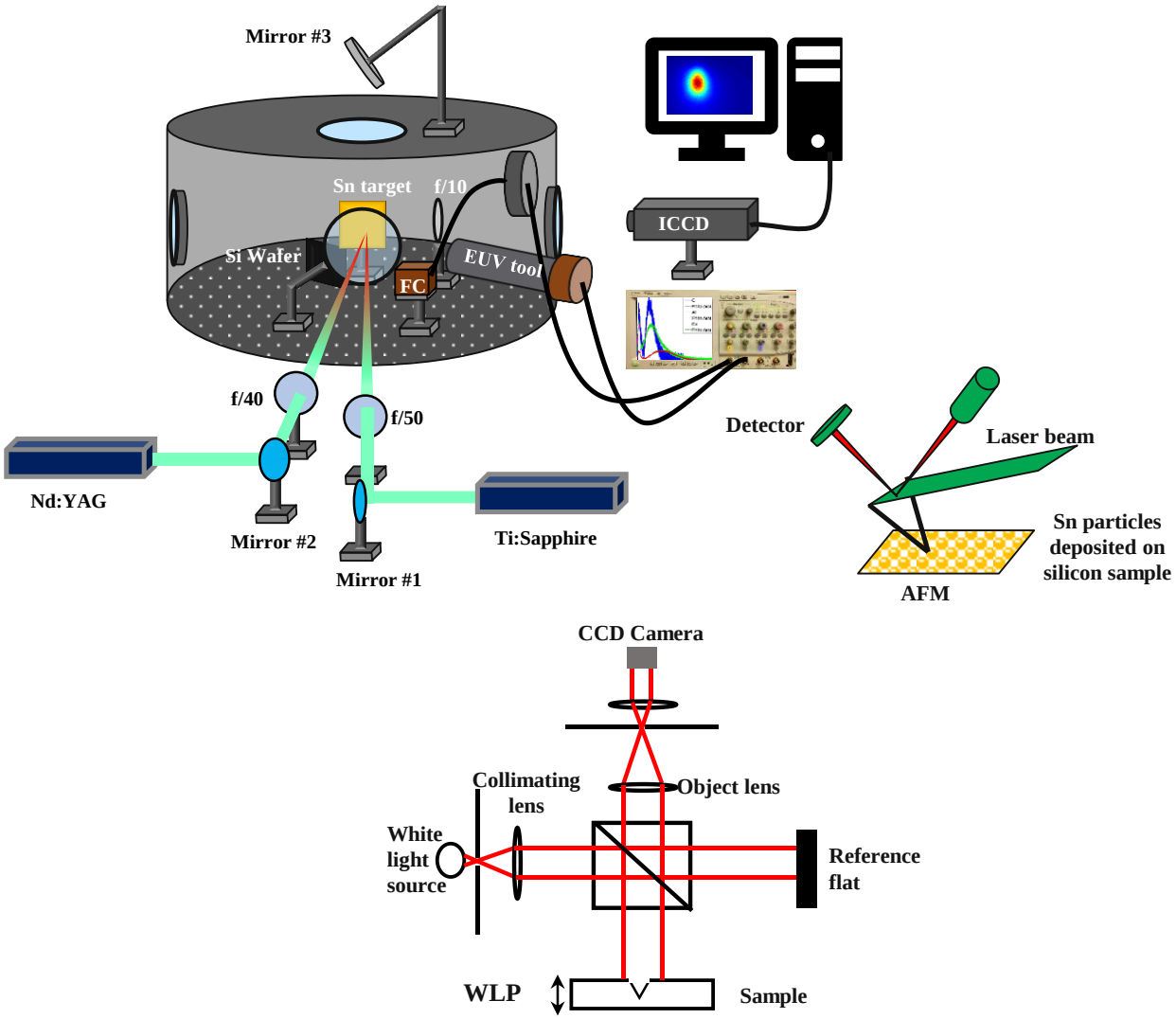

Figure 8.1 Experimental setup.

8.3 Preconditions for EUV Generation using Ultrafast Laser

8.3.1 Ultrafast Laser Ablation

Coupling laser energy with target material goes through consecutive steps. At first, the electrons in the target material absorb the incident photons via inverse Bremsstrahlung and gain high energy. Relaxation between electrons (electron-electron) occurs within a fraction of femtoseconds, causing the formation of an electronic compression wave. Then, these electrons transfer their energy to

lattice atoms leading to further ionization and excitation of the target material. Hence, after a few picoseconds, relaxation between the electrons and lattice atoms takes place, resulting in increasing ionic pressure. Then, the energy carriers (electrons and ions) carry the laser energy deep in the target material leading to material melting and vaporization [41]. Eventually, this thermal stress results in a high-speed expanding fluid. In turn, a spatially nonuniform high strain rate forms. Mechanical bond breakage and fluid fragmentation occur accordingly, leading to the formation of nanoparticles [41,42]. Figure 8.2 shows the ablation profile resulting from irradiating the tin target with the Ti:Sapphire laser at intensity 6.4×10^{14} W/cm^2. From the ablation profile, the total ablated mass can be inferred to be around 0.036 µg.

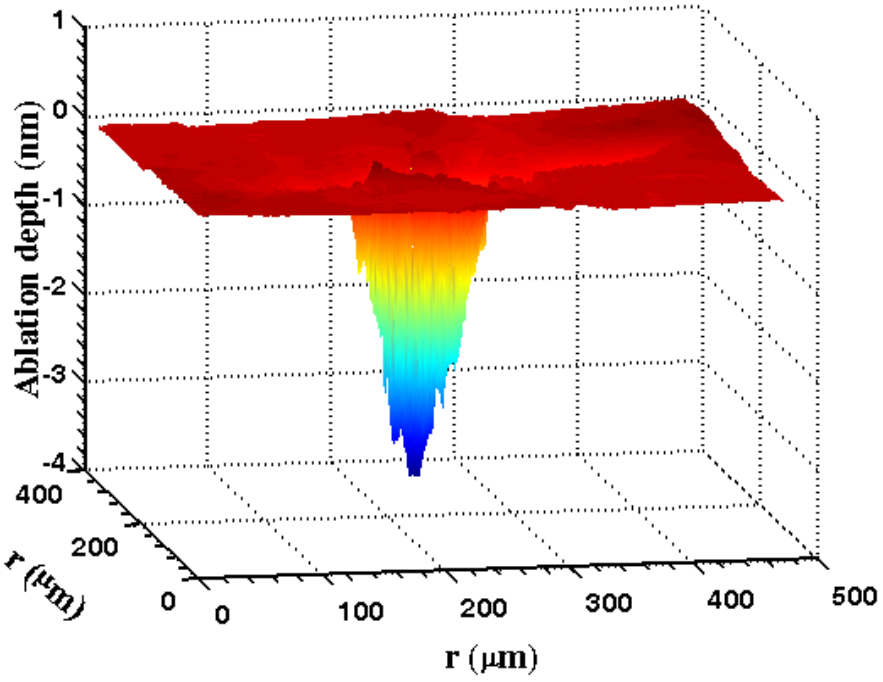

Figure 8.2 Ablation profile resulting from 6.4×10^{14} W/cm^2 Ti:Sapphire laser-tin planar target interaction

This ablated mass contains charged particles, neutral atoms, and nanoclusters. A silicon wafer placed 1 cm away from the target and 20º off normal to the target surface was used to deposit these particles on its surface. Figure 8.3 shows that the size of these particles varies from a few tens of nanometers to hundreds of nanometers in diameter. It worth mentioning here that there is an absence of a big chunk of molten material or even microdroplets. The absence of large size

particles gives an advantage to ultrafast laser over other short pulse lasers like nanosecond laser, for example.

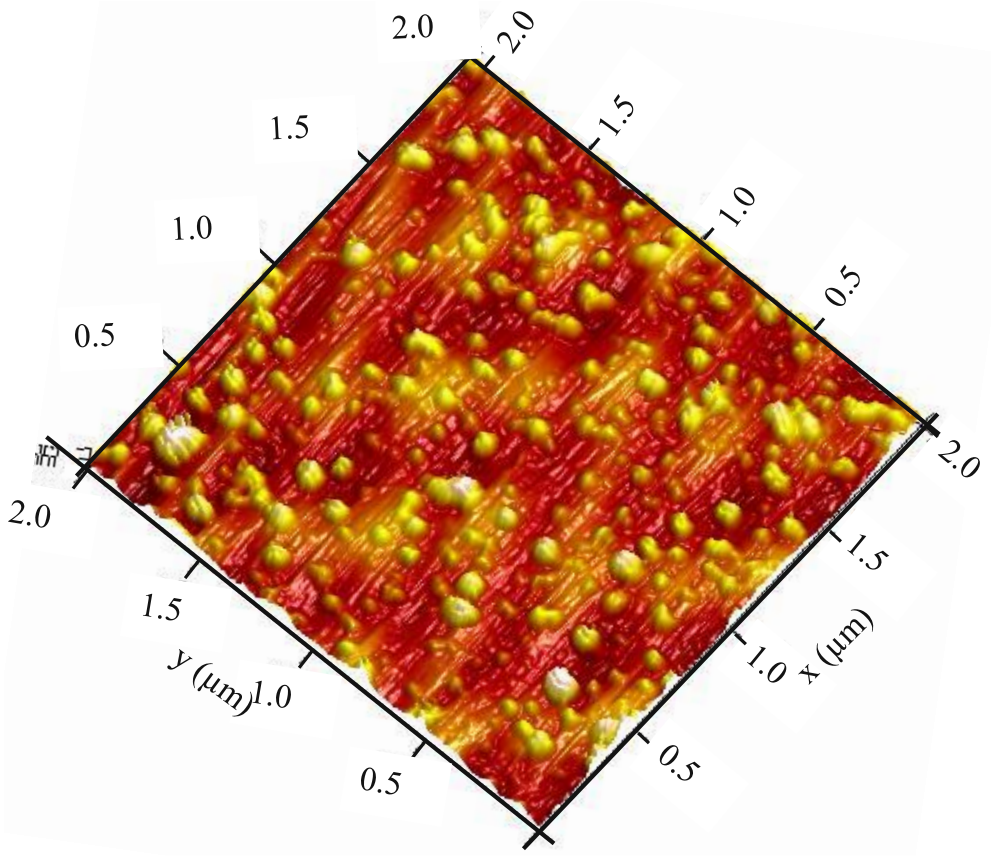

Figure 8.3. Illustrates the absence of tin microdroplets and even molten material. The nanoparticles were generated using 6.4×10^{14} W/cm^2 Ti:Sapphire laser and accumulated from 10 laser shots.

8.3.2 Ultrafast Laser-Produced Plasma

As mentioned above, the ablated mass contains charged particles, neutral atoms, and nanoparticles. The population and expanding speed of each species are different. Knowing the expanding speed of these particles is needed in characterizing the preconditions for EUV photons generation as these species will play a role in mitigating the ions debris, as it is propose in this work. For this purpose, a fast imaging technique using an ICCD camera combined with a neutral density filter

was used to image the plume at different time delay to find the propagating speed of the ejected plume. Figure 8.4 shows the expansion of the ablated plume resulting from irradiating the Sn target with the Ti:Sapphire laser at an intensity of 6.4×10^{14} W/cm^2. The temporal evolution of such a plume was obtained by tracking the point of maximum intensity within the plume; results are shown in Figure 8.5. Linear fitting to the data presented in Figure 8.5 shows that the propagating speed of the plume is 1.8 ± 0.1 μm/ns, while at an early time (<50 ns), the plume has a faster-propagating speed; as shown by the insertion in the same figure, it is 14.6 ± 0.5 μm/ns. It is worth mentioning here that the plume is a combination of different particles with a different population and even speeds such as neutral atoms and ions. Tracking the plume gives an average propagating speed of these particles, which is shown at a time larger than 50 ns, whereas at a time of less than 50 ns, when the photon emission is mainly coming from the fast species, which are the ejected ions, tracking the plume gives an average speed of the ejected ions. This can be confirmed by measuring the ion TOF using FC detector, as shown in Figure 8.6, which shows that the peak value of the propagating speed of the ions is 12.0 ± 0.4 μm/ns in a good agreement with the speed measured by tracking the plume at a time less than 50 ns. Furthermore, the peak ion flux density was measured to be 5.0 ± 0.2 mA/cm^2.

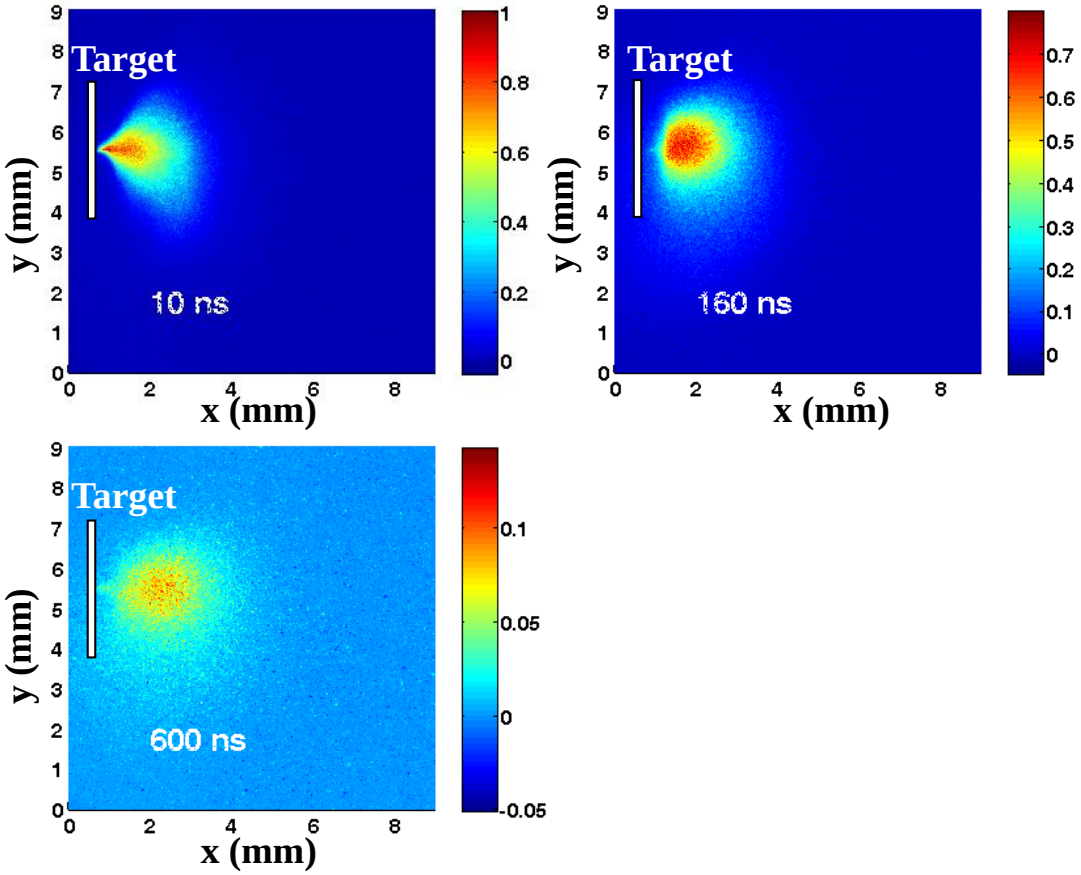

Figure 8.4. Expansion of Tin ablated plume using 6.4×10^{14} W/cm^2 Ti:Sapphire laser. Laser propagates from right to left. For comparison, the color scales of all the subfigures are normalized over the data measured at 10 ns and is given in arbitrary units.

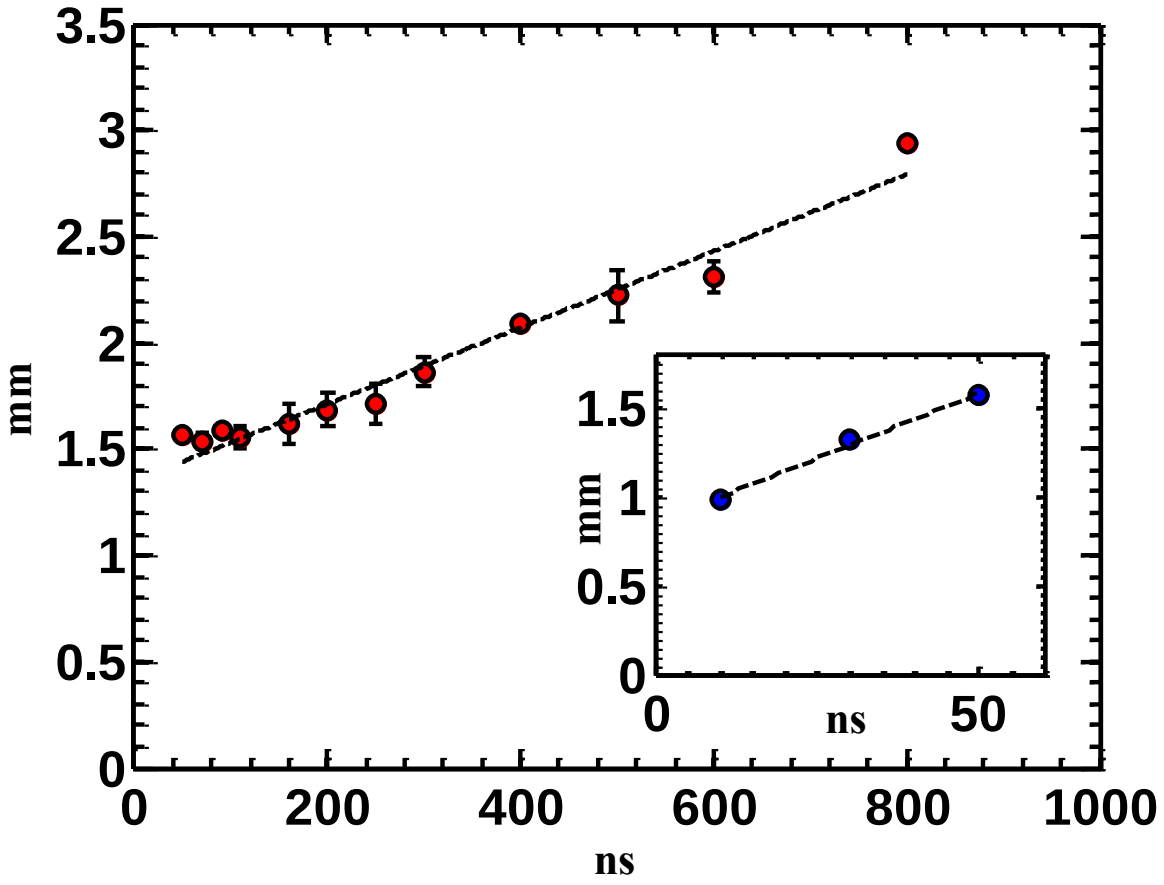

Figure 8.5. Temporal evolution of Tin plume using 6.4×10^{14} W/cm^2 Ti:Sapphire laser. The insertion shows the plume temporal evolution at a time of less than 50 ns.

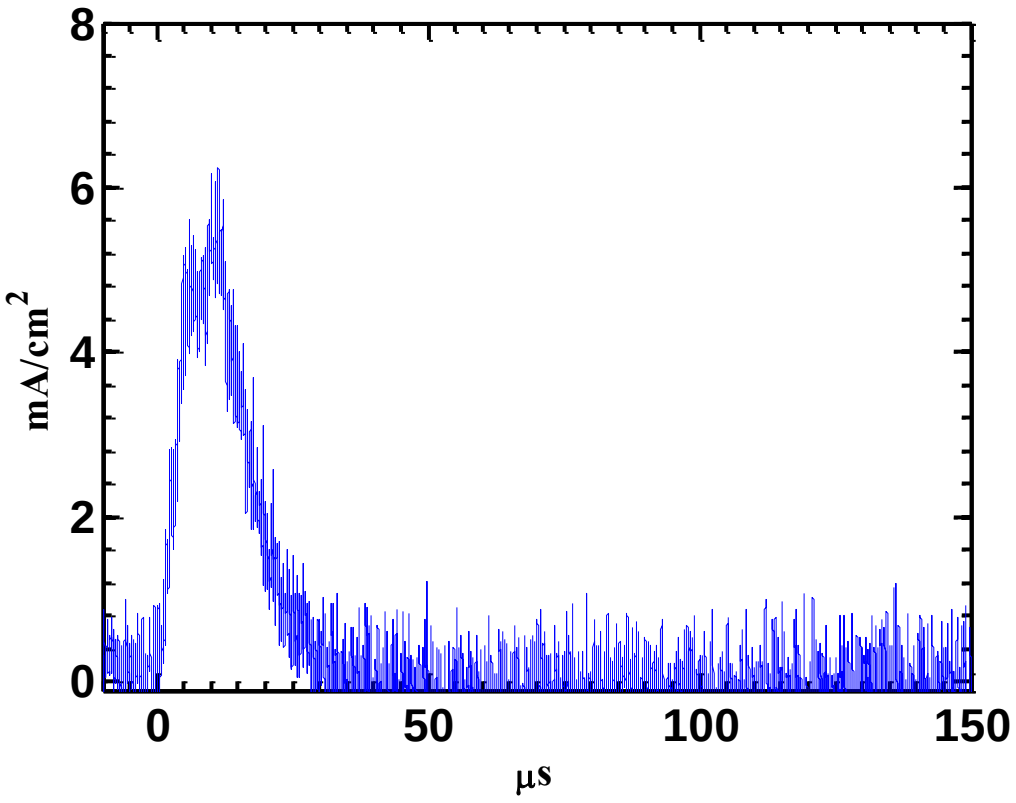

Figure 8.6 Tin ion Time-of-Flight (TOF) measured using the Faraday Cup (FC) detector placed 10 cm away from the target with 20º off-normal to the target surface

8.4 EUV Photon Generation Using Only Nanosecond Laser-Produced Plasma

Tin atomic transitions such as 4d-4f, 4p-4d, and 4d-5p transitions are the main source for EUV photons emission emitted with a wavelength near 13.5 nm. For these transitions to occur, and EUV photons to escape from the plasma without getting internally absorbed in the plume, optimum conditions of plasma temperature and plasma density have to be satisfied first. A 30 eV plasma temperature and electron plasma density ranging from $1x10^{19}$ cm^{-3} to $4x10^{19}$ cm^{-3} [77] were found to be the optimum conditions for EUV photon generation. Increasing laser intensity forms regions of high-density plasma. Therefore, the optimum temperature for EUV generation occurs within the dense plasma region. Tin plasma in a dense region has a significantly large opacity, so most of the EUV photons generated from dense plasma cannot escape and instead are internally absorbed within the plasma [77]. This results in maximum conversion efficiency (CE) occurring at moderate

laser intensity, as shown in Figure 8.7. Maximum CE was seen at $5x10^{10}$ W/cm^2 laser intensity, which is in good agreement with the work previously published [78–80]. Although improving the CE is important and there is much ongoing work is dedicated to CE enhancement [81,82], the scope of this work is mainly to mitigate the debris accompanying the EUV generation process.

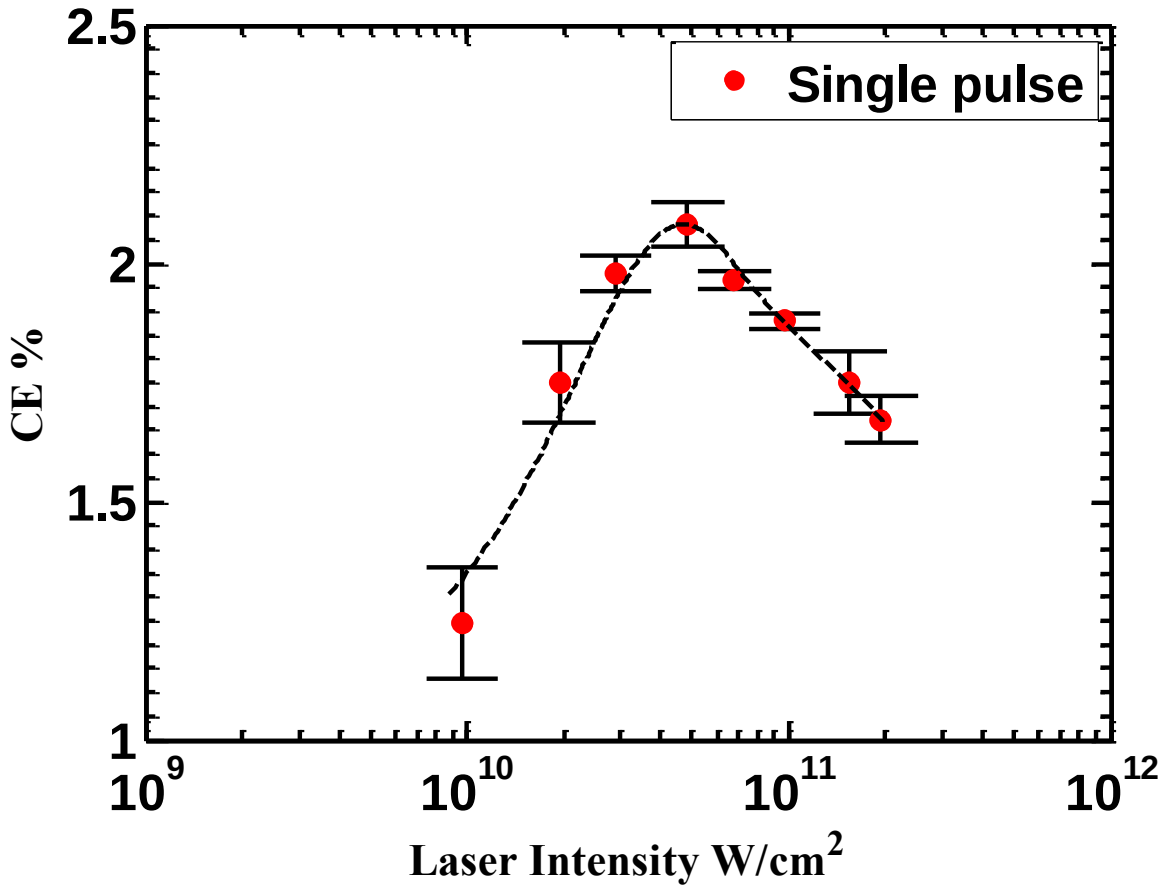

Figure 8.7. EUV conversion efficiency as a function of incident Nd:YAG laser intensity.

8.5 Effect of Preconditions on EUV Conversion Efficiency

Figure 8.8 shows the effect of the preconditions formed by the $6.4x10^{14}$ W/cm^2 Ti:Sapphire laser on the CE resulting from $5x10^{10}$ W/cm^2 Nd:YAG laser interaction with the planar tin target as a function of delay time between the two lasers. The preconditions were found to affect the CE, which was found to drop dramatically with increasing the time delay between the two lasers. This indicates the occurrence of EUV photon scattering and/or absorption inside the Ti:Sapphire ablated

plume. The drop in the CE increases until it reaches its maximum drop at around 5 μs. However, as the time delay increases beyond this value, the CE tends to recover its original value (obtained using only Nd:YAG laser). The uncertainty in the measured data comes mainly from the instability of the laser energy from shot to shot. Another point that has to be taken into account is the target surface modification, such as target drilling; this also may add to the uncertainty, as presented below. The observed reduction in the CE is taken as a negative point for the proposed system; however, this can be defeated if using a laser with a longer wavelength, such as commercially available CO_2 laser, instead of Nd:YAG laser, as longer wavelength enhances the absorption of the laser photons via the ablated plume.

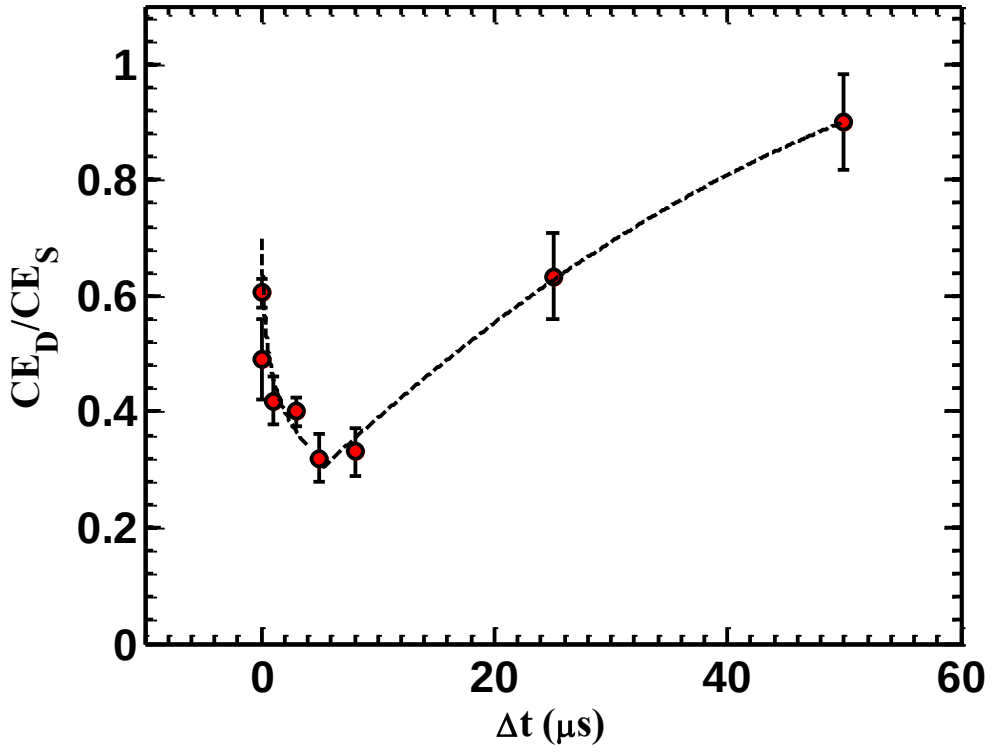

Figure 8.8. Shows the effect of preconditions formed using Ti:Sapphire laser on CE generated from Nd:YAG laser

8.6 Effect of Preconditions on Ion Debris

A FC detector was installed 10 cm away from the target surface at 20º off-normal to the target surface and was used to detect the ion's TOF. Providing the ion's TOF and the distance between the target surface and FC detector, the ion energy spectrum can be constructed. To explore the effect of the preconditions provided by 6.4×10^{14} W/cm^2 Ti:Sapphire laser on the peak ion kinetic energy accompanying the 5×10^{10} W/cm^2 Nd:YAG laser-tin target interaction, the ions' TOF was acquired at different time delays between the two lasers. Figure 8.9 shows that the effect of the preconditions on the ions' kinetic energy is similar to its effect on the CE. The drop in the kinetic energy is pronounced at the early time, and it reaches its peak after 5 μs, consistent with the CE. Similarly, it starts to recover its original value after tens of microseconds' time delay between the two lasers.

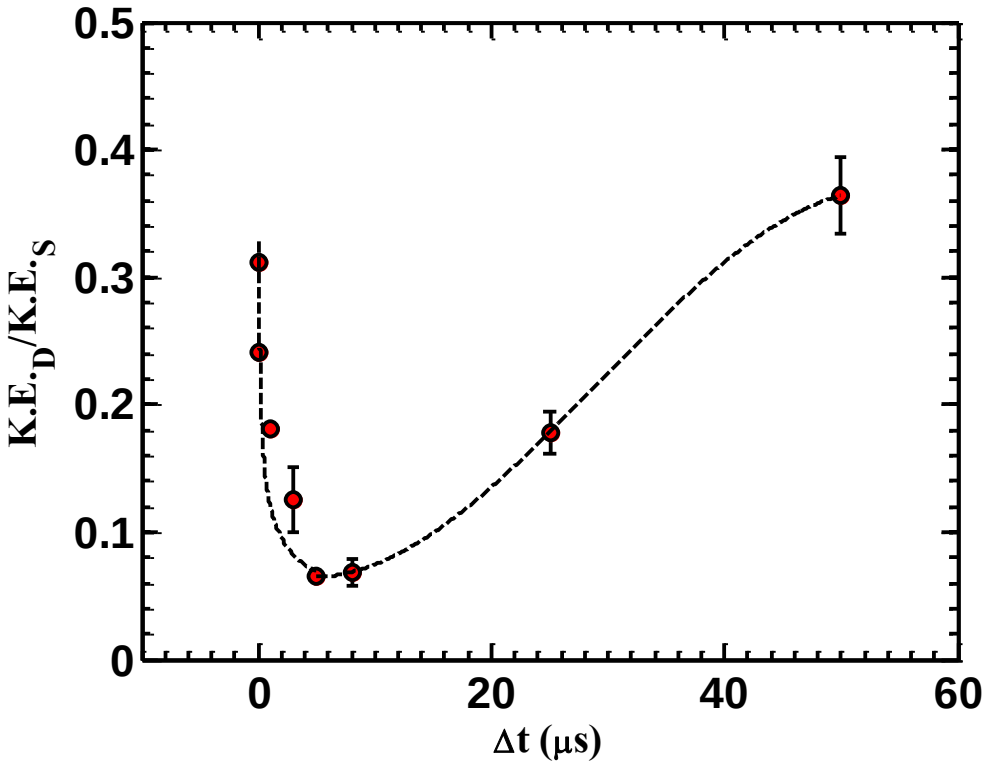

Figure 8.9. The effect of the preconditions generated using 6.4×10^{14}W/cm^2 Ti:Sapphire laser on the ion kinetic energy generated using 5×10^{10} W/cm^2 Nd:YAG laser. Subscript D refers to a double pulse and S refers to a single pulse

Figure 8.10 shows the effect of the preconditions on the ion flux, at early time delay ~100 ns, the peak flux using a double-pulse scheme tends to be in the same order or slightly higher than the peak flux using a single pulse. Minimum ion flux peak value can be achieved at almost 5 μs time delay consistent with the CE and the ion kinetic energy. Beyond this value the ion flux starts to increase again to recover its original value after tens of microseconds.

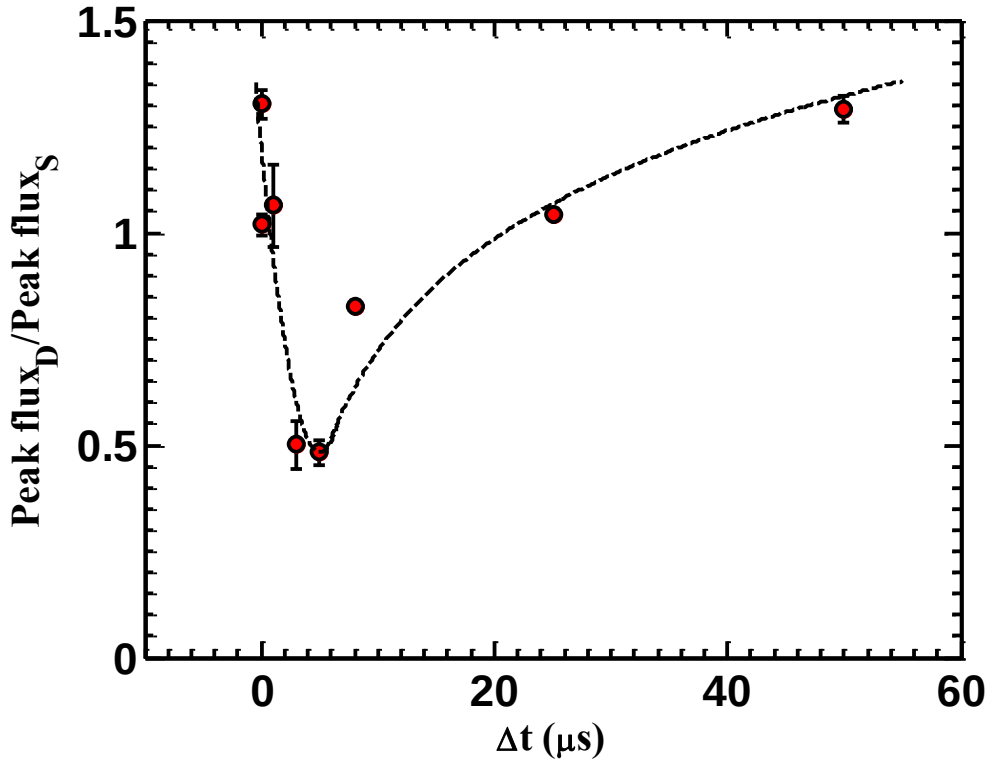

Figure 8.10. The effect of the preconditions generated using 6.4x10^{14} W/cm^2 Ti:Sapphire laser on the ion flux generated using 5x10^{10} W/cm^2 Nd:YAG laser. Subscript D refers to a double pulse, and S refers to a single pulse

Results presented in Figure 8.8, Figure 8.9, and Figure 8.10 are interconnected. To explain the reduction occurring in the ion flux, ion kinetic energy, and loss in the CE, it is meaningful to discuss the size of the plume after hundreds of nanoseconds, which is in the order of a millimeter, as shown in Figure 8.4. This is large compared to the spot size of the incident Nd:YAG laser. Consequently, scattering and/or absorption of the incident Nd:YAG laser by the plume may occur. This may lead to a further increase in the ionization state of the ejected ions by the Ti:Sapphire laser. Once the Nd:YAG laser hits the target, it will eject additional ions along with other particles,

leading to an increase in the total ejected flux. The collision of the ejected ions and photons with the Ti:Sapphire laser–ejected plume leads to the reduction in the ions kinetic energy and number of photons by absorption and/or scattering. Intuitively, as the Ti:Sapphire laser–ejected plume fades away by expansion, the reduction of the photons and ions kinetic energy decreases. At a time in the order of tens of microseconds, reduction in the kinetic energy and the photons could be due to the collision with the much slower species such as the nanoparticles.

From a quantitative point of view, a better understanding can be obtained when recalling that the Ti:Sapphire laser generates an ablated plume that propagates with a speed of about 1.8 ± 0.1 μm/ns (average speed of neutral and charged particles). This is followed by nanoparticles that expand with much less speed, considering their size and mass, which is almost one order of magnitude less than neutral atoms as measured by N. Sylvie et. al. When using short delay time (~300 ns) between Ti:Sapphire laser and Nd:YAG laser, the plume expansion distance from the target surface is almost 540 μm; this cloud of neutral atoms and ions will tend to collide with the EUV photons and ions ejected using Nd:YAG laser. While at a long time delay in the order of microseconds, collisions with neutral atoms and ions should be excluded as the ablated plume was observed to fade away due to the adiabatic expansion, as shown in Figure 8.4. However, regarding the nanoparticles that propagate with much lower propagating speed (almost one order of magnitude less than the neutral atoms), after a few microseconds, they reach almost a fraction of a millimeter away from the target. These nanoparticles again form a dense cloud around the ablated spot that tends to collide with the emitted photons and ions. The density (d) and the number of nanoparticles (N) within the Nd:YAG laser area can be estimated based on the results obtained from the insertion in Figure 8.3. Insertion in Figure 8.3 shows that the nanoparticles' density at 1 cm away from the target resulting from 10 laser shots is d=27.5 particle/cm^2; then, per single laser shot, d=2.75 particle/cm^2. Assuming these nanoparticles are moving like a disk and attenuate as $1/r^2$ as they move away from the target where r is the distance from the target, then at ~ 0.5 mm, d ~$1.3x10^3$ particle/cm^2. The Nd:YAG laser spot size at 0.5 mm away from the target is $2x10^{-4}$ μm^2. Eventually, the number of nanoparticles exists at distance 0.5 mm and within the Nd:YAG laser can be estimated to be N~$11x10^7$ particles. It worth mentioning here that the results in Figure 8.3 are obtained at 20º off-normal; accordingly, in practice, N is even more than what is estimated here.

In conclusion, using a femtosecond laser along with nanosecond laser was found to have a negative impact on the CE due to the loss of the EUV generated photons, which is taken as a negative point for this system. However, the operating conditions can be optimized via tuning the time delay between the two lasers to accomplish a good level of ion debris mitigation while maintaining the CE at an acceptable level. The loss in the CE can be defeated if using a laser with a longer wavelength, such as a commercially available CO_2 laser instead of the Nd:YAG laser that is being used in this work.

CHAPTER 9. SUMMARY AND FUTURE WORK

9.1 Summary

Laser-material interaction is a hot research area in the modern life due to its wide spectrum of applications. Understanding the physics of laser energy coupling to the target material and the consequences of this coupling is essential but complicated. Material properties (thermal and physical properties, for example), laser parameters (pulse duration, wavelength, laser energy, spot size), and ambient conditions (ambient gas, ambient pressure, type of ambient gas) are the main source of this complexity. Furthermore, these parameters/properties are interconnected. The existing simulations and theoretical models are useful tools to understand the physics of laser-material interaction in terms of laser ablation, plume formation, and plasma properties. The complexity of this process limits the simulation tools. For example, simulation of material erosion under thermal, EM and charged particle irradiation like conditions existing in fusion reactor it takes a significantly long time to produce such results; however, not all the physics can be captured.

The work discussed in this thesis provides a methodical series of consecutive experiments designed to help to understand the physics of laser-material interaction and provide a better understanding of how laser energy couples to target material and the consequences of this coupling. The studied topics of this research and the uniqueness of each topic are presented below.

9.1.1 Laser Ablation

The study starts with laser ablation to give insight into what is happening within the volume of the irradiated target. Different laser systems, ultrashort and nanosecond laser, were exploited to investigate some of the laser physics involved in laser material interaction, such as plasma shielding effect and plasma confinement heat-affected zone (HAZ). The effects of several parameters were investigated, such as laser fluence, laser pulse duration, material properties, and ambient conditions. The results show that the laser fluence has a high effect on the material ablation within a certain region in terms of the amount of mass that can be removed from the target, whereas beyond this region, the effect tends to be less significant. The material properties such as melting temperature and heat of vaporization were found to have a significant effect on the

resistivity of the material to incoming irradiation. This resistivity is quantified in this work in terms of the total ablated mass and the amount of melting occuring in the HAZ. The ambient pressure was found to have a significant effect on the laser ablation, whereas no significant difference was observed when using argon and air as ambient gas, especially in terms of the mass. The total mass ablation was found to be almost independent of the type of ambient gas (air and argon). The results of this work introduce a region of laser fluence for the ultrafast laser to be used in the micromachining industry rather than nanosecond laser that is being conventionally used. This topic investigated the laser-material interaction in the terawatt regime at which Beer's law breaks; such a regime was not covered in the literature to the best of our knowledge.

9.1.2 Laser-Ablated Plume

Moving away from the target volume, the study went on to examine the characteristics of the ablated plume that propagates ahead of the target surface. The ablated plume includes charged particles (ions and electrons), neutral atoms, and fragments. The atomic mass weight was found to have a pronounced effect not only on the energy of the ejected ions but also on the ejected ion flux. Insight into the ion dynamics represented by ion flux, ion velocity, temporal and angular distribution of ejected ions, electron plasma density, and electron temperature spatial and temporal evolution found that two types of ions can be ejected from the material according to their energy. The first type is the thermal/slow ions that occur due to the thermal vaporization taking place in the material due to laser irradiation. The other type of ions that was of interest to understand is the nonthermal/fast ions. The results show that these fast ions have a different spatial and temporal distribution from thermal/slow ions. So, the ejection mechanism must also be different. The dynamics of the femto- and nanosecond laser-induced ions were extensively studied, showing that the ejection mechanism responsible for these nonthermal/fast ions is the ambipolar time-dependent electric field, in the case of femtosecond laser, and the further heating of the ablated plume caused by the falling tail of the laser pulse, in the case of nanosecond laser. Results of this work show that ultrafast laser has the potential to fragment the target material into nanoparticles with no chunk of molten material or even microdroplets, with no need for ambient gas, as in the case of nanosecond laser. Accordingly, the ultrafast laser was found to be a promising candidate for thin film fabrication and nanoparticle formation. Studying the electron plasma temperature and electron plasma density completed the picture of laser-material interaction. The main difference between

the nano- and femtosecond laser-induced plasma was found to be in the lifetime of the plasma. The results show that the lifetime of the femtosecond laser-induced plasma is significantly shorter than nanosecond laser-induced plasma by orders of magnitude.

Experimentally finding the existence of different ion ejection mechanisms resulting from laser-material interaction and the role of the ambipolar electric field in ejecting fast ions are some of the unique points of this research, which resolves the different theory in literature around the ion ejection mechanism, mainly fast ions. Furthermore, it explains the dependence of nanoparticle size and shape on the laser properties.

9.1.3 Ion-Debris Mitigation for EUV Generation

Extreme ultraviolet (EUV) photons are currently considered the light source for the next generation of semiconductors and nanofabrication. Currently,there are three main challenges to overcome for industrial mass production. These challenges are conversion efficiency (CE), frequency, and ion debris. The last chapter of this work is dedicated to the last challenge, which is the debris mitigation. In this chapter, a EUV source generation scheme is proposed to tackle the ion debris by irradiating the target at first with femtosecond laser at a low laser intensity. Then irradiating the target with nanosecond laser to optimum laser intensity for EUV photons generation. Ablating the target with femtosecond laser at first results in the generation of an ablated plume. This plume contains charged particles, neutral atoms, and nanoparticles with an absence of the microdroplet mist that is observed when using a laser with longer pulse duration. One can think of it as a cloud of particles at which each species has a different population and different propagating speed. This cloud eventually will act as an attenuating medium to the EUV photons and ions generated using nanosecond laser. Collision with this cloud mitigates the ion debris and scatters and/or absorbs the EUV photons. The loss in the EUV photons that was observed is taken to be a disadvantage when using such a scheme. However, at the optimum time delay between the two lasers, one can achieve a good level of ion debris with an acceptable loss in the EUV photons. Furthermore, the loss in the EUV photons can be overcome by using another laser with a longer wavelength than the Nd:YAG laser used in this work. Such lasers are commercially available, such as a CO_2 laser. The longer the wavelength, the more energy can be absorbed in the plasma.

9.2 Recommendations for Future Research

This section has been added in order to give recommendations for future researchers in the field of laser-material interaction based on the work that has been done throughout this thesis. I would like to highlight some gaps and topics that were not covered in this work. Although this work provides a picture of the physics of the laser-material interaction process, there are still some gaps that need to be addressed to make this picture more complete. The charge state of the emitted ions and the relative population of each species is a vital topic for EUVL generation as well as the fundamental understanding of laser-material interaction, which was not covered in this thesis. Although this research studied the effect of laser fluence on laser ablation for micromachining, the thermal loading effect caused by laser irradiation rate (laser frequency) was not covered in this thesis; this effect should be considered when considering laser micromachining for high-volume manufacturing and cost reduction. In this work, an ablation profile was created that has width dimension in the order of tens of micrometers. The ablation profile as discussed mainly depends on the laser spot size and the Laser Pulse-Wing Effect; laser spot size obtained in this work was obtained using a conventional focusing lens that limits the laser spot size by the diffraction limit, so features with sizes smaller than ten of micrometers were not permissible. In this thesis, an acceptable level of debris mitigation was accomplished when using a combination of femto- and nanosecond laser, but the payoff for that is the CE.

Accordingly, the following topics for future research are proposed:

i. Investigating the effect of laser properties on the population of ions based on their ionic state. Such a study can be conducted using Electrostatic Energy Analyzer. Consequently, conditions for EUVL generation can be optimized.
ii. Studying the thermal loading effect on target material resulting from laser ablation at high frequency for high volume manufacturing. To the best of our knowledge, no comprehensive work has been done to address this issue that, if addressed, will significantly benefit the laser micromachining–dependent industry.
iii. On the application side, focusing the ultrafast laser beyond the diffraction limit corresponding to its wavelength may cause a significant improvement to the micromachining industry, such as solar cell fabrication and nanolithography applications, as it will provide the capability to manufacture features in the sub micrometer regions.

iv. The loss in CE accompanied by minimizing the ion debris mitigation can be overcome when using a nanosecond laser with a longer wavelength than the one that was used in this work (CO_2 laser instead of Nd:YAG laser, for example), which is commercially available, along with the femtosecond laser. The longer the wavelength, the higher the absorptivity of the laser photon in the ablated plume that, in turn, will increase the emission of EUV photons so CE.

v. When moving from the femtosecond laser ablation region to the picosecond laser ablation region, the size of the fragment changes. The effect of the size of these fragments on the EUV photon generation process is interesting to explore as well.

vi. It is also interesting to eliminate the effect of Nd:YAG laser-bulk material interaction and study the effect of Nd:YAG laser nanoparticle interaction separately. This can be accomplished by using an orthogonal irradiation scheme at which the irradiation angle between the femtosecond laser and nanosecond laser will be 90^{o} degrees. In this case, the nanoparticles will be the main medium to generate EUV photons and, at the same time, the medium to mitigate the ion debris.

APPENDIX

In this appendix, a supplementary experimental data is provided that could be helpful for future work and simulation benchmarking.

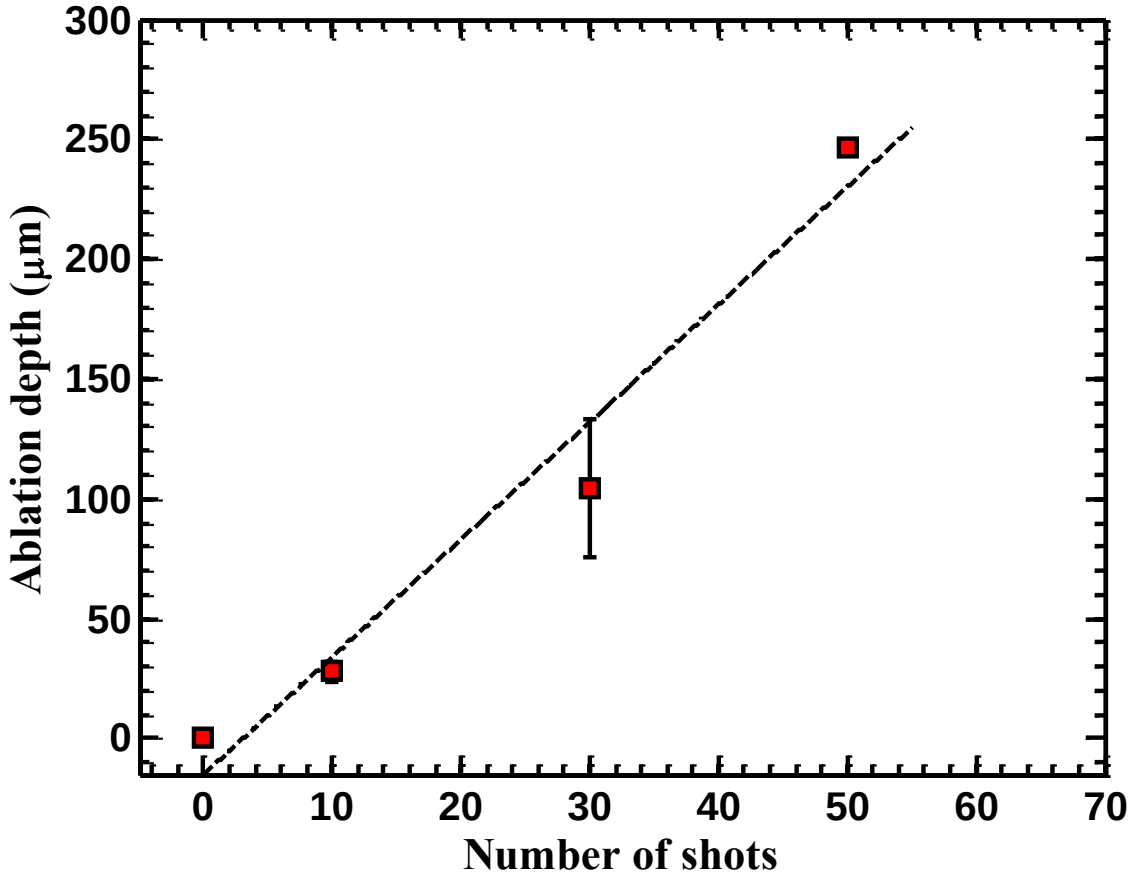

Figure A.1 Ablation depth as a function of the number of laser shots. The data was acquired using Ti:Sapphire laser that delivers the intensity of 6.37×10^{14} W/cm^2.

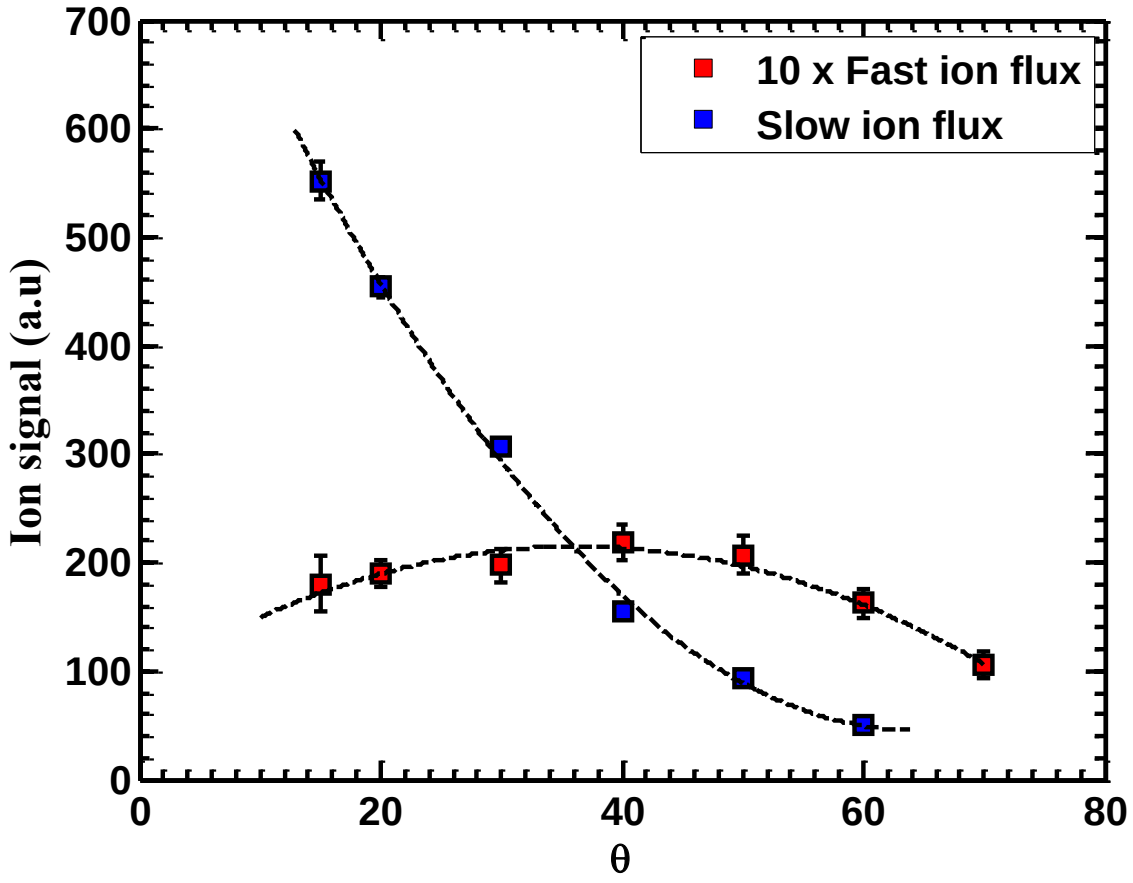

Figure A 2 Ion flux angular distribution at a normal laser incidence angle. The data acquired using 2.5×10^{10} W/cm^2 Nd;YAG laser.

REFERENCES

[1] J. Hecht, *Short History of Laser Development*, SPIE Reviews.

[2] W. Zinth, A. Laubereau, and W. Kaiser, *The Long Journey to the Laser and Its Rapid Development after 1960*, European Physical Journal H.

[3] P. Stavropoulos, C. Palagas, G. N. Angelopoulos, D. N. Papamantellos, and S. Couris, *Calibration Measurements in Laser-Induced Breakdown Spectroscopy Using Nanosecond and Picosecond Lasers*, Spectrochim. Acta - Part B At. Spectrosc. **59**, 1885 (2004).

[4] W. Gong, Z. Zheng, J. Zheng, X. Hu, and W. Gao, *Water Soluble CdS Nanoparticles with Controllable Size Prepared via Femtosecond Laser Ablation*, J. Appl. Phys. **102**, 064304 (2007).

[5] J. R. Freeman, S. S. Harilal, and A. Hassanein, *Enhancements of Extreme Ultraviolet Emission Using Prepulsed Sn Laser-Produced Plasmas for Advanced Lithography Applications*, J. Appl. Phys. **110**, 083303 (2011).

[6] L. Wang, W. Li, W. Zhang, L. Li, R. Zhao, Q. Liu, L. Li, H. Wang, and H. Yang, *Manipulating Redox Reaction during Pulsed Laser Deposition*, J. Appl. Phys. **118**, 185305 (2015).

[7] T. Kanesue, Y. Fuwa, K. Kondo, M. Okamura, T. Kanesue, Y. Fuwa, K. Kondo, and M. Okamura, *Laser Ion Source with Solenoid Field Laser Ion Source with Solenoid Field*, Appl. Phys. Lett. **105**, 193506 (2014).

[8] Y. A. Il'inskii and L. V. Keldysh, *Electromagnetic Response of Material Media* (1994).

[9] R. Kelly and A. Miotello, *Does Normal Boiling Exist Due to Laser-Pulse or Ion Bombardment?*, J. Appl. Phys. **87**, 3177 (2000).

[10] E. G. Gamaly, A. V Rode, V. T. Tikhonchuk, and B. Luther-Davies, *Ablation of Solids by Femtosecond Lasers : Ablation Mechanism and Ablation Thresholds for Metals and Dielectrics*, Phys. Rev. A **9**, 1 (2001).

[11] R. Timm, P. R. Willmott, and J. R. Huber, *Ablation and Blow-off Characteristics at 248 Nm of Al, Sn and Ti Targets Used for Thin Film Pulsed Laser Deposition*, J. Appl. Phys. **80**, 1794 (1996).

[12] S. S. Harilal, G. V. Miloshevsky, T. Sizyuk, and A. Hassanein, *Effects of Excitation Laser Wavelength on Ly-α and He-α Line Emission from Nitrogen Plasmas*, Phys. Plasmas (2013).

[13] A. E. Hussein, P. K. Diwakar, S. S. Harilal, and A. Hassanein, *The Role of Laser Wavelength on Plasma Generation and Expansion of Ablation Plumes in Air*, J. Appl. Phys. (2013).

[14] F. Rezaei and S. H. Tavassoli, *Developing the Model of Laser Ablation by Considering the Interplay between Emission and Expansion of Aluminum Plasma*, Phys. Plasmas **20**, 013301 (2013).

[15] S. Mehrabian, M. Aghaei, and S. H. Tavassoli, *Effect of Background Gas Pressure and Laser Pulse Intensity on Laser Induced Plasma Radiation of Copper Samples*, Phys. Plasmas (2010).

[16] J. P. Colombier, P. Combis, F. Bonneau, R. Le Harzic, and E. Audouard, *Hydrodynamic Simulations of Metal Ablation by Femtosecond Laser Irradiation*, Phys. Rev. B **71**, 165406 (2005).

[17] A. Semerok, C. Chaléard, V. Detalle, J.-L. Lacour, P. Mauchien, P. Meynadier, C. Nouvellon, B. Sallé, P. Palianov, M. Perdrix, and G. Petite, *Experimental Investigations of Laser Ablation Efficiency of Pure Metals with Femto, Pico and Nanosecond Pulses*, Appl. Surf. Sci. **138**–**139**, 311 (1999).

[18] S. P. Banerjee and R. Fedosejevs, *Single Shot Depth Sensitivity Using Femtosecond Laser Induced Breakdown Spectroscopy*, Spectrochim. Acta Part B At. Spectrosc. **92**, 34 (2014).

[19] T. Donnelly, J. G. Lunney, S. Amoruso, R. Bruzzese, X. Wang, and X. Ni, *Dynamics of the Plumes Produced by Ultrafast Laser Ablation of Metals*, J. Appl. Phys. **108**, 043309 (2010).

[20] J. P. Colombier, P. Combis, F. Bonneau, R. Le Harzic, and E. Audouard, *Hydrodynamic Simulations of Metal Ablation by Femtosecond Laser Irradiation*, Phys. Rev. B **71**, 165406 (2005).

[21] A. Macchi, M. Borghesi, and M. Passoni, *Ion Acceleration by Superintense Laser-Plasma Interaction*, Rev. Mod. Phys. (2013).

[22] D. S. Finn, Z. Lin, J. Kleinert, M. J. Darwin, and H. Zhang, *Study of Die Break Strength and Heat-Affected Zone for Laser Processing of Thin Silicon Wafers*, J. Laser Appl. (2015).

[23] J. Bovatsek, A. Tamhankar, R. S. Patel, N. M. Bulgakova, and J. Bonse, *Thin Film Removal Mechanisms in Ns-Laser Processing of Photovoltaic Materials*, Thin Solid Films **518**, 2897 (2010).

[24] M. Capitelli, A. Casavola, G. Colonna, and A. De Giacomo, *Laser-Induced Plasma Expansion: Theoretical and Experimental Aspects*, Spectrochim. Acta Part B At. Spectrosc. **59**, 271 (2004).

[25] H. R. Griem, *High-Density Corrections in Plasma Spectroscopy*, Phys. Rev. **128**, 997 (1962).

[26] F. Anabitarte, A. Cobo, and J. M. Lopez-Higuera, *Laser-Induced Breakdown Spectroscopy: Fundamentals, Applications, and Challenges*, ISRN Spectrosc. **2012**, 1 (2012).

[27] S. Amoruso, X. Wang, C. Altucci, C. De Lisio, M. Armenante, R. Bruzzese, and R. Velotta, *Thermal and Nonthermal Ion Emission during High-Fluence Femtosecond Laser Ablation of Metallic Targets Thermal and Nonthermal Ion Emission during High-Fluence Femtosecond Laser Ablation of Metallic Targets*, Appl. Phys. Lett. **77**, 3728 (2000).

[28] Z. Zhang, P. A. VanRompay, J. A. Nees, C. A. Stewart, X. Pan, G. A. Gary, and P. P. Pronko, *Diagnostics for Femtosecond and Nanosecond Laser-Ablation Discharge Plasmas as Used in Thin Film Growth*, in *Proceedings of SPIE - The International Society for Optical Engineering*, edited by R. F. Haglund, Jr. and R. F. Wood, Vol. 3935 (2000), pp. 86–96.

[29] T. Donnelly, J. G. Lunney, S. Amoruso, R. Bruzzese, X. Wang, and X. Ni, *Dynamics of the Plumes Produced by Ultrafast Laser Ablation of Metals*, J. Appl. Phys. **108**, 043309 (2010).

[30] G. O. Williams, G. M. O'Connor, P. T. Mannion, and T. J. Glynn, *Langmuir Probe Investigation of Surface Contamination Effects on Metals during Femtosecond Laser Ablation*, Appl. Surf. Sci. **254**, 5921 (2008).

[31] R. R. Schaller, *Moore's Law: Past, Present, and Future*, IEEE Spectr. (1997).

[32] A. Roy, S. S. Harilal, M. P. Polek, S. M. Hassan, A. Endo, and A. Hassanein, *Influence of Laser Pulse Duration on Extreme Ultraviolet and Ion Emission Features from Tin Plasmas*, Phys. Plasmas **21**, 033109 (2014).

[33] S. S. Harilal, *Influence of Spot Size on Propagation Dynamics of Laser-Produced Tin Plasma*, J. Appl. Phys. **102**, 123306 (2007).

[34] E. Parra, I. Alexeev, J. Fan, K. Y. Kim, S. J. McNaught, and H. M. Milchberg, *X-Ray and Extreme Ultraviolet Emission Induced by Variable Laser Pulse-Width Irradiation of Ar and Kr Clusters and Droplets*, in *Conference on Lasers and Electro-Optics Europe - Technical Digest* (2001).

[35] M. Schnürer, S. Ter-Avetisyan, H. Stiel, U. Vogt, W. Radloff, M. Kalashnikov, W. Sandner, and P. V. Nickles, *Influence of Laser Pulse Width on Absolute EUV-Yield from Xe-Clusters*, Eur. Phys. J. D (2001).

[36] T. Ando, S. Fujioka, H. Nishimura, N. Ueda, Y. Yasuda, K. Nagai, T. Norimatsu, M. Murakami, K. Nishihara, N. Miyanaga, Y. Izawa, K. Mima, and A. Sunahara, *Optimum Laser Pulse Duration for Efficient Extreme Ultraviolet Light Generation from Laser-Produced Tin Plasmas*, Appl. Phys. Lett. (2006).

[37] T. Donnelly, J. G. Lunney, S. Amoruso, R. Bruzzese, X. Wang, X. Ni, T. Donnelly, J. G. Lunney, S. Amoruso, R. Bruzzese, X. Wang, and X. Ni, *Dynamics of the Plumes Produced by Ultrafast Laser Ablation of Metals Dynamics of the Plumes Produced by Ultrafast Laser Ablation of Metals*, J. Appl. Phys. **108**, 043309 (2010).

[38] S. Amoruso, X. Wang, C. Altucci, C. de Lisio, M. Armenante, R. Bruzzese, N. Spinelli, and R. Velotta, *Double-Peak Distribution of Electron and Ion Emission Profile during Femtosecond Laser Ablation of Metals*, Appl. Surf. Sci. **186**, 358 (2002).

[39] E. G. Gamaly, A. V Rode, B. Luther-Davies, and V. T. Tikhonchuk, *Ablation of Solids by Femtosecond Lasers: Ablation Mechanism and Ablation Thresholds for Metals and Dielectrics*, Phys. Plasmas **9**, 949 (2002).

[40] S. Amoruso, R. Bruzzese, N. Spinelli, R. Velotta, M. Vitiello, X. Wang, G. Ausanio, V. Iannotti, and L. Lanotte, *Generation of Silicon Nanoparticles via Femtosecond Laser Ablation in Vacuum*, Appl. Phys. Lett. **84**, 4502 (2004).

[41] T. E. Glover, *Hydrodynamics of Particle Formation Following Femtosecond Laser Ablation*, J. Opt. Soc. Am. B **20**, 125 (2003).

[42] D. Perez and L. J. Lewis, *Ablation of Solids under Femtosecond Laser Pulses*, Phys. Rev. Lett. **89**, 255504 (2002).

[43] P. Gibbon, *Short Pulse Laser Interactions with Matter*, first edit (Imperial College Press, 2005).

[44] E. G. Gamaly, *Femtosecond Laser-Matter Interations: Theory, Experiments and Applications*, first (Pan Standford Publishing Pte. Ltd., 2011).

[45] B. Luther-Davies, E. G. Gamalii, Y. Wang, and A. V Rode, *Matter in Ultrastrong Laser Fields*, Sov. J. Quantum Electron **22**, 289 (1992).

[46] M. I. Kaganov, I. M. Lifshitz, and L. V Tanatarov, *Relaxation between Electrons and the Crystalline Lattice*, Jetp, Sov. Phys. **4**, 173 (1957).

[47] S. I. Anisimov, K. B. L, and T. L. Perel'man, *Electron Emission from Metal Surfaces Exposed to Ultrashort Laser Pulses*, Sov. Phys. JETP **39**, 375 (1975).

[48] T. J. Kelly, T. Butler, N. Walsh, P. Hayden, and J. T. Costello, *Features in the Ion Emission of Cu, Al, and C Plasmas Produced by Ultrafast Laser Ablation*, Phys. Plasmas **22**, 123112 (2015).

[49] B. N. Chichkov, C. Momma, S. Nolte, F. Alvensleben, and A. Tünnermann, *Femtosecond, Picosecond and Nanosecond Laser Ablation of Solids*, Appl. Phys. A Mater. Sci. Process. **63**, 109 (1996).

[50] K. K. Anoop, X. Ni, M. Bianco, D. Paparo, X. Wang, R. Bruzzese, and S. Amoruso, *Two-Dimensional Imaging of Atomic and Nanoparticle Components in Copper Plasma Plume Produced by Ultrafast Laser Ablation*, Appl. Phys. A **117**, 313 (2014).

[51] K. K. Anoop, X. Ni, X. Wang, R. Bruzzese, and S. Amoruso, *Spectrally Resolved Imaging of Ultrashort Laser Produced Plasma*, IEEE Trans. Plasma Sci. **42**, 2698 (2014).

[52] K. K. Anoop, X. Ni, X. Wang, and S. Amoruso, *Fast Ion Generation in Femtosecond Laser Ablation of a Metallic Target at Moderate Laser Intensity*, Laser Phys. **24**, 105902 (2014).

[53] A. M. Elsied, P. C. Dieffenbach, P. K. Diwakar, and A. Hassanein, *Nanosecond Laser-Metal Ablation at Different Ambient Conditions*, Spectrochim. Acta - Part B At. Spectrosc. **143**, 26 (2018).

[54] A. M. Elsied, P. K. Diwakar, and A. Hassanein, *Comprehensive Studies of Ultrashort Laser Pulse Ablation of Tin Target at Terawatt Power*, Spectrochim. Acta - Part B At. Spectrosc. **139**, (2018).

[55] Q. Bian, X. Yu, B. Zhao, Z. Chang, and S. Lei, *Femtosecond Laser Ablation of Indium Tin-Oxide Narrow Grooves for Thin Film Solar Cells*, Opt. Laser Technol. **45**, 395 (2013).

[56] C. W. Cheng, S. Y. Wang, K. P. Chang, and J. K. Chen, *Femtosecond Laser Ablation of Copper at High Laser Fluence: Modeling and Experimental Comparison*, Appl. Surf. Sci. **361**, 41 (2016).

[57] A. M. Elsied, P. K. Diwakar, M. Polek, and A. Hassanein, *Dynamics of Low- and High-Z Metal Ions Emitted during Nanosecond Laser-Produced Plasmas*, J. Appl. Phys. **120**, 173104 (2016).

[58] S. M, N, *Ionization in the Solar Chromosphere*, Phil. Mag **238**, 472 (1920).

[59] K. Eidmann, J. Meyer-ter-Vehn, and T. Schlegel, *Hydrodynamic Simulation of Subpicosecond Laser Interaction with Solid-Density Matter*, Phys. Rev. E **62**, 1202 (2000).

[60] P. Nica, S. Gurlui, M. Agop, and C. Focsa, *Oscillatory Regimes of Langmuir Probe Current in Femtosecond Laser-Produced Plasmas: Experimental and Theoretical Investigations*, Appl. Surf. Sci. **481**, 125 (2019).

[61] G. Baraldi, A. Perea, and C. N. Afonso, *Dynamics of Ions Produced by Laser Ablation of Several Metals at 193 Nm*, J. Appl. Phys. **109**, 043302 (2011).

[62] N. Farid, S. S. Harilal, H. Ding, and A. Hassanein, *Kinetics of Ion and Prompt Electron Emission from Laser-Produced Plasma*, Phys. Plasmas **20**, 073114 (2013).

[63] R. C. Issac, P. Gopinath, G. K. Varier, V. P. N. Nampoori, and C. P. G. Vallabhan, *Twin Peak Distribution of Electron Emission Profile and Impact Ionization of Ambient Molecules during Laser Ablation of Silver Target*, Appl. Phys. Lett. **73**, 163 (1998).

[64] D. Wu, L. Sun, J. Liu, X. Yu, R. Hai, C. Feng, Z. Wang, and H. Ding, *Dynamics of Prompt Electrons, Ions, and Neutrals of Nanosecond Laser Ablation of Tungsten Investigated Using Optical Emission*, Phys. Plasmas **26**, 013303 (2019).

[65] D. A. Cremers and L. J. Radziemski, *LIBS Apparatus Fundamentals*, Handb. Laser-Induced Break. Spectrosc. 69 (2013).

[66] E. Tognoni, V. Palleschi, M. Corsi, and G. Cristoforetti, *Quantitative Micro-Analysis by Laser-Induced Breakdown Spectroscopy: A Review of the Experimental Approaches*, Spectrochim. Acta Part B At. Spectrosc. **57**, 1115 (2002).

[67] M. Hanif, M. Salik, and M. A. Baig, *Optical Spectroscopic Studies of Titanium Plasma Produced by an Nd : YAG Laser*, Opt. Spectrosc. **114**, 7 (2013).

[68] G. Abdellatif and H. Imam, *A Study of the Laser Plasma Parameters at Different Laser Wavelengths* □, Spectrochim. Acta - Part B At. Spectrosc. **57**, 1155 (2002).

[69] A. M. El Sherbini and A. A. S. Al Aamer, *Measurement of Plasma Parameters in Laser-Induced Breakdown Spectroscopy Using Si-Lines*, World J. Nano Sci. Eng. (2012).

[70] A. M. Elsied, N. C. Termini, P. K. Diwakar, and A. Hassanein, *Characteristics of Ions Emission from Ultrashort Laser Produced Plasma*, Sci. Rep. **6**, 38256 (2016).

[71] G. Miloshevsky and A. Hassanein, *Modeling of Macroscopic Melt Layer Splashing during Plasma Instabilities*, J. Nucl. Mater. **415**, S74 (2017).

[72] L. T. Ciavola, S. Gammino, L. Ando, A. B. Laska, and J. Krasa, *Metallic Etching by High Power Nd : Yttrium – Aluminum – Garnet Pulsed Laser Irradiation*, Rev. Sci. Instrum. **71**, 4330 (2000).

[73] S. B. Wen, X. Mao, R. Greif, and R. E. Russo, *Laser Ablation Induced Vapor Plume Expansion into a Background Gas. II. Experimental Analysis*, J. Appl. Phys. **101**, (2007).

[74] N. Arnold, J. Gruber, and J. Heitz, *Spherical Expansion of the Vapor Plume into Ambient Gas: An Analytical Model*, Appl. Phys. A Mater. Sci. Process. **69**, 87 (1999).

[75] A. Bogaerts, Z. Chen, R. Gijbels, and A. Vertes, *Laser Ablation for Analytical Sampling: What Can We Learn from Modeling?*, Spectrochim. Acta - Part B At. Spectrosc. **58**, 1867 (2003).

[76] T. Sizyuk and A. Hassanein, *Scaling Mechanisms of Vapour/Plasma Shielding from Laser-Produced Plasmas to Magnetic Fusion Regimes*, Nucl. Fusion **54**, 023004 (2014).

[77] Y. Tao, H. Nishimura, S. Fujioka, A. Sunahara, M. Nakai, T. Okuno, N. Ueda, K. Nishihara, N. Miyanaga, and Y. Izawa, *Characterization of Density Profile of Laser-Produced Sn Plasma for 13.5nm Extreme Ultraviolet Source*, Appl. Phys. Lett. **86**, 201501 (2005).

[78] A. Hassanein, T. Sizyuk, V. Sizyuk, and S. S. Harilal, *Combined Effects of Pre-Pulsing and Target Geometry on Efficient EUV Production from Laser Produced Plasma Experiments and Modeling*, in *Proceedings of SPIE - The International Society for Optical Engineering*, edited by B. M. La Fontaine and P. P. Naulleau, Vol. 7969 (2011), p. 79690D.

[79] V. Sizyuk, A. Hassanein, and T. Sizyuk, *Three-Dimensional Simulation of Laser-Produced Plasma for Extreme Ultraviolet Lithography Applications*, J. Appl. Phys. **100**, 103106 (2006).

[80] A. Hassanein, *Effects of Plasma Spatial Profile on Conversion Efficiency of Laser-Produced Plasma Sources for EUV Lithography*, J. Micro/Nanolithography, MEMS, MOEMS **8**, 041503 (2009).

[81] N. Ueda, M. Nagata, H. Nishimura, S. Fujioka, T. Aota, Y. Yasuda, Y. Inubushi, T. Ando, T. Norimatsu, M. Nakai, K. Nagai, K. Nishihara, A. Sunahara, N. Miyanaga, Y. Izawa, and K. Mima, *Extreme Ultraviolet Emission from Laser-Irradiated Low-Density Xe Targets*, Jpn. J. Appl. Phys. **45**, 5951 (2006).

[82] H. Mizoguchi, A. Endo, T. Ariga, T. Miura, H. Hoshino, Y. Ueno, M. Nakano, H. Komori, A. Sumitani, T. Abe, T. Suganuma, G. Soumagne, H. Someya, Y. Takabayashi, and K. Toyoda, *Development of CO 2 Laser Produced Xe Plasma EUV Light Source for Microlithography*, in edited by M. J. Lercel, Vol. 6151 (2006), p. 61510S.

PUBLICATIONS

Dieffenbach, P. C., Borkowski, C. M., **Elsied, A. M.,** *Diwakar, P. K., Sizyuk, T., & Hassanein, A. (2019), Effects of Laser Wavelength on Aluminum Plasma in Transverse Magnetic Fields. Physics of Plasmas (Accepted)*

Elsied, A. M., *Dieffenbach, P. C., Diwakar, P. K., & Hassanein, A. (2018), Comprehensive Studies of Ultrashort Laser Pulse Ablation of Tin Target at Terawatt Power. Spectrochimica Acta B.* ***139****, 57-62.*

A. Suslova, **Elsied, A. M.,** *& Hassanein, A. (2018), Computer Simulation and Experimental Benchmarking of Ultrashort Pulse Laser Ablation of Metallic Targets. Laser Part. Beams. 1-10.*

Elsied, A. M., *Dieffenbach, P. C., Diwakar, P. K., & Hassanein, A. (2017), Nanosecond Laser-Metal Ablation at Different Ambient Conditions. Spectrochimica Acta B.* ***143****, 26-31.*

Elsied, A. M., *Dieffenbach, P. C., Diwakar, P. K., Sizyuk, T., & Hassanein, A. (2017) Laser Induced Ablation of Metals at Different Ambient Conditions: Experiments and Simulation. APS Meeting Abstracts.*

Elsied, A. M., *Termini, N., Diwakar, P. K., & Hassanein, A. (2016),* Characteristics of Ions Emission from Ultrashort Laser Produced Plasma. *Sci. Rep.* **6**, 38256.

Elsied, A. M., Diwakar, P. K., Polek, M., & Hassanein, A. (2016). Dynamics of low- and high-Z metal ions emitted during nanosecond laser-produced plasmas. *Journal of Applied Physics*, ***120***(17), 173104.

Elsied, A. M., Hafz, N. A. M., Li, S., Mirzaie, M., Sokollik, T., & Zhang, J. (2015). Generation of high-qualtiy electron beams from a laser-based advanced accelerator at Shanghai Jiao Tong University. *Chinese Physics C*, ***39***(6), 067003–067009.

Elsied, A. M., Giboni, K. L., & Ji, X. (2015). Alternative connection scheme for PMTs in large, low energy LXe detectors. *Journal of Instrumentation, **10**(01) T01003.*

Tao, M., Hafz, N. A. M., Li, S., Mirzaie, M., **Elsied, A. M. M**., Ge, X., Zhang, J. (2014). Quasimonoenergetic collimated electron beams from a laser wakefield acceleration in low density pure nitrogen. *Physics of Plasmas*, ***21***(7), 73102.

Li, S., Hafz**,** N. A. M., Mirzaie, M., **Elsied, A. M. M.,** Ge, X., Liu, F., Zhang, J. (2014). Generation of electron beams from a laser wakefield acceleration in pure neon gas. *Physics of Plasmas*, ***21***(8), 83108.